Quantitative seismic interpretation in thin-bedded geology using full-wavefield elastic modelling

Saskia Tschache

Thesis for the degree of Philosophiae Doctor (PhD)
University of Bergen, Norway
2023

UNIVERSITY OF BERGEN

Quantitative seismic interpretation in thin-bedded geology using full-wavefield elastic modelling

Saskia Tschache

Thesis for the degree of Philosophiae Doctor (PhD)
at the University of Bergen

Date of defense: 28.09.2023

Year: 2023

Title: Quantitative seismic interpretation in thin-bedded geology using full-wavefield elastic modelling

Name: Saskia Tschache

Print: Skipnes Kommunikasjon / University of Bergen

Preface

This thesis is an article-based dissertation submitted for the partial fulfilment of the requirements for the degree of Philosophiae Doctor (PhD) at the University of Bergen. The research work was conducted by the author within an industrial PhD project under the agreement of CGG Services (Norway) AS, the University of Bergen and the Research Council of Norway. The project was funded by the Research Council of Norway under grant 310441. The PhD candidate was employed by CGG Services (Norway) AS from January 2020 to March 2023 and conducted the research work in the CGG office in Oslo. The main supervisor was Prof. Einar Iversen at the University of Bergen and the co-supervisors were Dr. Vetle Vinje, Senior Scientist at CGG Services (Norway) AS, and Dr. Jan Erik Lie, Geophysical Advisor at AkerBP ASA.

Acknowledgements

This endeavour would not have been possible without the guidance and support of my supervisors Dr. Vetle Vinje, Prof. Einar Iversen and Dr. Jan Erik Lie. It has been a great honour to work with and learn from such excellent researchers. Thank you for always being available and helpful when I needed some advice and for your encouragement during the difficult moments of this journey.

I would like to thank all the (former) colleagues, co-authors and external researchers who have contributed to my PhD project and been involved in discussions about my work, especially Gordon Poole, Dr. Henning Hoeber, Dr. Peng Zhao, Marianne Gram-Jensen, Martin Brandtzæg Gundem, Dr. Per Avseth and Dr. Thomas Elboth.

I would like to thank CGG for providing a professional work environment in which I was able to concentrate fully on the PhD project and was given all the support and resources I needed. I am particularly grateful to all the colleagues at CGG who helped me to revise the research articles included in this thesis. Many thanks to the colleagues in the Oslo office for the socialising during lunch and coffee breaks.

Special thanks to my peers Dr. Volodya Hlebnikov, Dr. Thomas de Jonge and Dr. Jing Sun for the mutual support and for the many happy moments on this PhD journey. I would also like to thank the PhD students at AkerBP for the fortnightly technical exchange and the PhD students at the University of Bergen with whom I collaborated during the courses.

The Research Council of Norway, CGG and the University of Bergen are acknowledged for funding this industrial PhD project under grant no. 310441.

Last but not least, I would like to thank my family, partner and friends for all their support during this sometimes challenging time.

Abstract in English

Reflection seismics is used to image the subsurface for the exploration of oil and gas, geothermal or carbon storage reservoirs, among others. In addition to the structural interpretation of the resulting seismic images, the seismic data can be interpreted quantitatively with the goal to obtain rock and fluid properties. An essential tool in quantitative seismic interpretation is the analysis of the amplitude variation with offset (AVO).

Thin-bedded geology below the seismic resolution poses challenges for AVO modelling and interpretation. One problem addressed in this thesis is accurate seismic forward modelling in thin-bedded media. Primaries-only convolutional modelling, commonly used in conventional AVO modelling and inversion, is prone to failure in the presence of thin beds. Better alternatives are finite-difference modelling or the reflectivity method. The reflectivity method is a semi-analytic modelling method for horizontally layered media and is computationally cheaper than finite-difference modelling on densely sampled grids. I show in this thesis that the reflectivity method is well-suited for the AVO modelling of layered media.

The band-limited nature of seismic data is one reason for the non-unique estimation of reservoir properties from seismic data, especially in thin-bedded geology. Probabilistic inversion methods, such as Bayesian methods, honour this non-uniqueness by predicting probabilities that allow the uncertainty to be quantified.

In this thesis, I integrate full-wavefield elastic seismic modelling by the reflectivity method with Bayesian classification and inversion. The objective is to address two concrete quantitative seismic interpretation problems: 1) the uncertainty quantification of Bayesian pore-fluid classification in the presence of thin high-impedance layers caused by calcite cementation in sandstone, and 2) the estimation of reservoir properties of turbidite reservoirs characterised by sand-shale interbedding.

In the first application, I show through a modelling study that calcite-cemented beds lead to detectable reflection responses that can interfere with the target reflection at the reservoir top and thereby perturb the AVO behaviour. The observed effect increases

the uncertainty of pore-fluid classification based on AVO attributes, as demonstrated by a case study. Consequently, the probability of a false hydrocarbon indication is significantly increased in the presence of calcite-cemented beds.

In the second application, I present a Bayesian inversion that takes the AVO intercept and gradient measured at the top of a reservoir as input and estimates the probability density function of the net-to-gross ratio and the net-pay-to-net ratio. The method was applied to synthetic data and AVO attribute maps from the Jotun field on the Norwegian Continental Shelf. It was found that the AVO gradient correlates with the net-to-gross ratio of the reservoir, while the AVO intercept is most sensitive to the type of pore fluid. After inversion, maps of the most-likely values of the net-to-gross ratio, net-pay-to-net ratio, net pay and the uncertainty could be generated. These maps help to identify potential zones of high reservoir quality and hydrocarbon saturation.

Abstract in Norwegian

Refleksjonsseismikk brukes til å lage seismiske «bilder» av den øverste delen av jordskorpen, blant annet med tanke på leting etter reservoarer for olje, gass, karbonlagring og geotermisk energi. I tillegg til å gi grunnlag for en strukturell tolkning, kan de seismiske dataene brukes til å kvantifisere egenskapene til det faste materialet og væskeinnholdet i bergartene. Et viktig verktøy i slik kvantitativ seismisk tolkning er analyse av såkalt AVO: amplitudenes variasjon med avstanden mellom kilde og mottaker (offset).

Tynne geologiske lag gir utfordringer for AVO-modellering og tolkning, fordi lagtykkelsen vil kunne være mindre enn oppløsningen i de seismiske dataene. En problemstilling som tas opp i denne avhandlingen er nettopp hvordan man kan gjøre nøyaktig seismisk (forover) modellering i medier med tynne lag. En konvensjonell tilnærming innen AVO-modellering og inversjon er å bruke såkalt konvolusjonsmodellering. Denne metoden tar imidlertid bare hensyn til de primære seismiske refleksjonene og er derfor unøyaktig når modellene har tynne lag. To bedre alternativer er endelig-differanse-modellering og reflektivitetsmetoden. Reflektivitetsmetoden er en delvis analytisk modelleringsmetode for horisontalt lagdelte medier og er beregningsmessig billigere enn endelig-differanse-modellering, der beregningene er basert på et tett samplet rutenett (grid). Jeg viser i avhandlingen at reflektivitetsmetoden er godt egnet for AVO-modellering i lagdelte medier.

Seismiske data har en båndbegrenset karakter. En konsekvens er at beregning av reservoaregenskaper fra seismiske data generelt ikke er entydig, noe som særlig kommer til uttrykk for lagdelt geologi med tynne lag. Probabilistiske inversjonsmetoder, som for eksempel bayesianske metoder, tar hensyn til denne flertydigheten ved å forutsi sannsynligheter, noe som gjør det mulig a kvantisere usikkerheten.

I avhandlingen kombinerer jeg seismisk modellering med bayesiansk klassifisering og inversjon. Modelleringen er utført med reflektivitetsmetoden og er basert på det komplette elastiske bølgefeltet. Formålet er å adressere to konkrete kvantitative seismiske tolkningsproblemer: 1) kvantifisering av usikkerhet i bayesiansk porevæske-klassifisering i nærvær av tynne lag med høy impedans, forårsaket av kalsittsementering i sandstein,

og 2) estimering av reservoaregenskapene til turbiditt-reservoarer karakterisert ved alternerende lag av sandstein og skifer.

I den første anvendelsen viser jeg i en modelleringsstudie at kalsitt-sementerte lag kan gi en detekterbar refleksjonsrespons, noe som kan påvirke amplituden målt ved reservoartoppen og dermed forstyrre AVO-målingen. Den observerte effekten øker usikkerheten ved porevæske-klassifisering basert på AVO-attributter, som jeg har demonstrert i en case-studie. Følgelig øker sannsynligheten for en falsk hydrokarbon-indikasjon betydelig i nærvær av kalsittsementerte lag.

I den andre anvendelsen presenterer jeg en bayesiansk inversjon som tar AVO-skjæringspunktet og gradienten målt på toppen av et reservoar som inngangsdata og estimerer sannsynlighetstetthetsfunksjonen til forholdstallene «net-to-gross» og «net-pay-to-net». Metoden ble anvendt på syntetiske data og AVO-attributtkart fra Jotunfeltet på norsk kontinentalsokkel. Det ble funnet at AVO-gradienten korrelerer med reservoarets net-to-gross forhold, mens AVO-skjæringspunktet er mest følsomt for typen porevæske. Etter inversjon genererte jeg kart over de mest sannsynlige verdiene av forholdene net-to-gross og net-pay-to-net, samt kart over net pay og usikkerhetene. Disse kartene kan bidra til å identifisere potensielle soner med høy reservoarkvalitet og hydrokarbonmetning.

List of publications

1. S. Tschache, V. Vinje, E. Iversen, *On the accuracy and spatial sampling of finite-difference modelling in discontinuous models*, Journal of Applied Geophysics **206**, 104789, 2022, DOI: `https://doi.org/10.1016/j.jappgeo.2022.104789`.

2. S. Tschache, V. Vinje, J. E. Lie, E. Iversen, *Quantifying amplitude-variation-with-offset uncertainties related to calcite-cemented beds using a Monte Carlo simulation*, Interpretation **11**, Issue 2, T315–T329, 2023, DOI: `https://doi.org/10.1190/int-2022-0084.1`.

3. S. Tschache, V. Vinje, J. E. Lie, M. Brandtzæg Gundem, E. Iversen, *Estimation of net-to-gross ratio and net pay from seismic amplitude variation with offset using Bayesian inversion*, submitted to Interpretation 5 April 2023.

Contents

Chapter 1

Introduction

1.1 Outline

This thesis is based on three research articles. The first part of the thesis describes the fundamental theory, concepts and methods used in the articles, gives context to the research work, summarises the results and presents an overall discussion and conclusion of the thesis. The second part of the thesis is the chapter "Scientific results" that contains the articles in their published or submitted formats.

The first chapter comprises the background, motivation, scope and scientific contributions of the thesis.

The subsequent four chapters introduce the scientific methods. Chapter 2 covers important aspects of finite-difference modelling relevant for Article 1. The central method of this thesis is the reflectivity method. With chapter 3, a comprehensive chapter is dedicated to this method. A review of the theory is given, modelling examples are shown and applications of the method are discussed. The fourth chapter introduces amplitude-variation-with-offset theory and the practical aspects of its analysis. In chapter 5, selected statistical methods are covered.

The sixth chapter provides summaries of the individual research articles.

A conclusion, discussion and outlook are given in chapter 7.

Finally, the full-length research articles are presented in the last chapter.

1.2 Background

Active reflection seismics is a geophysical method that makes it possible to image the subsurface of the earth. The method can be applied both on land and at sea and is widely used for the exploration of oil and gas, minerals, geothermal reservoirs or in the context of carbon capture and storage. Figure 1.1 shows a sketch of a marine seismic towed-streamer acquisition. A single airgun (as shown in the figure) or an airgun array towed by a vessel generates acoustic waves that travel through the water layer and penetrate the earth layers below the water bottom. Streamers equipped with seismic sensors (hydrophones) record the reflected signals.

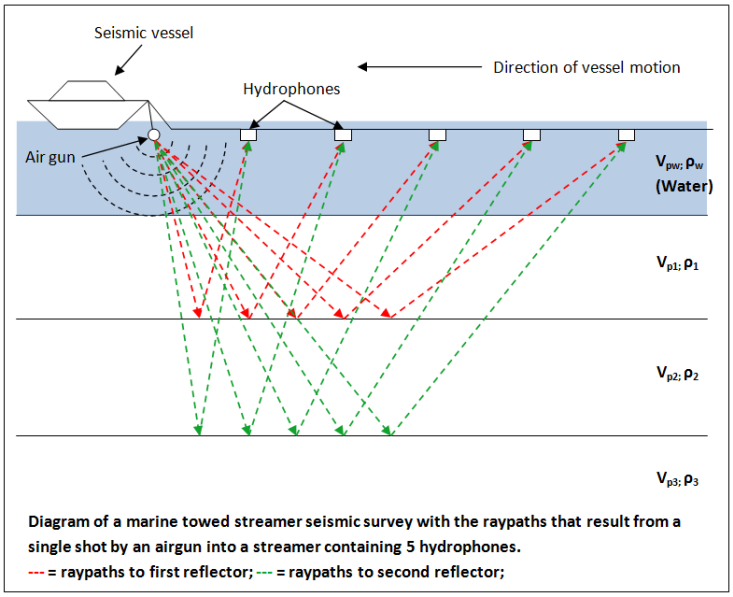

Figure 1.1: Sketch of a marine seismic towed-streamer acquisition. Created by Nwhit and licensed under CC BY-SA 3.0.

The reflection seismic method consists of three major steps:

1. Data acquisition
2. Data processing and imaging
3. Interpretation.

Today, the industry standard is 3D seismic surveys producing 3D image volumes of the subsurface after a sophisticated data processing and imaging procedure. Seismic waves

are reflected at interfaces at which the elastic properties change (see Figure 1.1). The resulting seismic images are band-limited reflectivity images that can be regarded to represent interfaces of rock units. Furthermore, the images contain noise and unwanted signals that could not be completely removed during the processing and possibly artefacts arising from imaging procedures. In the third step, seismic images are structurally interpreted and correlated with well data to produce models of the subsurface. Quantitative interpretation attempts to link seismic signatures to geological and reservoir-related properties (Avseth et al., 2005).

The analysis of the amplitude variation with offset (AVO) is one of the most important tools of quantitative interpretation (Avseth et al., 2005), especially for the exploration of hydrocarbons (Castagna and Backus, 1993; Chopra and Castagna, 2014). However, there are several challenges and pitfalls in AVO interpretation related to seismic data processing, AVO modelling and AVO inversion (Avseth et al., 2005). In addition, geological heterogeneity and complexity can make the interpretation of seismic AVO signatures difficult. The thesis addresses specifically the challenges caused by thin-bedded geology. The impact of thin layers with high acoustic impedance contrast (Article II) and low impedance contrast (Article III) on seismic AVO are investigated in this thesis.

Seismic forward modelling simulates a seismic experiment given an earth model and the locations of a source and receivers. Seismic modelling is a powerful tool and plays an important role in all three major steps of the seismic method. It can be used to design an optimal acquisition layout (step 1), it is an integral component of modern imaging techniques (step 2) and it can help to interpret seismic data, e.g., by seismic AVO modelling (step 3). There are several methods for seismic forward modelling, which all come with their individual advantages and limitations (Carcione et al., 2002; Krebes, 2004). Among the most widely used ones are the finite-difference method (Fichtner, 2010), ray tracing (Červený, 2001), the reflectivity method (Kennett, 2009) and convolutional modelling (Russell, 1988).

Seismic finite-difference modelling is used as part of seismic imaging and velocity model building steps, such as reverse-time migration and full-waveform inversion. As a direct method (Carcione et al., 2002), it solves the wave equation numerically in a discretised subsurface model and at finite time steps using finite-difference approximations of derivatives. Thereby, the full wavefield can be simulated. The downside of the finite-difference method is its high computational cost, especially in 3D or when a dense grid sampling is required to model high frequencies.

The reflectivity method is a non-asymptotic semi-analytic modelling method for horizontally layered media (Sen, 2021). Despite the limitation to stratified media, there are

many possible applications of this modelling method in the seismic industry. This thesis demonstrates how full-wavefield elastic modelling by the reflectivity method can be applied to address specific challenges in quantitative interpretation caused by thin-bedded geology.

1.3 Motivation and scope of the thesis

Quantitative seismic interpretation by means of AVO analysis has been successfully applied to locate hydrocarbon reservoirs (Castagna and Backus, 1993; Chopra and Castagna, 2014; Simm and Bacon, 2014). However, AVO anomalies have been falsely interpreted as hydrocarbon accumulations in many situations (Allen et al., 1993) and AVO inversion can fail in practice (Avseth et al., 2016). There are many challenges and pitfalls in seismic AVO analysis and interpretation. Measured seismic amplitudes can be affected by noise, acquisition effects, distortions during processing and residual moveout (Downton et al., 2000; Avseth et al., 2005). It should be kept in mind that residual noise and multiples can be present after seismic data processing and that migration methods have limitations and can generate artefacts. Furthermore, seismic ray paths might be distorted by structurally complex geology (Downton et al., 2000). Seismic data have a limited bandwidth. Small-scale heterogeneity below the seismic resolution affects the seismic amplitudes through interference and tuning effects.

This thesis focuses on the effect of vertical heterogeneity of reservoir and caprock on seismic AVO and AVO-based quantitative interpretation. In Article II, the impact of thin high-impedance layers on AVO is analysed and the uncertainty of AVO-based pore-fluid classification in the presence of such hard beds is quantified. The focus of Article III is a shale–sand interbedding typical for turbidite reservoirs. A Bayesian inversion is presented that estimates probability distributions of reservoir properties from seismic AVO attributes.

Most commercially used AVO techniques are based on the Zoeppritz equations or their linearised approximations (Downton et al., 2000). The Zoeppritz equations are valid under the assumption that a plane wave hits the planar interface of two isotropic and homogeneous media (Aki and Richards, 2002; Avseth et al., 2005). Consequently, these assumptions are violated when the plane-wave approximation of a seismic wave does not hold (as discussed in more detail in subsection 3.2.1), the interface is curved or the media are anisotropic or heterogeneous. Conventional AVO modelling, well ties and seismic pre-stack inversion are based on convolutional seismic modelling (Russell, 1988) using the Zoeppritz equations or linearised approximations. This means that AVO pitfalls

may arise when the mentioned assumptions for the Zoeppritz equations are not met, for example, in thin-bedded geology (Avseth et al., 2005). The limitations of convolutional modelling are discussed and demonstrated in Articles II and III.

In this thesis, the reflectivity method is used as an alternative to primaries-only convolutional modelling for layered media. The reflectivity method has two major advantages over convolutional modelling. Firstly, the elastic full-wavefield response of a layered medium including internal multiples, transmission loss and mode conversions is modelled in contrast to primary reflections only. Secondly, the spherical-wave response is modelled rather than the plane-wave response. As a semi-analytic method, the reflectivity method is accurate for any layer thickness, which is also proven in Article I.

The semi-analytic character of the reflectivity method guaranteeing high accuracy makes it an ideal benchmark tool for other seismic forward modelling methods. The two most important criteria of seismic modelling are accuracy and computational cost. For efficiency, it is desirable to find the limit of achieving a sufficiently high accuracy for a respective use case at a minimum computational cost. Efficiency becomes particularly important when modelling tasks are performed many times, such as in iterative inversion schemes or Monte Carlo simulations. This is also true for finite-difference modelling, which is widely used in the seismic industry. As a numerical method computed on grids in space and at discrete time steps, the accuracy generally increases with decreasing sampling intervals in space and time. At the same time, the computational cost increases. One goal of the PhD project was therefore to analyse the accuracy of finite-difference modelling in horizontally layered thin-bedded media to find the optimal gridding parameters and method for efficient seismic modelling as presented in Article I.

Seismic reservoir characterisation is part of quantitative seismic interpretation and aims at estimating reservoir properties from seismic data or seismic attributes (Grana et al., 2021). There are many factors that lead to uncertainty in seismic reservoir characterisation, such as noise, the limited resolution of seismic data, seismic data processing, approximations in physical relations, structurally complex geology, anisotropy and geomechanical processes (Grana et al., 2021). In this thesis, the focus is on the uncertainty associated with thin beds below the seismic resolution.

Several deterministic and probabilistic methods can be applied to solve an inverse geophysical problem. Deterministic methods predict a single solution as the best estimate. In contrast to deterministic methods, probabilistic methods predict a probability or probability distribution of the model variable. Probabilistic algorithms honour the non-uniqueness of the solution to an inverse problem by estimating the most likely solution as well as the uncertainty associated with a prediction (Grana et al., 2021). Uncertainty

estimates are useful to assess risks in decision-making, to integrate different types of data and they help to estimate the value of additional information (Avseth et al., 2005).

Grana et al. (2022) reviewed the latest scientific progress in the probabilistic inversion of seismic data for reservoir characterisation. Most of the applications to date are based on the Bayesian approach (Grana et al., 2022), which has also been used in Articles II and III. Article II considers uncertainty in Bayesian classification, while Article III presents a Bayesian inversion.

1.4 Scientific contributions

The fundamental building block of the PhD project is a seismic modelling code that implements the reflectivity method. At the beginning of the project, several available open-source codes of the reflectivity method were tested. However, the available codes were too restrictive in array sizes, model parametrisation and source definition. In addition, some modelling results exhibited serious wraparound artefacts. In order to have full control of all aspects of the modelling, it was decided to develop a modelling code from scratch as part of the PhD project. This also allowed implementing efficient seismic forward modelling as part of Monte Carlo simulations, where a large number of simulations is required.

Some features of the modelling code to highlight are:

- acoustic, elastic or viscoelastic simulation
- support of 2D (line source) and 3D (point source) wave propagation
- generation of spherical-wave or optionally plane-wave synthetics
- computation of pressure and displacement
- source definition by excitation function or (far-field) wavelet in displacement or pressure
- option between free surface or absorbing upper model boundary
- option to include or ignore the direct wave

A complete review of the theory of the reflectivity method is given in chapter 3. The seismic modelling code was carefully checked against benchmarks from analytical solutions and finite-difference modelling. The modelling code was used in the research work

for all three articles that are included in this thesis. Future research and development activities of CGG will benefit from the code.

In addition to the developed seismic modelling code, the main scientific contributions of the thesis can be summarised as follows:

1. Article I gives recommendations for model gridding to achieve accurate seismic finite-difference modelling results efficiently in discontinuous media. These recommendations refer to the spatial sampling interval and the procedure for low-pass filtering the model. It is demonstrated that the devised filtering procedure is suited for the downsampling/upscaling of well logs to produce model grids for efficient finite-difference modelling. In addition, it is shown that the reflectivity method and the finite-difference method give practically identical results provided a sufficiently dense spatial sampling. Checked against analytical solutions, both modelling methods can be used to accurately model AVO effects in thin-bedded media.

2. In Article II, the increase in uncertainty of AVO-based pore-fluid classification caused by calcite-cemented beds is quantified. A workflow is presented that can be adapted to any reservoir that is prone to calcite cementation to obtain better uncertainty estimates for risk assessment.

3. Article III presents a Bayesian inversion of AVO attributes for the net-to-gross ratio and the net pay in turbidite reservoirs. It is demonstrated how the inversion results can be displayed on maps to guide interpretation and decision-making.

To summarise, the feasibility of efficient and accurate full-wavefield elastic modelling by the reflectivity method for Monte Carlo simulations is demonstrated. This allows to study the AVO uncertainty related to thin-bedded geology.

Chapter 2

Finite-difference modelling

This chapter introduces seismic finite-difference modelling briefly and covers aspects that are relevant for Article I.

2.1 Fundamentals

The propagation of seismic waves is described by the wave equation. The finite-difference (FD) method can be used to solve the wave equation numerically. The method is based on a discretisation in space and time or frequency. The fundamental idea behind FD modelling is to replace derivatives with finite-difference approximations. These approximations are derived from truncated Taylor series. A second-order central finite-difference approximation of the spatial derivative of a function $f(x_i)$ at location x_i can be written as (Fichtner, 2010, eq. 2.41)

$$\frac{\partial f(x_i)}{\partial x} = \frac{1}{2\Delta x}\left[f(x_i + \Delta x) - f(x_i - \Delta x)\right] + \mathcal{O}((\Delta x)^2) \ , \tag{2.1}$$

where Δx denotes the spatial sampling interval. In this 1D example, the derivative is approximated by the difference of function $f(x)$ evaluated at the two neighbouring points.

Higher-order finite-difference stencils can be constructed from truncated Taylor series in the same way as the second-order stencil. They will converge faster to the exact solution as Δx approaches zero and give generally a higher accuracy at a finite Δx (Fichtner, 2010).

Alternatively, spatial derivatives can be numerically computed by the Fourier or pseu-

dospectral method (Kosloff and Baysal, 1982; Fornberg, 1988). The spatial derivatives are computed in the Fourier domain and are accurate up to the Nyquist frequency of the grid (Kosloff and Baysal, 1982). Theoretically, two grid points per wavelength are sufficient for the spatial sampling of the wavefield (Kosloff and Baysal, 1982). The pseudospectral method can be regarded as the limit of increasing order of finite-difference stencils (Fornberg, 1987).

2.2 Formulations

There are finite-difference schemes for solving the acoustic (Alford et al., 1974), elastic (Graves, 1996) or viscoelastic (Robertsson et al., 1994) wave equation. For solving the elastic wave equation, several formulations exist, such as the velocity-stress formulation, the displacement-stress formulation or the displacement formulation (Fichtner, 2010). Most prominent is the Virieux-type staggered scheme using the velocity-stress formulation (Virieux, 1986; Levander, 1988), where some components of variables are computed in between grid points on a second, staggered grid. The usage of staggered grids decreases the effective grid spacing for the same number of discrete variables and therefore reduces the numerical dispersion (Fichtner, 2010).

The fact that vectors of field variables need to be computed for elastic wave propagation with the grid spacing and time step restricted by the lowest shear wave velocity in the model makes elastic FD modelling computationally expensive (Alkhalifah, 2000). Therefore, many applications in the seismic industry to date use acoustic FD modelling as a computationally cheaper approximation. The wavefield in acoustic media can be described by a single scalar field, the pressure. Acoustic FD schemes for vertical and tilted transversely isotropic media have been implemented (Alkhalifah, 2000; Zhang et al., 2011). The FD scheme used in Article I described by Zhang et al. (2011) is based on conventional central grids in contrast to staggered grids.

2.3 Numerical accuracy and stability

The maximum time step for numerical stability of an FD scheme is given by the Courant-Friedrichs-Lewy (CFL) condition (Courant et al., 1967) that takes the general form (Fichtner, 2010, eq. 3.49)

$$\Delta t \leq \text{const.} \frac{\Delta x}{v_{max}} \ , \tag{2.2}$$

where Δx denotes a constant grid spacing and v_{max} is the maximum wave velocity. The constant depends on the specific FD scheme.

A too sparsely sampled wavefield will suffer from the numerical artefact of grid dispersion. To avoid grid dispersion, the grid spacing Δx should be chosen according to the criterion (Bohlen et al., 2015)

$$\Delta x \leq \frac{\lambda_{min}}{n} = \frac{v_{min}}{n f_{max}} \ , \tag{2.3}$$

where λ_{min} denotes the minimum wavelength, v_{min} is the minimum wave velocity in the model and f_{max} is the maximum frequency of the wavelet. The required number n of grid points per shortest wavelength depends on the FD operator length and type (Bohlen et al., 2015). Higher-order FD schemes require a lower number n. The Nyquist criterion requires $n = 2$ grid points per shortest wavelength. As mentioned, this is the theoretical requirement for pseudospectral schemes (Kosloff and Baysal, 1982).

Apart from the grid sampling requirement to avoid grid dispersion, the presence of discontinuities in the FD grid will lead to other types of numerical errors (Symes and Vdovina, 2009; Mittet, 2017, 2021). In practice, this will make a denser grid sampling necessary. Article I elaborates on the required grid spacing in discontinuous models concluding that 4-5 points per shortest wavelength are sufficient for a pseudospectral scheme.

Chapter 3

Reflectivity method

This chapter introduces the reflectivity method as a modelling tool in seismology and applied seismics, explains the theory and gives an overview of its application in today's research and technology. Complete derivations can be found in the book by Kennett (2009).

3.1 Definition and development

Reflectivity methods encompass techniques for calculating synthetic seismograms in stratified media that include in general the full wavefield with all elastic wave phenomena. In the literature, the term *reflectivity method* often refers to the more specific technique described by Fuchs and Müller (1971), which calculates only the reflection response of a set of layers comprising a reflection zone that is located below the source and receivers. As discussed by Kennett (2009), this specific technique can be regarded as the synthesis of a subset of the full response. In this thesis, I use the term *reflectivity method* in the broader sense of a technique that is able to model the full response of a stratified medium to energy excited by a source, including a reflective surface above the source.

The origin of reflectivity methods lies in propagator-matrix methods for elastic wave propagation in stratified media developed by Thomson (1950), Haskell (1953) and Knopoff (1964). Fuchs (1968) and Fuchs and Müller (1971) established the reflectivity method as a practical tool for the computation of synthetic seismograms. Kennett (1974) derived an iterative scheme for the computation of reflection and transmission coefficients of multi-layered media by connecting the layer matrices to their reflection and transmission properties. Fryer (1980) proposed a slowness approach to the reflectivity

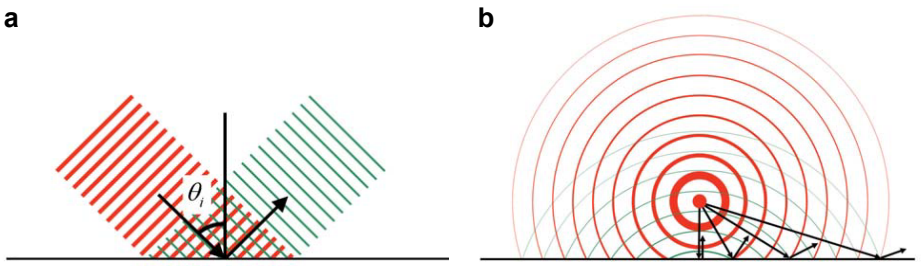

Figure 3.1: Schematic illustration of the reflection of a plane wave (a) and a spherical wave (b) at a horizontal interface. The thickness of the wavefront lines of the incident wave (red) and the reflected wave (green) indicates the wave's amplitude. While the amplitude of a plane wave changes only upon reflection, the amplitude of a spherical wave changes additionally during propagation. Modified after Ursenbach et al. (2007).

method. An extension of the reflectivity method to anisotropic layers was introduced by Booth and Crampin (1983). While the theory of reflectivity methods was well understood, several authors tried to accelerate the numerical computations (Phinney et al., 1987) and discussed practical computational aspects (Mallick and Frazer, 1987).

3.2 Theory

The reflectivity method can be broken down into two main steps: (i) the computation of the overall plane-wave reflectivity matrix of a layered medium for all slowness values p and radial frequency values ω of interest and (ii) the synthesis of the spherical-wave response measured at a receiver location by numerically computing the Sommerfeld integral (Sommerfeld, 1909, 1949).

3.2.1 The concepts of plane waves and spherical waves

For understanding the theory of the reflectivity method, it is important to know the difference between the concepts of plane and spherical waves. The concept of plane waves is often used in physics and more specifically, commonly used in seismic amplitude variation with offset (AVO) applications (Ostrander, 1984; Aki and Richards, 2002; Chopra and Castagna, 2014). However, point sources generate spherical waves (true spherical wavefronts only in isotropic media). Figure 3.1 illustrates the reflection of a plane wave (Figure 3.2.1a) and a spherical wave (Figure 3.2.1b) at a horizontal interface.

Unlike plane waves, spherical waves undergo spherical divergence, which means that the

wave's amplitude decreases as the wave travels. When a plane wave hits an interface, the energy partition into reflected and transmitted energy is independent of the wave's frequency, which is also evident from the Knott-Zoeppritz equations (Knott, 1899; Zoeppritz, 1919). Spherical-wave reflectivity is an integral of many plane-wave contributions (Aki and Richards, 2002) and is frequency-dependent (Ursenbach et al., 2007; Li et al., 2017). The reflection coefficient of a spherical wave can be regarded as a sum of plane-wave reflectivity contributions from a range of incidence angles around the central ray (Alhussain et al., 2008) and the frequencies that constitute its wavelet (Ursenbach et al., 2007). The difference between a plane-wave and a spherical-wave reflection coefficient becomes large when (i) the wavefront curvature is strong (Krail and Brysk, 1983) or (ii) the incidence angle approaches the critical angle because the plane-wave reflection coefficient changes rapidly there and reflected and head waves interfere (Alhussain et al., 2008). The latter has implications for all AVO applications that are based on plane-wave theory: Since the plane-wave assumption does not hold for reflections near the critical angle, critical and post-critical events should not be included in conventional plane-wave AVO analysis or inversion.

3.2.2 Assumptions

The basic assumption for applying the reflectivity method is that the medium can be described as a stack of homogeneous horizontal layers. Such a model is sometimes called a *1D model* because its properties only vary in one dimension, the depth. The layers are assumed to be acoustic, elastic or viscoelastic. Acoustic layers are realised by a shear wave velocity approaching zero. Viscoelasticity is described by a constant quality factor Q and a reference frequency f_r and is realised by working with complex velocities (Müller, 1985, eq. 132). Furthermore, it is assumed that the layer properties are isotropic. Extensions of the reflectivity method for anisotropic media exist (Booth and Crampin, 1983) but were not used in this thesis.

The modelling code written during this PhD project aims at simulating marine towed-streamer reflection seismic acquisitions. Therefore, an additional assumption is made for the uppermost layer to be a fluid layer bounded by the free surface at the top and the seabed at the bottom. It is further assumed that the source and receivers are located in this fluid layer and that the source generates only compressional waves and the receivers measure only compressional waves. Figure 3.2 illustrates the case of a source and receiver located in a fluid layer on top of a stack of elastic layers.

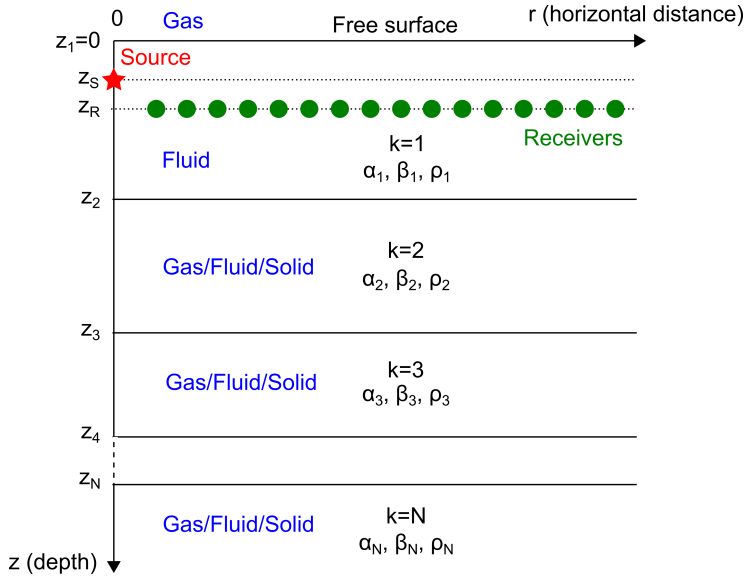

Figure 3.2: Sketch of a layered model according to the assumptions made for the reflectivity method as it is used in this thesis. Each layer k is defined by its upper boundary located at depth z_k and the constant elastic properties P-wave velocity α_k, S-wave velocity β_k and density ρ_k. The uppermost surface is the free surface located at $z = 0$. The first layer is assumed to be a fluid layer that contains the source and receivers.

3.2.3 Overall P-P reflectivity of a layered medium

Let us first concentrate on the reflected waves from a stack of layers below the source and receiver. Given the (visco-)elastic properties of the layers, it is possible to compute the overall reflectivity R_D of a stack of layers that includes all internal multiples and mode conversions. This computation can be achieved by an iterative scheme proposed by Kennett (1974). The overall reflectivity $R_D(z_k-)$ of a downgoing wavefield impinging on interface k, just above layer k, specified as depth z_k-, can be expressed as (Kennett, 2009, eq. 6.26)

$$R_D(z_k-) = R_{D,k} + T_{U,k} R_D(z_k+) \left[I - R_{U,k} R_D(z_k+)\right]^{-1} T_{D,k} \ , \tag{3.1}$$

where I is the identity matrix and $R_{D,k}$, $R_{U,k}$, $T_{D,k}$, and $T_{U,k}$ denote the local plane-wave reflection and transmission coefficient matrices at interface k with subscript D for downgoing and subscript U for up-going incident waves. These four matrices are computed by the Knott-Zoeppritz equations, e.g., given in matrix form by Aki and Richards (2002, eq. 5.36-5.38). Matrix $R_D(z_k+)$ denotes the overall reflectivity just below interface k. It is computed by the multiplication of the overall reflectivity $R_D(z_{k+1}-)$ just above the interface $k+1$ with phase terms that correspond to the propagation through the uniform

layer k,

$$R_D(z_k+) = E_{D,k} R_D(z_{k+1}-) E_{D,k} \ , \tag{3.2}$$

where $E_{D,k}$ denotes the phase matrix of layer k.

All reflection and transmission matrices in equations (3.1) and (3.2) are 2×2-matrices of the structure

$$\begin{pmatrix} PP & SP \\ PS & SS \end{pmatrix} \ ,$$

where the first letter denotes the incident wave type of P- or S-wave and the second letter denotes the reflected or transmitted wave type, respectively.

The phase matrices are diagonal 2×2-matrices because the waves travel as either P- or S-wave through the uniform layer,

$$E_{D,k} = \begin{pmatrix} e^{-i\omega q_{\alpha,k}(z_{k+1}-z_k)} & 0 \\ 0 & e^{-i\omega q_{\beta,k}(z_{k+1}-z_k)} \end{pmatrix} \ , \tag{3.3}$$

where ω denotes radial frequency and $q_{\alpha,k} = \sqrt{\alpha_k^{-2} - p^2}$ and $q_{\beta,k} = \sqrt{\beta_k^{-2} - p^2}$ are the layer-specific P-wave and S-wave vertical slownesses, respectively, resulting from a given horizontal slowness p. When waves become evanescent, i.e., the vertical slowness q becomes imaginary, the branch cuts need to be chosen such that (Kennett, 2009, eq. 28)

$$\exp(-i\omega q(z_{k+1} - z_k)) = \exp(-i\omega \, |q| \, (z_{k+1} - z_k)) \ . \tag{3.4}$$

Since $z_{k+1} > z_k$, growing exponentials with increasing frequencies are avoided and the computationally scheme is numerically stable (Kennett, 2009).

Starting at the deepest interface of the model, where $R_D(z_N-) = R_{D,N}$, equations (3.1) and (3.2) can now be applied alternately in an iterative way moving the layer stack upwards until the seabed is reached. Finally, the PP-component of $R_D(z_2-)$ is multiplied with a phase term to include the travel time from source level z_S to z_2 and back to source level z_S.

$$R_D(z_S) = R_{D,PP}(z_2-) e^{-2i\omega q_{\alpha,1}(z_2 - z_S)}. \tag{3.5}$$

R_D represents then the overall P-wave to P-wave reflectivity of the whole stack of uniform layers below the seabed for a specific radial frequency ω and horizontal slowness p, $R_D(z_S, \omega, p)$. It should be noted that mode conversions, such as PPSP, PSPP, PSSP, etc. are included. This iterative computation scheme needs to be performed for several horizontal slownesses and frequencies in order to compute spherical-wave seismograms.

The matrix inverse in equation (3.1) can be approximated by a series expansion and,

thus, be replaced by a truncated series of reverberations (Kennett, 2009)

$$[I - R_{U,k}R_D(z_k+)]^{-1} \approx I + R_{U,k}R_D(z_k+) + R_{U,k}R_D(z_k+)R_{U,k}R_D(z_k+) + \dots \ . \quad (3.6)$$

It should be noted that the interface reflection and transmission matrices $R_{D,k}$, $R_{U,k}$, $T_{D,k}$, and $T_{U,k}$ are frequency-independent in the acoustic or elastic case and can be pre-computed.

3.2.4 Reflections at the free surface

Reflections at the free surface at the top of the model ($z = z_1 = 0$) are responsible for the source and receiver ghost and reverberations observed as free-surface multiples. The free surface can be treated via reflection matrices or explicitly (Kennett, 2009). Here, we compute the local P-P reflection coefficient $R^{fS}_{U,PP}$ of an upgoing incident wavefield by the Knott-Zoeppritz equations using a typical compressional wave velocity and density for air to incorporate the boundary conditions at $z = 0$. The local free-surface reflection coefficient is multiplied by a phase term to include the travel time from source level z_S to the free surface at $z = 0$ and back to source level z_S. The free-surface reflectivity is then given by

$$R^{fS}_U(z_S) = R^{fS}_{U,PP} e^{(-2i\omega q_{\alpha,1} z_S)} \ , \quad (3.7)$$

where $q_{\alpha,1} = \sqrt{\alpha_1^{-2} - p^2}$ is the vertical slowness of a P-wave for a horizontal slowness p.

From the overall reflectivity R_D of a layer stack below the source and receiver and the free-surface reflectivity R^{fS}_U, the displacement wavefield $W(z_R)$ at receiver level z_R for $z_R < z_S$ is given by (Kennett, 2009, eq. 7.35),

$$W(z_R) = \left[W_{US}(z_R) + W_{DS}(z_R)R^{fS}_U\right]\left[1 - R_D R^{fS}_U\right]^{-1}\left[\Sigma_U + R_D\Sigma_D\right] \ , \quad (3.8)$$

and for $z_R > z_S$ is given by (Kennett, 2009, eq. 7.36),

$$W(z_R) = \left[W_{DS}(z_R) + W_{US}(z_R)R_D\right]\left[1 - R^{fS}_U R_D\right]^{-1}\left[\Sigma_D + R^{fS}_U\Sigma_U\right] \ . \quad (3.9)$$

W_{US} and W_{DS} account for the correct travel time to receiver level z_R for upgoing and downgoing waves arriving at the receiver, respectively.

$$\begin{aligned} W_{US} &= \exp(-i\omega q_{\alpha,1}(z_S - z_R)) \ , \\ W_{DS} &= \exp(+i\omega q_{\alpha,1}(z_S - z_R)) \ . \end{aligned} \quad (3.10)$$

Additionally, receiver directivity could be included. If the displacement needs to be

computed at receiver level z_R, the horizontal and vertical components of displacement are given by

$$\begin{aligned} W_{US}^{hor} &= \sin\theta W_{US} \ , \\ W_{DS}^{hor} &= \sin\theta W_{DS} \ , \\ W_{US}^{ver} &= -\cos\theta W_{US} \ , \\ W_{DS}^{ver} &= \cos\theta W_{DS} \ . \end{aligned} \tag{3.11}$$

Σ_U and Σ_D represent the upward and downward radiation of the source. If we assume that the radiation pattern of the source is equal in all directions, then

$$\Sigma_U = \Sigma_D = 1 \ . \tag{3.12}$$

To better understand equations (3.8) and (3.9), they should be read from right to left. The right term in equation (3.8) represents the source contribution. It consists of directly upwards radiated waves from the source Σ_U and downwards radiated waves that are reflected at the interfaces below the source $R_D\Sigma_D$. The term in the centre is a reverberation operator that couples the free-surface reflections with the reflections of the layers below the source. It can be replaced by a limited number of reverberations analogous to equation (3.6). The left term in equation (3.8) corresponds to the receiver level z_R. It contains waves that arrive at the receiver travelling upwards $W_{US}(z_R)$ and downwards after being reflected at the free surface $W_{DS}(z_R)R_U^{fS}$.

If we want to simulate an absorbing boundary at $z = 0$ instead of a free surface, we can set R_U^{fS} to zero. It follows then for $z_R < z_S$,

$$W(z_R) = W_{US}(z_R)\Sigma_U + W_{US}(z_R)R_D\Sigma_D \ . \tag{3.13}$$

The waves arriving at the receiver are coming upwards either directly from the source or after reflection from below. For $z_R > z_S$, we get

$$W(z_R) = W_{DS}\Sigma_D(z_R) + W_{US}(z_R)R_D\Sigma_D \ . \tag{3.14}$$

In this case, the waves arriving at the receiver are coming downwards directly from the source or upwards after reflection from below.

3.2.5 Source excitation function

Given a source signal at a distance R_1 from the source in radial displacement $U(R_1, t)$ or pressure $P(R_1, t)$, it is possible to compute the excitation function $F(t)$ of the source, be it an explosive point source (3D wave propagation) or an explosive line source (2D wave propagation). The Fourier transform of the excitation function, $\hat{F}(\omega)$, will later be used in the computation of synthetic seismograms.

Spherical waves generated by an explosion point source

The compressional potential $\Phi(R, t)$ at distance R and at time t of a spherical wave generated by an explosion point source in an acoustic medium of constant compressional wave velocity α is given by (Müller, 2007, eq. 3.8)

$$\Phi(R, t) = \frac{1}{R} F\left(t - \frac{R}{\alpha}\right) , \tag{3.15}$$

where $F(t)$ denotes the source excitation function, also called the reduced displacement potential (Müller, 2007).

The radial displacement $U(R, t)$ can then be derived as (Müller, 2007, eq. 3.9)

$$U(R, t) = \frac{\partial \Phi}{\partial R} = -\frac{1}{R^2} F\left(t - \frac{R}{\alpha}\right) - \frac{1}{R\alpha} F'\left(t - \frac{R}{\alpha}\right) , \tag{3.16}$$

where the first term represents the *near-field term* dominating at sufficiently short distances R and the second term is the *far-field term* dominating at distances larger than several wavelengths (Müller, 2007). Using the boundary condition that a defined displacement signal $U_1(R_1, t)$ at distance $R = R_1$ fulfils equation (3.16), it is possible to compute the excitation function $F(t)$ of the source. For the computation, we use the displacement $\bar{U}_1\left(t - \frac{R_1}{\alpha}\right) = \bar{U}_1(\tau) = U_1(t)$ at the retarded time $\tau = t - \frac{R_1}{\alpha}$. The relationship between the source excitation function and the defined displacement signal at distance R_1 follows from equation (3.16) and is expressed in the frequency domain as

$$\hat{F}(\omega) = -\frac{R_1^2 \hat{\bar{U}}_1(R_1, \omega)}{1 + \frac{i\omega R_1}{\alpha}} , \tag{3.17}$$

where i denotes the imaginary unit and ω denotes radial frequency.

If a pressure signal $\bar{P}_1(R_1, t - \frac{R_1}{\alpha}) = \bar{P}_1(R_1, \tau) = P_1(R_1, t)$ at distance R_1 and retarded time $\tau = t - \frac{R_1}{\alpha}$ is given, the corresponding source excitation function $F(t)$ can be

computed using the relation (Müller, 2007)

$$P(r,t) = -\rho \frac{\partial \Phi(r,t)}{\partial t^2} \ , \tag{3.18}$$

assuming a constant density ρ in the medium, resulting in

$$\hat{F}(\omega) = \frac{R_1}{\omega^2 \rho} \hat{\hat{P}}_1(R_1, \omega) \tag{3.19}$$

in the frequency domain.

Cylindrical waves generated by an explosion line source

The compressional potential $\Phi(R,t)$ at distance R and time t of a cylindrical wave generated by an explosion line source in an acoustic medium of a constant compressional wave velocity α is given by (Müller, 2007, eq. 3.95)

$$\Phi(R,t) = \int_{\frac{R}{\alpha}}^{t} F(t-\tau) \cosh^{-1}\left(\frac{\alpha\tau}{R}\right) d\tau \ , t > \frac{R}{\alpha} \ , \tag{3.20}$$

where $F(t)$ denotes the source excitation function. Equation (3.20) describes a convolution of $F(t)$ with $F(t) \equiv 0$ if $t < 0$ and the function $K(R,t)$, which is defined as

$$K(R,t) = \begin{cases} 0 & \text{if } t < \frac{R}{\alpha} \\ \cosh^{-1}\left(\frac{\alpha t}{R}\right) & \text{if } t \geq \frac{R}{\alpha} \end{cases} \ . \tag{3.21}$$

In the frequency domain, the convolution is expressed as a multiplication of the two functions, so that

$$\Phi(R,\omega) = \hat{F}(\omega)\hat{K}(R,\omega). \tag{3.22}$$

Using the relationship between pressure P and compressional potential Φ given by equation (3.18), the source excitation function $\hat{F}(\omega)$ can be computed in the frequency domain given a pressure signal $\hat{P}(R_1,\omega)$ at a distance R_1

$$\hat{F}(\omega) = \frac{\hat{P}(R_1,\omega)}{\rho\omega^2 \hat{K}(R_1,\omega)} \ , \tag{3.23}$$

where ρ denotes the density of the medium.

The radial displacement $U(R,t)$ can be derived as (Müller, 2007, eq. 3.96)

$$U(R,t) = \frac{\partial \Phi}{\partial R} = \frac{\partial}{\partial R}\left(F(t) * K(R,t)\right) = F(t) * \frac{\partial K(R,t)}{\partial R} = F(t) * Y(R,t) \ , t > \frac{R}{\alpha} \ , \tag{3.24}$$

where $Y(R,t)$ is defined as

$$Y(R,t) = \frac{\partial K(R,t)}{\partial R} = -\frac{t}{R\left(t^2 - \frac{R^2}{\alpha^2}\right)^{\frac{1}{2}}} \ , t > \frac{R}{\alpha} \tag{3.25}$$

The source excitation function $\hat{F}(\omega)$ can be computed given a radial displacement signal $U(R_1,\omega)$ at distance R_1 in frequency domain as follows

$$\hat{F}(\omega) = \frac{\hat{U}(R_1,\omega)}{\hat{Y}(R_1,\omega)} \ . \tag{3.26}$$

3.2.6 Computation of synthetic seismograms

A spherical wave generated by a point source can be expressed as a sum of plane-wave contributions using the Weyl integral (Weyl, 1919) or as a sum of conical-wave contributions using the Sommerfeld integral (Sommerfeld, 1909, 1949). The Sommerfeld integral itself can be derived from the Weyl integral (Müller, 2007). Aki and Richards (2002, eq. 6.9) give the Sommerfeld-integral expression of a spherical wave as an integral over all positive horizontal slowness values p

$$\frac{1}{R}e^{i\omega\frac{R}{\alpha_1}} = i\omega\int_0^\infty \frac{p}{q}J_0(\omega pr)e^{i\omega q|z|}dp \ , \tag{3.27}$$

where q denotes the vertical slowness that relates to the horizontal slowness p as $q = \sqrt{\frac{1}{\alpha_1^2} - p^2}$, α_1 denotes the compressional wave velocity of the medium, J_0 is the Bessel function of the first kind and order zero and R is given by the horizontal coordinate r and the vertical downwards pointing coordinate z by $R = \sqrt{r^2 + z^2}$.

Assuming harmonic excitation, the displacement potential of an explosion point source located at $z = r = 0$ is (Müller, 2007, eq. 3.80)

$$\Phi = \frac{1}{R}e^{i\omega\left(t - \frac{R}{\alpha_1}\right)}, \tag{3.28}$$

which can be expressed as an integral over horizontal slowness p using the Sommerfeld integral (Müller, 2007, cf. eq. D.5)

$$\Phi = \frac{1}{R}e^{i\omega\left(t - \frac{R}{\alpha_1}\right)} = -i\omega\int_0^\infty \frac{p}{q}J_0(\omega pr)e^{i\omega(t - qz)}dp \ . \tag{3.29}$$

It is also possible to express the potential as an integral over incidence angle θ, which is related to the horizontal slowness $p = \frac{\sin\theta}{\alpha_1}$ and the vertical slowness $q = \frac{\cos\theta}{\alpha_1}$. With

$dp = \frac{\cos\theta}{\alpha_1} d\theta$, it follows that

$$\Phi = \frac{1}{R} e^{i\omega\left(t-\frac{R}{\alpha_1}\right)} = -\frac{i\omega}{\alpha_1} \int_{\Gamma} \sin\theta J_0\left(\frac{\sin\theta}{\alpha_1}\omega r\right) e^{i\omega\left(t-z\frac{\cos\theta}{\alpha_1}\right)} d\theta \ , \tag{3.30}$$

where the integration path Γ goes along the real axis from 0 to $\frac{\pi}{2}$ and then parallel to the imaginary axis from $\frac{\pi}{2} + i0$ to $\frac{\pi}{2} + i\infty$. In that way, homogeneous and inhomogeneous plane waves can be included (see Tsvankin (1995), Aki and Richards (2002) and Müller (2007) for details).

We can now use the Sommerfeld integral to compute the full spherical-wave response observed at a receiver that is located at a depth z_R and a horizontal distance r. In section 3.2.4, the computation of the full wavefield $W(z_R)$ at receiver level z_R was derived including the direct wave, reflections from subsurface layers and reflections from the free surface. $W(z_R, \theta, \omega)$ represents the plane-wave response for a specific incidence angle θ, determining a constant horizontal slowness or ray parameter $p = \frac{\sin\theta}{\alpha_1}$, and a radial frequency ω. The transition to impulse excitation from harmonic excitation requires a multiplication with the spectrum of the source excitation function $\hat{F}(\omega)$ in frequency domain (Müller, 2007). See section 3.2.5 for the details of the computation of $\hat{F}(\omega)$. The Fourier transform of the potential $\hat{\Phi}(z_R, r, \omega)$ of the full-wavefield response at z_R and r is then given by

$$\hat{\Phi}_{3D}(z_R, r, \omega) = -\frac{i\omega}{\alpha_1} \hat{F}(\omega) \int_{\Gamma} \sin\theta J_0\left(\frac{\sin\theta}{\alpha_1}\omega r\right) W(z_R, \theta, \omega) d\theta \ . \tag{3.31}$$

The phase terms for correct travel times to the receiver are already included in $W(z_R, \theta, \omega)$ (see section 3.2.4).

The Fourier transform of the pressure response for wave propagation in 3D $\hat{P}_{3D}$ can be derived from the potential as

$$\hat{P}_{3D}(z_R, r, \omega) = \rho_1 \omega^2 \hat{\Phi}_{3D}(z_R, r, \omega) = -\frac{i\omega^3 \rho_1}{\alpha_1} \hat{F}(\omega) \int_{\Gamma} \sin\theta J_0\left(\frac{\sin\theta}{\alpha_1}\omega r\right) W(z_R, \theta, \omega) d\theta \ , \tag{3.32}$$

where ρ_1 is the density of the medium in which the receiver is located.

The horizontal displacement $\hat{u}_{3D}$ in the Fourier domain is derived from the potential as

$(J_0'(x) = -J_1(x))$

$$\begin{aligned}\hat{u}_{3D}(z_R, r, \omega) = \frac{\partial \hat{\Phi}(z_R, r, \omega)}{\partial r} &= \frac{i\omega^2}{\alpha_1^2}\hat{F}(\omega)\int_\Gamma \sin^2\theta J_1\left(\frac{\sin\theta}{\alpha_1}\omega r\right) W(z_R, \theta, \omega)d\theta \\ &= \frac{i\omega^2}{\alpha_1^2}\hat{F}(\omega)\int_\Gamma \sin\theta J_1\left(\frac{\sin\theta}{\alpha_1}\omega r\right) W^{hor}(z_R, \theta, \omega)d\theta \ ,\end{aligned} \tag{3.33}$$

where $W^{hor}(z_R, \theta, \omega) = \sin\theta W(z_R, \theta, \omega)$ (cf. section 3.2.4).

The vertical displacement $\hat{v}_{3D}$ in the Fourier domain is derived from the potential as

$$\begin{aligned}\hat{v}_{3D}(z_R, r, \omega) = \frac{\partial \hat{\Phi}(z_R, r, \omega)}{\partial z} &= -\frac{i\omega}{\alpha_1}\hat{F}(\omega)\int_\Gamma \sin\theta J_0\left(\frac{\sin\theta}{\alpha_1}\omega r\right)\frac{\partial W(z_R, \theta, \omega)}{\partial z}d\theta \\ &= \frac{\omega^2}{\alpha_1^2}\hat{F}(\omega)\int_\Gamma \sin\theta J_0\left(\frac{\sin\theta}{\alpha_1}\omega r\right) W^{ver}(z_R, \theta, \omega)d\theta\end{aligned} \tag{3.34}$$

with $W^{ver}(z_R, \theta, \omega)$ defined in section 3.2.4.

Amundsen and Reitan (1994) give the equations needed to transform the potential for 3D wave propagation (equation (3.31)) to the potential for 2D wave propagation. The potential for 2D wave propagation is given by

$$\hat{\Phi}_{2D}(z_R, r, \omega) = -2i\hat{F}(\omega)\int_\Gamma \cos\left(\frac{\sin\theta}{\alpha_1}\omega r\right) W(z_R, \theta, \omega)d\theta \ . \tag{3.35}$$

Using the relation $\hat{P}_{2D} = \rho_1\omega^2\hat{\Phi}_{2D}$, the pressure $\hat{P}_{2D}$ can be expressed as

$$\hat{P}_{2D}(z_R, r, \omega) = -2i\omega^2\rho_1\hat{F}(\omega)\int_\Gamma \cos\left(\frac{\sin\theta}{\alpha_1}\omega r\right) W(z_R, \theta, \omega)d\theta \ . \tag{3.36}$$

The horizontal displacement for wave propagation in 2D $\hat{u}_{2D}$ in the Fourier domain is derived from the potential as

$$\begin{aligned}\hat{u}_{2D}(z_R, r, \omega) = \frac{\partial \hat{\Phi}_{2D}(z_R, r, \omega)}{\partial r} &= 2i\frac{\omega}{\alpha_1}\hat{F}(\omega)\int_\Gamma \sin\left(\frac{\sin\theta}{\alpha_1}\omega r\right)\sin\theta W(z_R, \theta, \omega)d\theta \\ &= 2i\frac{\omega}{\alpha_1}\hat{F}(\omega)\int_\Gamma \sin\left(\frac{\sin\theta}{\alpha_1}\omega r\right) W^{hor}(z_R, \theta, \omega)d\theta \ .\end{aligned} \tag{3.37}$$

The vertical displacement for wave propagation in 2D $\hat{v}_{2D}$ in the Fourier domain is derived from the potential as

$$\hat{v}_{2D}(z_R, r, \omega) = \frac{\partial \hat{\Phi}_{2D}(z_R, r, \omega)}{\partial z} = 2\frac{\omega}{\alpha_1}\hat{F}(\omega)\int_\Gamma \cos\left(\frac{\sin\theta}{\alpha_1}\omega r\right) W^{ver}(z_R, \theta, \omega)d\theta \ . \tag{3.38}$$

W^{hor} and W^{ver} are given by inserting the corresponding displacement matrices for horizontal or vertical displacement, respectively, given in equation (3.11) into equations (3.8) and (3.9) (see section 3.2.4).

For the computation of synthetic seismograms for 3D or 2D wave propagation, the integrals in equations (3.32)-(3.34) and (3.36)-(3.38) are computed numerically, e.g., by the trapezoidal method. This can be achieved once the wavefield matrix $\mathbf{W}$ has been computed for a range of angles θ and radial frequencies ω using a unit sampling as described in section 3.2.4. After computation of the integral, multiplication with the factors corresponding to equations (3.32)-(3.34) and (3.36)-(3.38) and the spectrum of the source excitation function $\hat{F}(\omega)$ (see section 3.2.5) is done. Finally, the pressure or displacement observed at a receiver located at depth z_R and source-receiver offset r is obtained in time domain by an inverse Fourier transform.

The main computational burden lies in the computation of the overall reflectivity R_D of a stratified medium (see section 3.2.3) on a regular grid of angle θ and radial frequency ω to form the matrix $\mathbf{W}$ (see section 3.2.4). The computation time increases with the number of layers. Once this matrix is computed, the generation of synthetic seismic traces is fast. Mallick and Frazer (1987) discuss the computational aspects of the reflectivity method. The use of a taper, such as a Hanning window, at the upper integration limit of the angle θ is recommended to avoid numerical artefacts.

Typically, the Sommerfeld integral is expressed as an integral over horizontal wavenumber k_x or horizontal slowness p (Aki and Richards, 2002; Müller, 2007). Other authors suggested a transformation to departing angle θ (Fuchs, 1968; Fuchs and Müller, 1971; Tsvankin, 1995). The reflectivity method as described by Fuchs and Müller (1971) restricts the integration to real angles. I found the integration over angle θ beneficial for numerical stability. One reason is the absence of a denominator that can approach zero, in contrast to equation (3.29). Furthermore, the regular sampling in angle instead of slowness seems to support numerical accuracy.

3.3 Modelling examples

Figure 3.3 shows the modelling results for a simple 3-layer model with the layer properties given in Table 3.1 with an absorbing upper model boundary, i.e., no free-surface reflections or ghosts. The source is a point source located at 20 m depth below the absorbing upper model boundary. The wavelet is a 20 Hz Ricker wavelet defined in pressure. The receivers are located at 10 m depth and the horizontal source-receiver offset

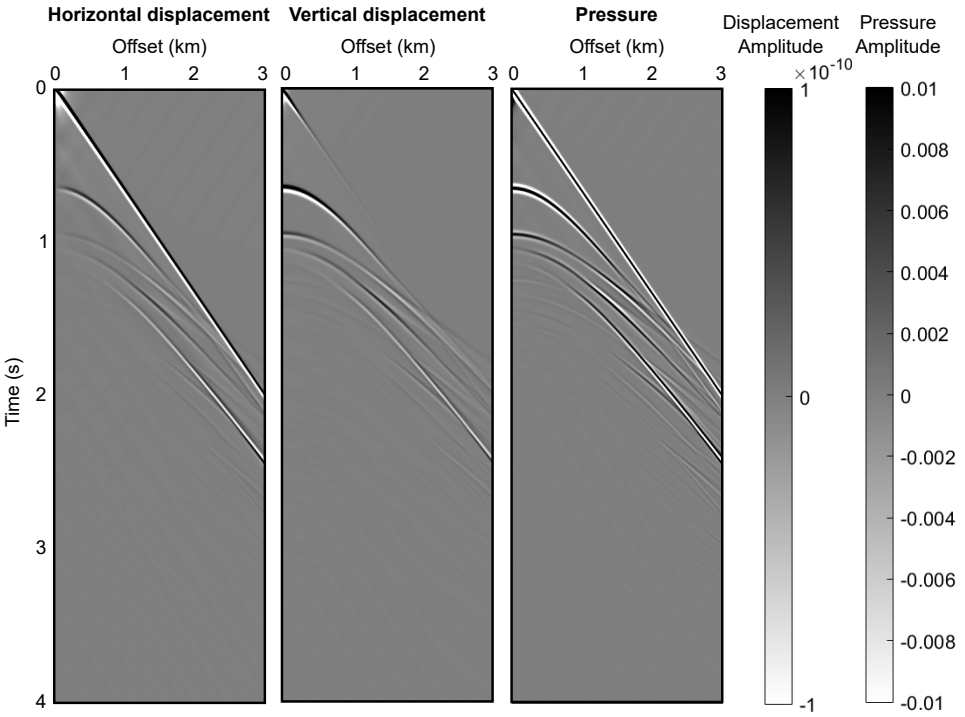

Figure 3.3: Synthetic shot gathers of a 3-layer model computed by the reflectivity method ignoring reflections at the free surface.

ranges from 0 m to 3000 m in steps of 10 m. Note the direct wave, the two primary reflections and the later arriving multiples and reflections, where at least one leg travelled as an S-wave. Refractions are also included.

	Depth of layer top (m)	V_P (m/s)	V_S (m/s)	Density (g/cm^3)
Layer 1 (water)	0	1500	0.001	1.0
Layer 2 (solid)	500	2000	1200	2.0
Layer 3 (solid)	800	3000	1800	2.2

Table 3.1: Layer properties of the 3-layer model.

The same modelling exercise has been performed with a reflective free surface and the modelling results are shown in Figure 3.4. The wavelet shape is now affected by the source and receiver ghost and the repeated pattern created by the free-surface multiples can be seen.

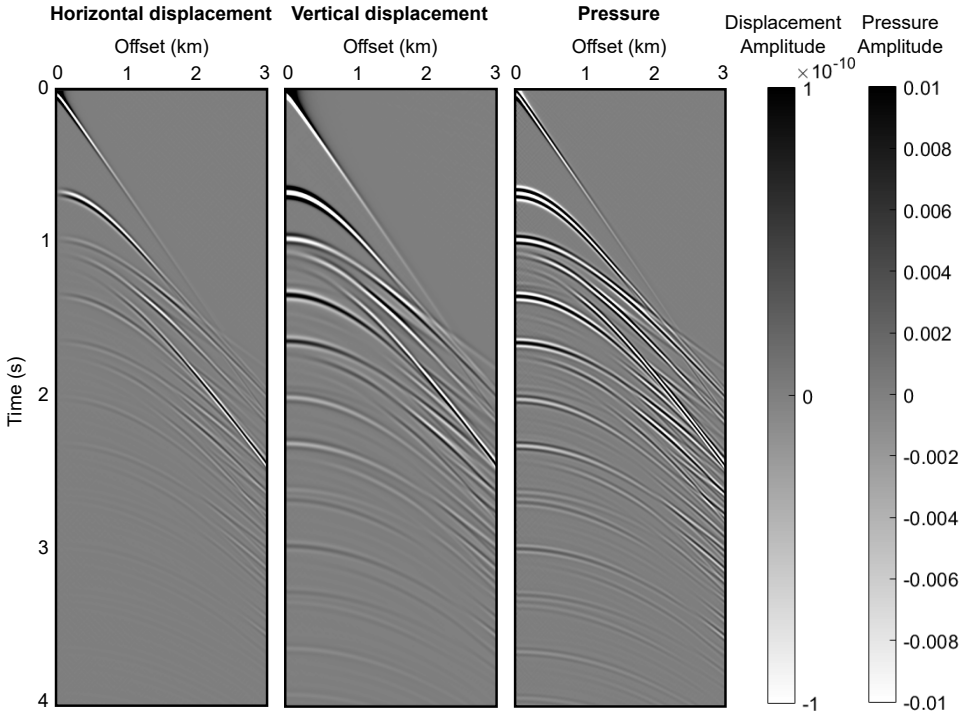

Figure 3.4: Synthetic shot gathers of a 3-layer model computed by the reflectivity method including reflections at the free surface.

3.4 Applications

As any seismic forward modelling method, the reflectivity method comes with its advantages and disadvantages. A drawback of the method is certainly its limitation to layered models (1D models). However, there are many applications, where the local assumption of a layered model can be applied, for example, in the inversion of seismic image gathers resulting from pre-stack migration (Oliveira et al., 2018; Chen et al., 2020). An extension of the reflectivity method to curved interfaces was developed by Sen and Pal (2009). Numerical challenges are another potential disadvantage (Chapman and Orcutt, 1985). The Sommerfeld integral has an oscillatory nature, which requires a dense sampling to avoid numerical inaccuracies. Pole singularities on the integration axis related to evanescent waves can lead to problems. Incorporating attenuation using complex velocities (Müller, 1985) shifts such singularities off the real slowness or angle axis (Chapman and Orcutt, 1985).

An advantage of the reflectivity method is the flexibility to model only a selected part of the wavefield and neglect unwanted parts of the wavefield, which can be useful to analyse the contributions of, e.g., internal multiples, mode conversions, free-surface multiples and ghost arrivals or transmission loss in an isolated way. Single interfaces can be easily made non-reflective by setting their reflection coefficients to zero without changing travel times or the ray bending. Likewise, transmission loss can be neglected by setting transmission coefficients to one. Even the number of reverberations can be controlled as shown in equation (3.6).

Another advantage is the possibility to choose between plane-wave and spherical-wave synthetics (cf. section 3.2.1). The plane-wave synthetics can be generated by omitting the numerical computation of the Sommerfeld integral. Instead, synthetic seismograms in the τ-p domain can be built by multiplying an overall reflectivity $R(\omega, p)$ computed in a recursive scheme (cf. sections 3.2.3-3.2.4) with a wavelet spectrum followed by an inverse Fourier transform. Angle gathers can be created afterwards by normal moveout correction and by transforming slowness in layer i, $p_i = \frac{\sin\theta_i}{\alpha_i}$, to angle θ_i using the P-wave velocity α_i. Combined with an efficient, vectorised computation scheme for the overall reflectivity, synthetic plane-wave angle gathers generated in this way have been used for pre-stack AVO inversion (Liu et al., 2016; Oliveira et al., 2018; Liu et al., 2020; Chen et al., 2020). In contrast to classical primaries-only convolutional modelling of AVO (Russell, 1988) as currently implemented in most industry software packages, the plane-wave synthetics from the reflectivity method contain the full response of a layered medium including internal multiples, transmission loss and mode conversions. It should be noted that the plane-wave angle gathers are applicable in the far field and as

long as no critical angle is approached. As discussed in section 3.2.1, the plane-wave reflection coefficient deviates from the spherical-wave reflection coefficient close to and at the critical angle. The computational effort for the synthesis of spherical-wave angle gathers is much higher compared to their plane-wave counterparts because the following additional steps are required (Oliveira et al., 2018):

- numerical integration along slowness or angle axis, which requires a dense sampling to avoid aliasing (Mallick and Frazer, 1987)
- normal moveout and geometrical spreading correction or pre-stack migration
- offset-to-angle mapping by ray tracing.

The high computational effort is limiting the usage of spherical-wave synthetics in pre-stack AVO inversion to date (Oliveira et al., 2018). Recently, there has been some research interest in the usage of frequency information contained in spherical-wave reflection coefficients (SRCs) (Li et al., 2017; Cheng et al., 2020; Yan et al., 2020). SRC-based AVO inversion can be applied also to near and critical offsets, where plane-wave-based AVO fails (Yan et al., 2020). The expectation is that SRC-based AVO inversion can improve the density estimation because of the inclusion of wider angles (Downton and Ursenbach, 2006). However, this still needs to be proven in practice. In AVO inversion using 1.5D wave-equation-based modelling, the inclusion of wider angles leads only to small improvements (Gisolf and Haffinger, 2022). Another possibility is the decomposition of an observed spherical wavefield into plane waves by a τ-p transform so that plane-wave AVO can be applied (Zhu and McMechan, 2015).

The reflectivity method has been successfully applied to models composed of thin layers (Wapenaar et al., 1999; Ursin and Stovas, 2002; Stovas et al., 2006) and for seismic-well ties (Liu et al., 2018b; Philip et al., 2018). Thanks to its lower computational cost compared to finite-difference modelling, the reflectivity method has the potential to be used in Monte Carlo simulations, as demonstrated in Articles II and III, and to produce training data for supervised machine learning (Das et al., 2019; Zheng, 2019).

The synthetic seismic data modelled by the reflectivity method are highly accurate if suitable numerical parameters are chosen (adequate sampling in angle/slowness and frequency domain, adequate angle/slowness range). For this reason, the method has been frequently applied as a reference or benchmark (Daley and Hron, 1982; Stephen, 1983; Levander, 1988; Yang et al., 2002) as also shown in Article I.

Chapter 4

Amplitude variation with offset

The principles of amplitude variation with offset (AVO) are briefly explained in this chapter. For more details, the reader is referred to the books by Castagna and Backus (1993), Chopra and Castagna (2014) and Simm and Bacon (2014). Avseth et al. (2005) give an excellent review of the technique and the pitfalls in its application.

4.1 Angle-dependent reflectivity

If a plane P-wave impinges on a single interface at non-vertical incidence, its energy is partitioned into a reflected P-wave, a reflected S-wave, a transmitted P-wave and a transmitted S-wave (Figure 4.1). The reflection and transmission coefficients are a function of the incidence angle and the material properties of the upper and lower medium. The Knott-Zoeppritz equations (Knott, 1899; Zoeppritz, 1919) give the plane-wave reflection and transmission coefficients at a single interface. Because these equations are complicated, several approximations have been developed.

Richards and Frasier (1976) and Aki and Richards (1980) derived a well-known approximation for the P-wave reflection coefficient $R(\theta) = R_{PP}(\theta)$ under the assumption of weak contrasts in the material properties of the upper and lower medium

$$R(\theta) \approx \frac{1}{2}\left(1 - 4\frac{V_S^2}{V_P^2}\sin^2\theta\right)\frac{\Delta\rho}{\rho} + \frac{1}{2\cos^2\theta}\frac{\Delta V_P}{V_P} - \left(4\frac{V_S^2}{V_P^2}\sin^2\theta\right)\frac{\Delta V_S}{V_S}\ , \tag{4.1}$$

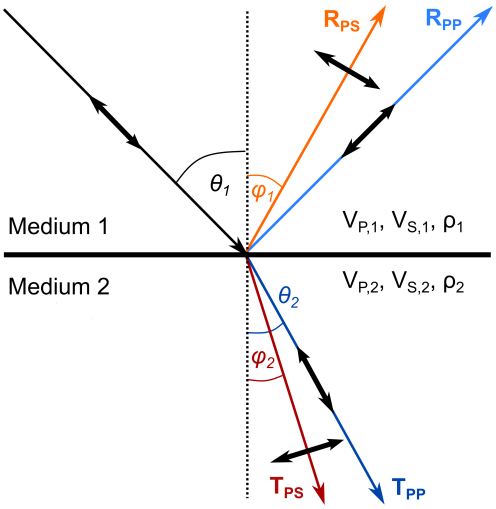

Figure 4.1: Sketch illustrating the energy partitioning of a plane P-wave incident on an interface at angle θ_1 with the normal. The interface separates two homogeneous media with the respective P-wave velocity V_P, S-wave velocity V_S and density ρ. A reflected P-wave with reflection coefficient R_{PP}, a reflected S-wave (R_{PS}), a transmitted P-wave (T_{PP}) and a transmitted S-wave (T_{PS}) are generated. The angular relationships follow Snell's law. The black double arrows indicate the direction of particle motion. Redrawn after Chopra and Castagna (2014).

where

$$\Delta V_P = V_{P,2} - V_{P,1}, \quad \Delta V_S = V_{S,2} - V_{S,1}, \; \Delta\rho = \rho_2 - \rho_1,$$
$$V_P = \frac{V_{P,1} + V_{P,2}}{2}, \quad V_S = \frac{V_{S,1} + V_{S,2}}{2}, \; \rho = \frac{\rho_1 + \rho_2}{2} \text{ and } \theta = \frac{\theta_1 + \theta_2}{2} \; .$$

In practice, the average angle θ is often replaced by the incidence angle θ_1. In that case, the approximation becomes less accurate at larger angles (Chopra and Castagna, 2014).

Shuey (1985) rearranged the Aki-Richards approximation to a three-term equation

$$R(\theta) \approx R_0 + \left(A_0 R_0 + \frac{\Delta\sigma}{(1-\sigma)^2} \right) \sin^2\theta + \frac{1}{2}\frac{\Delta V_P}{V_P} \left(\tan^2\theta - \sin^2\theta \right) \; , \tag{4.2}$$

where σ denotes the Poisson's ratio,

$$\Delta\sigma = \sigma_2 - \sigma_1, \; \sigma = \frac{\sigma_1 + \sigma_2}{2}, \; R_0 = \frac{1}{2}\left(\frac{\Delta V_P}{V_P} + \frac{\Delta\rho}{\rho} \right),$$
$$A_0 = B - 2\,(1+B)\,\frac{1-2\sigma}{1-\sigma}, \; B = \frac{\frac{\Delta V_P}{V_P}}{\frac{\Delta V_P}{V_P} + \frac{\Delta\rho}{\rho}}.$$

The three terms describe the reflectivity at normal incidence, intermediate angles, and wide angles approaching the critical angle, respectively. For θ <30°, the third term can be dropped (Shuey, 1985) resulting in the two-term approximation

$$R(\theta) \approx R(0) + G \sin^2 \theta \ , \tag{4.3}$$

where $R(0) = R_0$ denotes the P-wave reflectivity at normal incidence, called the AVO intercept, and

$$G = A_0 R_0 + \frac{\Delta\sigma}{(1-\sigma)^2} \tag{4.4}$$

is called the AVO gradient. At intermediate angles $\theta_1 < 30°$, the average angle θ can be replaced by the incident angle θ_1 (Chopra and Castagna, 2014).

4.2 AVO analysis

Before the advent of AVO technology, bright-spot technology was used as a tool in hydrocarbon exploration. It had been observed that high amplitudes visible as bright spots coincided often with gas-filled sands in the Gulf of Mexico (Avseth et al., 2005). However, not all bright spots are related to the accumulation of gas. Ostrander (1984) demonstrated that the Poisson's ratio has a strong impact on the variation of seismic amplitudes with offset. Because the presence of gas decreases the Poisson's ratio, analysis of the AVO can help to distinguish between gas-related amplitude anomalies and other types of bright spots. Shuey (1985) showed analytically using an approximation of the Knott-Zoeppritz equation how the contrast in Poisson's ratio between the upper and lower medium affects the angle-dependent reflection coefficient (see equation (4.2)).

The AVO analysis technology developed in the 1980s and 1990s draws heavily on the simple linear regression described by the 2-term Shuey equation (4.3) (Simm and Bacon, 2014). Consequently, the AVO attributes intercept $R(0)$ and gradient G are commonly used to describe the seismic AVO. Intercept and gradient can further be combined to give additional attributes, such as the product $R(0) \times G$.

For AVO analysis, the seismic data need to be processed in an AVO-friendly manner so that true relative amplitudes are preserved (Avseth et al., 2005). Chopra and Castagna (2014) elaborate on the different factors that may affect seismic amplitudes and on seismic data processing for AVO analysis. One important process to mention is normal moveout correction that flattens the primary reflections. If amplitudes are picked at a constant time or depth, residual moveout can lead to errors. Amplitude-preserving pre-stack depth migration is a good choice for AVO processing, especially in areas with

structural complexity (Avseth et al., 2005).

Seismic data are measured as a function of source-receiver offset. To relate the observed AVO to angle-dependent reflectivity, a mapping from offset to reflection angle is required. For this mapping, a velocity model is used. The reflection angle at a specific location given a source-receiver offset can be found by ray tracing. An estimate of the reflection angle for horizontally layered media can be computed by the Dix formula (Dix, 1955) using root-mean-square velocities (Simm and Bacon, 2014).

The calculation of AVO intercept and gradient using the two-term Shuey approximation (equation 4.3) is illustrated in Figure 4.2. As discussed, it is important to restrict the angle range to maximum 30°, where the two-term approximation is appropriate. An important aspect is the scaling of seismic amplitudes to reflection coefficients, which is usually done by well ties (Simm and Bacon, 2014).

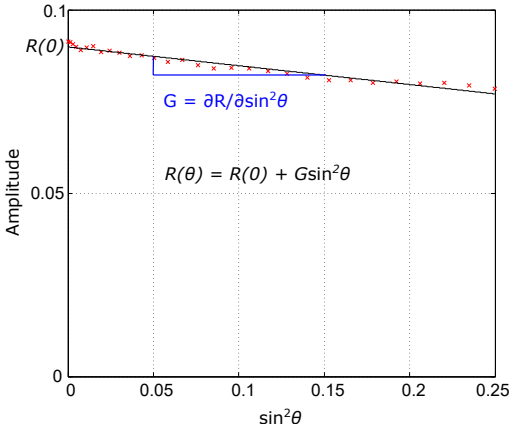

Figure 4.2: Illustration of fitting a linear function to picked amplitudes (red crosses) to obtain the AVO intercept $R(0)$ and the AVO gradient G.

A common way to visualise AVO responses is to plot AVO intercept and gradient in an AVO crossplot as shown in Figure 4.3. Rutherford and Williams (1989) classified the AVO responses of shale–gas-sand interfaces into three classes I, II and III (see Figure 4.3). Ross and Kinman (1995) suggested a class IIp for small positive intercept class II responses with an inherent phase reversal. Another category, class IV, was introduced by Castagna and Swan (1997) for responses showing a large negative incident and a decreasing absolute amplitude with offset. Originally developed for classifying AVO types of hydrocarbon-bearing sands, the mentioned AVO classes are used for describing AVO behaviour generally (Simm and Bacon, 2014).

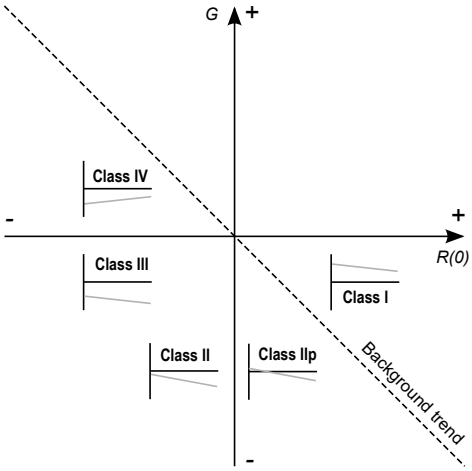

Figure 4.3: AVO classes and their location in the AVO crossplot. For each class, the characteristic amplitude trend for increasing $\sin^2\theta$ is shown. Redrawn after Castagna et al. (1998) and Avseth et al. (2005).

An alternative is the generation of angle stacks, where data of a specified angle range are stacked to create angle sub-stacks in addition to the full stack. An example of near and far angle stacks is shown in Figure 4.4. Angle stacks can be interpreted directly or they can be used as an input data for pre-stack seismic inversion.

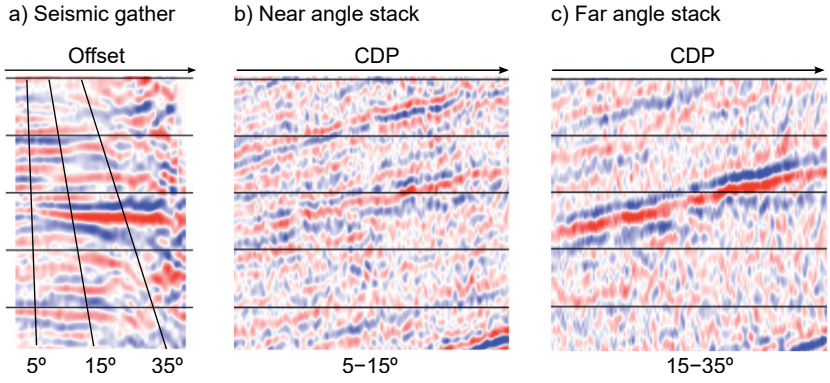

Figure 4.4: Near angle (5–15°) and far angle (15–35°) stacks are created by stacking the seismic data of the specific angle ranges. Modified after Simm and Bacon (2014).

Chapter 5

Statistical methods for seismic reservoir characterisation

This chapter introduces the statistical methods that were applied in Article II and Article III. The field of statistical methods used in seismic reservoir characterisation is wide. A good overview is given in the books by Doyen (2007) and Grana et al. (2021). Avseth et al. (2005) cover the concepts of statistical rock physics.

5.1 Bayesian inversion

The inverse problem in geophysics is to find a model $\mathbf{m}$ that can explain the observed data $\mathbf{d}$. This problem can be formulated as

$$\mathbf{d} = \mathbf{f}(\mathbf{m}) + \epsilon, \tag{5.1}$$

where $\mathbf{f}$ is the forward operator, typically a set of physical equations, and ϵ denotes the measurement error and noise of the data (Grana et al., 2021). Solving the inverse problem in a probabilistic sense corresponds to estimating the conditional probability distribution $p(\mathbf{m} \mid \mathbf{d})$. This can be achieved by applying Bayes' theorem

$$p(\mathbf{m} \mid \mathbf{d}) = \frac{p(\mathbf{d} \mid \mathbf{m})p(\mathbf{m})}{p(\mathbf{d})} = \frac{p(\mathbf{d} \mid \mathbf{m})p(\mathbf{m})}{\int p(\mathbf{d} \mid \mathbf{m})p(\mathbf{m})d\mathbf{m}} \, . \tag{5.2}$$

In Bayesian vocabulary, the conditional probability $p(\mathbf{m} \mid \mathbf{d})$ is called the posterior probability that is computed from the prior probability distribution $p(\mathbf{m})$, the likelihood function $p(\mathbf{d} \mid \mathbf{m})$ and the normalising marginal distribution $p(\mathbf{d})$.

If there is a linear operator $\mathbf{f}$ and if the prior $p(\mathbf{m})$ and the measurement error ϵ are Gaussian, the posterior probability distribution $p(\mathbf{m} \mid \mathbf{d})$ is also Gaussian (Tarantola, 2005). These assumptions are often used to solve seismic inversion problems (Grana et al., 2021). Bayesian linearised AVO inversion was developed by Buland and Omre (2003) using a linear forward operator by convolutional seismic modelling.

If the operator $\mathbf{f}$ is not linear, the posterior distribution can be found by stochastic simulation techniques, such as Monte Carlo sampling (Mosegaard and Tarantola, 1995). With the increase in computing power, Monte Carlo simulation has become a popular method for solving various probabilistic problems (Avseth et al., 2005). The basic idea is to draw a large number of samples from a given probability distribution and to apply a (generally non-linear) operator to the samples to estimate the desired probability distribution. Sequential Monte Carlo simulation is typically realised by Markov chains (Liu, 2004).

5.2 Bayesian classification

A classification problem can be regarded as a special type of inverse problem, where the goal is to predict a category rather than inverting for continuous model variables. In seismic reservoir characterisation, classification is often applied to categorise input data into lithofacies or pore-fluid classes (Avseth et al., 2005). One way to approach a classification problem is to apply Bayesian decision theory (Duda, 2001).

Let c_j, $j = 1, ..., N$ denote N different classes, for example, the pore fluids brine, oil and gas. The classification is done based on input data x. For example, this could be the AVO intercept and gradient. The posterior probability of a particular class c_j given an observed input data point x is according to Bayes' theorem given by

$$p\left(c_j \mid x\right) = \frac{p\left(x \mid c_j\right) p\left(c_j\right)}{p(x)} \ , \tag{5.3}$$

where $p\left(x \mid c_j\right)$ denotes the conditional probability of x given class c_j, $p\left(c_j\right)$ denotes the prior probability of class c_j and $p(x)$ is a normalising constant to guarantee that the sum of probabilities over all classes is one (Avseth et al., 2005). Relation (5.3) updates a given prior probability of a class to a posterior probability by using a class-conditional probability distribution estimated from measured or simulated training data (Avseth et al., 2005). Figure 5.1 shows an example of estimated probability density functions of the AVO intercept and gradient for three different pore-fluid classes.

The classification based on the estimated posterior probabilities $p(c_j \mid x)$ can be done

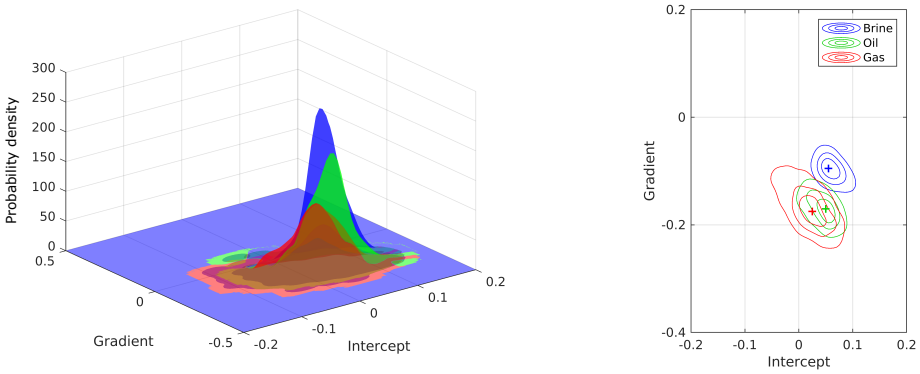

Figure 5.1: Class-conditional probability density functions of AVO intercept and gradient for the three pore-fluid classes brine (blue), oil (green) and gas (red) shown as surface plot (left) and contour plot (right). The right figure was modified after Tschache et al. (2023).

using Bayes' decision rule

$$c_k = \underset{j=1,\ldots,N}{\operatorname{argmax}}\ p(c_j \mid x)\ . \tag{5.4}$$

This decision rule maximises the posterior probability and minimises the misclassification error and should be applied when the loss associated with each misclassification type is equal (Avseth et al., 2005). In a hydrocarbon exploration setting, the losses associated with a dry hole compared with a missed hydrocarbon accumulation are different and the decision rule can be changed to reflect the corresponding financial losses (Avseth et al., 2005).

Typically, the class-conditional probability density functions $p\,(x \mid c_j)$ will show some overlap (as shown in Figure 5.1) leading to a non-perfect classification. Classification confusion matrices allow the analysis of success rates and the different kinds of misclassification. An example of a confusion matrix is shown in Figure 5.2. Each element p_{ij} represents the conditional probability that the true class is c_i when the predicted class is c_j, $p_{ij} = (\text{true class} = i \mid \text{predicted class} = j)$. Confusion matrices can be computed from training data using the "leave-one-out" jackknife technique or by using validation datasets (Avseth et al., 2005). The accuracy of statistical estimates, such as success rates, can be computed by bootstrapping (Efron, 1979).

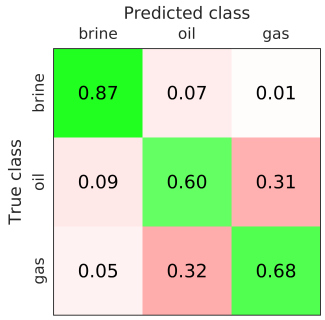

Figure 5.2: Confusion matrix for a Bayesian classification of pore-fluid types. Diagonal elements represent probabilities of correct classification, while off-diagonal elements represent misclassification probabilities. The colour intensity is scaled according to the respective probability value. Modified after Tschache et al. (2023).

5.3 Geostatistical simulation

Geostatistical tools have been originally developed for mining engineering problems in the 1950s and have since then been applied to many domains in Earth sciences (Grana et al., 2021). In seismic reservoir characterisation, geostatistical methods are typically used to interpolate reservoir properties spatially between wells by integrating seismic data. In Article III, geostatistical simulation methods are applied to generate pseudo-wells based on statistical properties from well measurements. The next paragraphs briefly describe the methods that were applied in Article III. Detailed explanations can be found in the cited books.

Variograms (or semivariograms) are typical input parameters of geostatistical simulation. A variogram measures the dissimilarity of a variable with increasing distance h. Given a dataset of a continuous variable $\mathbf{x}$, the experimental variogram $\gamma(h)^*$ can be computed as

$$\gamma(h)^* = \frac{1}{2n_h} \sum_{j=1}^{n_h} [x(\mathbf{u}_j) - x(\mathbf{u}_j + h)]^2 \ , \tag{5.5}$$

where $\mathbf{u}_j$ is a vector of spatial coordinates of data sample j and n_h is the number of pairs of data points separated by distance h. The variogram $\gamma(h)$ is related to the spatial covariance function $C(h)$ by

$$\gamma(h) = C(0) - C(h) \ . \tag{5.6}$$

Parametric variogram models are fitted to experimental variograms estimated from the data. The three most common models are exponential, Gaussian and spherical models

(Grana et al., 2021). A spherical variogram model as used in Article III is defined as

$$\gamma_{\text{spherical}}(h) = \begin{cases} \sigma^2 \left(\frac{3h}{2r} - \frac{h^3}{2r^3} \right) & h \leq r \\ \sigma^2 & h > r \end{cases}, \tag{5.7}$$

where σ^2 is the variance of the variable, called the sill of the variogram model, and r is called the range of the variogram model. Figure 5.3 shows an example of an experimental variogram and a fitted spherical variogram model with the sill and range indicated. For an increasing h, the variogram converges to a plateau level, which is the sill. The range (or correlation range) r is the distance at which the plateau is reached. Data values beyond the range are uncorrelated.

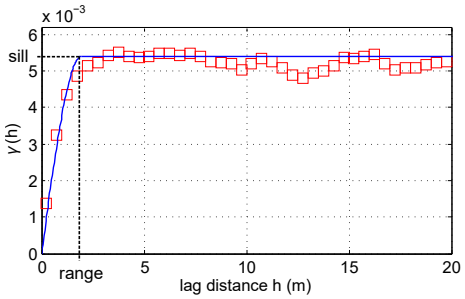

Figure 5.3: Experimental variogram (red markers) and fitted spherical variogram model (blue line) for porosity data of a well.

Sequential Indicator Simulation (SISIM) described by Deutsch and Journel (1992) is a geostatistical simulation method for categorical variables, such as facies. The method samples from a given probability mass function of the categories. At each location visited during the sequential simulation, the probability of a category is conditioned on the previously simulated samples by indicator kriging. A 1D example of SISIM is the simulation of a vertical facies model, where a specific facies is assigned to each sample in a sequential way from top to bottom.

For the simulation of continuous variables, such as porosity, Sequential Gaussian Simulation (SGSIM) is a common method (Deutsch and Journel, 1992). As the name suggests, this method assumes that the variables have a Gaussian distribution. If this is not the case, the data are transformed to normal scores before simulation (Goovaerts, 1997). During SGSIM, simple kriging estimates are computed based on direct measurements and previously simulated values (Grana et al., 2021). The simulated normal scores are then back-transformed.

Chapter 6

Summaries of the articles

6.1 Article I

S. Tschache, V. Vinje, E. Iversen, *On the accuracy and spatial sampling of finite-difference modelling in discontinuous models*, Journal of Applied Geophysics **206**, 104789, 2022.

Seismic finite-difference (FD) modelling solves the wave equation numerically by approximating derivatives by finite differences. The accuracy of a 2D acoustic central-grid pseudospectral scheme was investigated for several discontinuous models: a step model, a single thin-layer model and a multi-layer model. To evaluate the accuracy, the FD simulation results were compared to the analytic result of the step model and the semi-analytic results of the reflectivity method for the thin-layer and multi-layer models. We analysed the normalised amplitude spectra and phase difference vs. frequency.

For an aliasing-free representation of discontinuities in a regular grid, a tapered low-pass wavenumber filtering procedure was devised. The cut-off wavenumber of the filter is the Nyquist wavenumber of the desired grid. The length of the filter operator is controlled by the adaptable taper size. The filter is applied to densely sampled models of compliance and density. The filtering procedure can also be used to upscale (downsample) well logs. More accurate FD modelling results were achieved with upscaled models by the proposed method compared to upscaling by Backus averaging (Backus, 1962), which is the conventional method.

The FD modelling accuracy was investigated for a varying grid sampling interval, which has a huge impact on the computational cost of the simulation. We found that a spatial sampling of 4-5 grid points per shortest wavelength is generally sufficient for high

accuracy throughout the full bandwidth of the signal. In case of thin layers with strong impedance contrasts, a denser grid sampling is needed to obtain full bandwidth accuracy also at wide angles.

The conclusions of this study are directly applicable to an optimal grid representation of discontinuities, such as the seabed or sediment-salt interfaces. The sampling recommendation concluded from the study is relevant for central-grid FD schemes, that are widely used in the seismic industry as part of full waveform inversion or reverse time migration. Furthermore, the suitability of the reflectivity method as an accurate and computationally efficient full-wavefield seismic modelling tool for layered media is demonstrated.

6.2 Article II

S. Tschache, V. Vinje, J. E. Lie, E. Iversen, *Quantifying amplitude-variation-with-offset uncertainties related to calcite-cemented beds using a Monte Carlo simulation*, Interpretation **11**(2), T315–T329, 2023.

Calcite cementation is often observed locally in shallow marine sandstones forming concretions or thin beds of calcite-cemented rock. Calcite-cemented beds are characterised by a high acoustic impedance and typical thicknesses in the range 0.1-1.5 m. Owing to their strong acoustic impedance contrast with the surrounding rock, calcite-cemented beds produce detectable seismic reflection signals which might interfere with target reflections at the top of a reservoir. In such a case, the amplitude variation with offset (AVO) of the observed seismic signature will be perturbed and may even lead to a false hydrocarbon indication.

Pore fluids can be predicted by a Bayesian classification of the AVO attributes intercept and gradient. If the AVO attributes are potentially altered by the interference with seismic responses of calcite-cemented beds, the pore-fluid prediction will be impaired. Therefore, a workflow was devised that allows the quantification of the uncertainty of AVO-based pore-fluid discrimination associated with calcite-cemented beds. The workflow uses well data to extract regional rock-physical properties and is demonstrated using a case example of the Alvheim field on the Norwegian Continental Shelf. Two types of models are generated, where calcite-cemented beds are either absent or present. Many realisations of these models are considered in a Monte Carlo simulation. Synthetic seismic angle gathers are computed and the AVO attributes at the top of the reservoir are extracted.

A crucial element of the workflow is the seismic forward modelling method that is used

as part of the Monte Carlo simulation. It is demonstrated that convolutional modelling using plane-wave reflection coefficients fails for models that contain calcite-cemented beds, while the reflectivity method generates correct synthetics.

It was observed that the uncertainty of the pore-fluid classification increases significantly when calcite-cemented beds are present. In the case example, the probability of a false hydrocarbon indication increases from 3–5 % to 18–21 % due to the presence of calcite-cemented beds. A Bayesian classifier based on models that contain calcite-cemented intervals performed slightly better than a classifier based on models without calcite-cemented intervals when tested at well locations.

The study shows that calcite-cemented beds can create a serious AVO pitfall. The presence of such thin, hard beds should not be ignored in a pore-fluid prediction. Otherwise, the uncertainty will be underestimated. The proposed workflow provides useful uncertainty estimates for the pre-drilling risk assessment of AVO anomalies.

6.3 Article III

S. Tschache, V. Vinje, J. E. Lie, M. Brandtzæg Gundem, E. Iversen, *Estimation of net-to-gross ratio and net pay from seismic amplitude variation with offset using Bayesian inversion*, submitted to Interpretation 5 April 2023.

Turbidite reservoirs are characterised by a sand-shale interbedding which is typically below the seismic resolution. Essential properties in reservoir characterisation are the net-to-gross ratio, the ratio of net sand of a gross reservoir thickness, and the net pay, which comprises the sand intervals that are sufficiently saturated by hydrocarbons for economic production. The estimation of these reservoir properties in-between wells can be attempted by using seismic data, particularly the AVO information.

We present a Bayesian inversion that estimates a bivariate probability density function of net-to-gross ratio and net-pay-to-net ratio given the AVO intercept and gradient measured from the seismic reflection at the reservoir top. The statistical characteristics of sand and shale layers are derived from well data of a specific field. These properties are used to create many pseudo-wells consisting of sand and shale layers. As seismic modelling method, a variant of the reflectivity method is used that produces plane-wave synthetic angle gathers. Because of the moderate acoustic impedance contrasts in the pseudo-wells consisting of sand and shale beds, the plane-wave synthetics are suitable. A Monte Carlo simulation is used to estimate probability density functions of AVO intercept and gradient from many pseudo-wells with varying reservoir properties. In this

way, a likelihood function is estimated that is combined with the prior probabilities of the reservoir properties.

The inversion was successfully tested on pseudo-wells and then applied to synthetic seismic AVO at well locations, where the inversion results were robust. Finally, the inversion was applied to AVO attribute maps produced from seismic field data. Maps of the most likely values of the net-to-gross ratio, the net-pay-to-net ratio, the resulting net pay and the uncertainty could be generated. Such maps can add useful information in the screening for zones of high reservoir quality and hydrocarbon saturation.

Chapter 7

Conclusion, discussion and outlook

7.1 Conclusion

Article I demonstrates the feasibility of the reflectivity method as a benchmark modelling tool for finite-difference modelling in horizontally layered media. It could be shown that the finite-difference modelling results approach the benchmark with decreasing spatial sampling interval. Consequently, the reflectivity method provides an accurate and computationally cheaper alternative to finite-difference modelling in horizontally layered models.

An aliasing-protected resampling (upscaling) method for regularly sampled models is proposed in Article I. This method allows to integrate discontinuities in the model grid that are smaller than the grid spacing. It has been shown that grids produced by this method yield more accurate finite-difference modelling results than upscaled grids obtained from Backus averaging.

Articles II and III show the potential failure of convolutional seismic modelling in thin-bedded geology. In both articles, it is demonstrated how the reflectivity method can be used to generate accurate synthetic angle gathers. Although such a full-wavefield modelling requires more computation time than convolutional modelling, the suitability for Monte Carlo simulation is proven.

In Article II, it is shown that thin, hard layers that are well below the seismic resolution can alter the seismic signatures and AVO considerably. A workflow is presented that allows to assess the uncertainty of AVO-based pore-fluid prediction in the presence of thin high-impedance layers. The interference with reflection responses from thin high-impedance layers increases the uncertainty of the pore-fluid prediction significantly and

therefore increases the probability of a false positive hydrocarbon indication.

In Article III, the estimation of reservoir properties of turbidite reservoirs from seismic AVO attributes measured at the top of a reservoir is demonstrated. A Bayesian inversion is presented that estimates the probability density function of the reservoir properties net-to-gross ratio and net-pay-to-net ratio. The most likely values and the uncertainty of the prediction can be assessed in this way. In the case example, the AVO gradient is correlated with the net-to-gross ratio, while the AVO intercept is most sensitive to the pore-fluid type.

Sub-seismic heterogeneity is one reason for uncertainty in quantitative seismic interpretation. In this thesis, I therefore advocate the use of probabilistic methods to account for the inherent non-uniqueness of quantitative interpretation of band-limited seismic data. Furthermore, inappropriate seismic modelling can lead to significant errors. I show in this thesis the advantages of full-wavefield elastic seismic modelling by the reflectivity method for AVO studies. The thesis demonstrates how full-wavefield seismic modelling can be integrated with Bayesian methods for quantitative seismic interpretation.

7.2 Discussion and outlook

The central method for seismic forward modelling in this thesis is the reflectivity method. In chapter 3, it is discussed how shot gathers can be generated by this method. For producing synthetic angle gathers as used in AVO studies, there are two variants applied in this thesis. The first variant is the generation of spherical-wave shot gathers by the reflectivity method, followed by a Kirchhoff pre-stack depth migration and an offset-to-angle mapping as applied in Article II. The second variant can be regarded as a shortcut to produce plane-wave angle gathers, where the computation of the slowness integral is omitted as described in section 3.4. This procedure has been proposed by Oliveira et al. (2018) and was used in Article III. Plane-wave synthetics generated using the reflectivity method are commonly used (Mallick, 1999; Liu et al., 2016; Oliveira et al., 2018). However, it should be noted that spherical-wave synthetics are required when a critical angle is reached in the modelling (cf. subsection 3.2.1). In Article II, the thin high-velocity layers lead to relatively small critical angles, which makes the usage of spherical-wave synthetics necessary. The models in Article III consist of shale and sand beds with moderate contrasts in acoustic impedance allowing the usage of plane-wave synthetics.

The application of the reflectivity method requires the assumption of a horizontally

layered medium. A pre-stack migration collapses diffractions and corrects for reflector dip and curvature effects (Oliveira et al., 2018), such that the assumption of a horizontally layered subsurface can be applied locally to seismic image gathers. Recent advances of seismic migration methods, such as reverse time migration, could facilitate the usage of local 1D inversions based on the reflectivity method for targets with more complex structures (Mallick and Adhikari, 2015).

1D pre-stack seismic waveform inversions using the reflectivity method have been proposed (Sen and Stoffa, 1991; Stoffa and Sen, 1991; Zhao et al., 1994; Mallick, 1995; Sen and Roy, 2003) but the conventional pre-stack inversion remains on the basis of primaries-only convolutional modelling. Compared to convolutional modelling, forward modelling by the reflectivity method is more time-consuming and it is more complicated to compute differential seismograms (Sen and Roy, 2003; Liu et al., 2016). With the increase in computing power, pre-stack inversion on the basis of the reflectivity method gained more attention in recent years (Liu et al., 2016, 2018a; Oliveira et al., 2018; Chen et al., 2020; Yang and Lu, 2020). For better efficiency, the vectorisation by Phinney et al. (1987) is often used (Liu et al., 2016, 2018a). All the cited inversion algorithms have in common that they use plane-wave synthetics. Some of them are implemented in the τ-p domain which requires a plane-wave transformation of the input data (Sen and Stoffa, 1991; Stoffa and Sen, 1991; Sen and Roy, 2003; Zhao et al., 1994). Other inversion algorithms are directly applied to seismic angle gathers (Mallick, 1995, 1999; Liu et al., 2016, 2018a; Oliveira et al., 2018; Chen et al., 2020; Yang and Lu, 2020).

The additional effort of computing spherical-wave seismograms using the reflectivity method as opposed to plane-wave seismograms is the main reason why plane-wave synthetics are currently preferred for pre-stack inversion (Oliveira et al., 2018). Modern seismic acquisitions typically include long source-receiver offsets to support full-waveform inversion. This means that seismic reflections at or beyond the critical angle are more commonly recorded (Zhu and McMechan, 2012). To use the full angle range of the data instead of muting (post-)critical reflections, spherical-wave reflectivity must be taken into account. Some authors used spherical-wave reflectivity in pre-stack inversion (Skopintseva et al., 2011; Zhu and McMechan, 2012). A current research topic is the usage of the frequency dependence of spherical-wave reflectivity (Li et al., 2017; Yan et al., 2020; Cheng et al., 2020, 2022). Spherical-wave amplitude-variation-with-offset and -frequency inversion is still in an exploratory stage today (Cheng et al., 2022).

From a practical viewpoint, the usage of spherical-wave reflectivity in AVO studies has two application cases. The first case is seismic data recorded at a short travel distance, where the wavefront can not be regarded as a plane, e.g., in crosshole seismics, vertical seismic profiling or near-surface reflection seismics. The other use case is seismic data

recorded at wide angles that include (post-)critical angles. It is commonly expected that the inclusion of wider angles in pre-stack inversion improves the inversion results (Gisolf and Haffinger, 2022), especially for shear modulus and density. However, a recent analysis by Gisolf and Haffinger (2022) indicates that there is little improvement compared to more conventional pre-critical angle ranges. Even if post-critical reflection energy might be of limited benefit for the seismic industry and spherical-wave AVO inversion does not seem to become the industry standard soon, the widespread usage of simplistic primaries-only convolutional modelling should be reconsidered. As discussed, 1D pre-stack seismic waveform inversions based on the reflectivity method applied to muted angle gathers that contain only pre-critical reflections or applied to seismic data in the τ-p domain would be an improvement because internal multiple reflections, mode conversions and transmission loss are included. Another promising approach is the application of targeted wave-equation-based AVO inversion using an integral representation of the elastic wave equation (Gisolf et al., 2017).

Although full-waveform inversion based on finite-difference modelling has improved a lot in the past decade, the method is not yet capable of producing reservoir models of sufficient detail and accuracy (Mallick and Adhikari, 2015). As 3D elastic full-waveform inversion could become applicable at reservoir scale in the future, this method could supersede the 1D pre-stack inversions (Mallick and Adhikari, 2015).

The development of Bayesian methods for the prediction of lithology and fluid classes from seismic data has made good progress in the last twenty years (Larsen et al., 2006; Ulvmoen and Omre, 2010; Ulvmoen et al., 2010; Grana and Rossa, 2010; Kolbjørnsen et al., 2020; Grana et al., 2022). The linearised seismic forward modelling by convolution proposed by Buland and Omre (2003) is typically used with the mentioned limitations to single scattering and the plane-wave assumption. The problem of estimating reservoir properties from seismic data continues to be under active research because it is non-linear and non-unique even for the noise-free case (Das and Mukerji, 2020).

Another research direction, which is currently explored, is the application of machine learning techniques for quantitative seismic interpretation. Supervised learning of convolutional neural networks has been proposed to estimate elastic or petrophysical properties from seismic data (Das et al., 2019; Das and Mukerji, 2020). Physics-guided networks for quantitative seismic interpretation include the physics of seismic wave propagation in the training of the network (Sun et al., 2020, 2021; Biswas et al., 2019; Vashisth and Mukerji, 2022). The reflectivity method could be used as a full-wavefield modelling alternative to convolutional modelling for generating training data for supervised learning or as part of physics-guided networks.

Bibliography

Aki, K. and Richards, P. G. *Quantitative Seismology: Theory and Methods*, volume 1 and 2. W. H. Freeman and Co., San Francisco, 1980. ISBN 0716710587.

Aki, K. and Richards, P. G. *Quantitative seismology*. University Science Books, Sausalito, 2nd edition, 2002. ISBN 0935702962.

Alford, R. M., Kelly, K. R., and Boore, D. M. Accuracy of finite-difference modeling of the acoustic wave equation. *GEOPHYSICS*, 39(6): 834–842, 1974. doi: 10.1190/1.1440470.

Alhussain, M., Gurevich, B., and Urosevic, M. Experimental verification of spherical-wave effect on the AVO response and implications for three-term inversion. *GEOPHYSICS*, 73(2): C7–C12, 2008. doi: 10.1190/1.2837641.

Alkhalifah, T. An acoustic wave equation for anisotropic media. *GEOPHYSICS*, 65(4): 1239–1250, 2000. doi: 10.1190/1.1444815.

Allen, J. L., Peddy, C. P., and Fasnacht, T. L. Some AVO failures and what (we think) we have learned. *The Leading Edge*, 12(3): 162–167, 1993. doi: 10.1190/1.1436938.

Amundsen, L. and Reitan, A. Transformation from 2-D to 3-D wave propagation for horizontally layered media. *GEOPHYSICS*, 59(12): 1920–1926, 1994. doi: 10.1190/1.1443579.

Avseth, P., Mukerji, T., and Mavko, G. *Quantitative Seismic Interpretation: Applying Rock Physics Tools to Reduce Interpretation Risk*. Cambridge University Press, New York, 2005. ISBN 9780521816014.

Avseth, P., Janke, A., and Horn, F. AVO inversion in exploration — Key learnings from a Norwegian Sea prospect. *The Leading Edge*, 35(5): 405–414, 2016. doi: 10.1190/tle35050405.1.

Backus, G. E. Long-wave elastic anisotropy produced by horizontal layering. *Journal of Geophysical Research*, 67(11): 4427–4440, 1962. doi: 10.1029/JZ067i011p04427.

Biswas, R., Sen, M. K., Das, V., and Mukerji, T. Prestack and poststack inversion using a physics-guided convolutional neural network. *Interpretation*, 7(3): SE161–SE174, 2019. doi: 10.1190/INT-2018-0236.1.

Bohlen, T., Nil, D. D., Koehn, D., and Jetschny, S. *SOFI3D - seismic modeling with finite differences. 3D - acoustic and viscoelastic version. Users Guide.* Karlsruhe Institute of Technoloy, Nov. 2015.

Booth, D. C. and Crampin, S. The anisotropic reflectivity technique: theory. *Geophysical Journal International*, 72(3): 755–766, 1983. doi: 10.1111/j.1365-246X.1983.tb02831.x.

Buland, A. and Omre, H. Bayesian linearized AVO inversion. *GEOPHYSICS*, 68(1): 185–198, 2003. doi: 10.1190/1.1543206.

Carcione, J. M., Herman, G. C., and ten Kroode, A. P. E. Seismic modeling. *GEOPHYSICS*, 67(4): 1304–1325, 2002. doi: 10.1190/1.1500393.

Castagna, J. P. and Backus, M. M. *Offset-dependent reflectivity—Theory and practice of AVO analysis.* Society of Exploration Geophysicists, Tulsa, 1993.

Castagna, J. P. and Swan, H. W. Principles of AVO crossplotting. *The Leading Edge*, 16(4): 337–344, 1997. doi: 10.1190/1.1437626.

Castagna, J. P., Swan, H. W., and Foster, D. J. Framework for AVO gradient and intercept interpretation. *GEOPHYSICS*, 63(3): 948–956, 1998. doi: 10.1190/1.1444406.

Chapman, C. H. and Orcutt, J. A. The computation of body wave synthetic seismograms in laterally homogeneous media. *Reviews of Geophysics*, 23(2): 105–163, 1985. doi: 10.1029/RG023i002p00105.

Chen, L., Li, J., Chen, X., Liu, H., and Zhou, L. Prestack AVO inversion based on the vectorised reflectivity method with blockiness constraint. *Exploration Geophysics*, 51 (5): 535–548, 2020. doi: 10.1080/08123985.2020.1801082.

Cheng, G., Yin, X., and Zong, Z. Frequency-dependent spherical-wave nonlinear AVO inversion in elastic media. *Geophysical Journal International*, 223(2): 765–776, 2020. doi: 10.1093/gji/ggaa312.

Cheng, G., Yin, X., Zong, Z., Xia, T., Wang, J., and Liu, H. Seismic inversion using complex spherical-wave reflection coefficient at different offsets and frequencies. *GEOPHYSICS*, 87(2): R183–R192, 2022. doi: 10.1190/geo2020-0787.1.

Chopra, S. and Castagna, J. P. *AVO.* Society of Exploration Geophysicists, Tulsa, 2014.

Courant, R., Friedrichs, K., and Lewy, H. On the Partial Difference Equations of Mathematical Physics. *IBM Journal of Research and Development*, 11(2): 215–234, 1967. doi: 10.1147/rd.112.0215.

Daley, P. F. and Hron, F. Ray-reflectivity method for SH-waves in stacks of thin and thick layers. *Geophysical Journal International*, 69(2): 527–535, 1982. doi: 10.1111/j.1365-246X.1982.tb04963.x.

Das, V. and Mukerji, T. Petrophysical properties prediction from prestack seismic data using convolutional neural networks. *GEOPHYSICS*, 85(5): N41–N55, 2020. doi: 10.1190/geo2019-0650.1.

Das, V., Pollack, A., Wollner, U., and Mukerji, T. Convolutional neural network for seismic impedance inversion. *GEOPHYSICS*, 84(6): R869–R880, 2019. doi: 10.1190/geo2018-0838.1.

Deutsch, C. V. and Journel, A. G. *GSLIB: Geostatistical Software Library and User's Guide*. Oxford University Press, New York, 1992. ISBN 9780195073928.

Dix, C. H. Seismic velocities from surface measurements. *GEOPHYSICS*, 20(1): 68–86, 1955. doi: 10.1190/1.1438126.

Downton, J. E. and Ursenbach, C. Linearized amplitude variation with offset (AVO) inversion with supercritical angles. *GEOPHYSICS*, 71(5): E49–E55, 2006. doi: 10.1190/1.2227617.

Downton, J. E., Russell, B. H., and Lines, L. R. AVO for managers: pitfalls and solutions. Technical report, CREWES Research Report, Volume 12, 2000.

Doyen, P. *Seismic Reservoir Characterization*. European Association of Geoscientists & Engineers, Houten, 2007. ISBN 9789073781771.

Duda, R. O. *Pattern classification*. Wiley, New York, 2nd edition, 2001. ISBN 0471056693.

Efron, B. Bootstrap Methods: Another Look at the Jackknife. *The Annals of Statistics*, 7(1): 1–26, 1979. doi: 10.1214/aos/1176344552.

Fichtner, A. *Full Seismic Waveform Modelling and Inversion*. Advances in Geophysical and Environmental Mechanics and Mathematics. Springer, Berlin, Heidelberg, 2010. ISBN 9783642158063.

Fornberg, B. The pseudospectral method: Comparisons with finite differences for the elastic wave equation. *GEOPHYSICS*, 52(4): 483–501, 1987. doi: 10.1190/1.1442319.

Fornberg, B. The pseudospectral method: Accurate representation of interfaces in elastic wave calculations. *GEOPHYSICS*, 53(5): 625–637, 1988. doi: 10.1190/1.1442497.

Fryer, G. J. A slowness approach to the reflectivity method of seismogram synthesis. *Geophysical Journal International*, 63(3): 747–758, 1980. doi: 10.1111/j.1365-246X.1980.tb02649.x.

Fuchs, K. The Reflection of Spherical Waves from Transition Zones with Arbitrary Depth-dependent Elastic Moduli and Density. *Journal of Physics of the Earth*, 16 (Special): 27–41, 1968. doi: 10.4294/jpe1952.16.Special_27.

Fuchs, K. and Müller, G. Computation of Synthetic Seismograms with the Reflectivity Method and Comparison with Observations. *Geophysical Journal International*, 23 (4): 417–433, 1971. doi: 10.1111/j.1365-246X.1971.tb01834.x.

Gisolf, A. and Haffinger, P. Post-Critical and Near-Critical Reflections in Seismic AVO Inversion. *Conference Proceedings, 83rd EAGE Annual Conference and Exhibition*, 2022(1): 1–5, 2022. doi: 10.3997/2214-4609.202210617.

Gisolf, D., Haffinger, P. R., and Doulgeris, P. Reservoir-oriented wave-equation-based seismic amplitude variation with offset inversion. *Interpretation*, 5(3): SL43–SL56, 2017. doi: 10.1190/INT-2016-0157.1.

Goovaerts, P. *Geostatistics for natural resources evaluation*. Applied geostatistics series. Oxford University Press, New York, 1997. ISBN 0195115384.

Grana, D. and Rossa, E. D. Probabilistic petrophysical-properties estimation integrating statistical rock physics with seismic inversion. *GEOPHYSICS*, 75(3): O21–O37, 2010. doi: 10.1190/1.3386676.

Grana, D., Mukerji, T., and Doyen, P. *Seismic Reservoir Modeling: Theory, Examples, and Algorithms*. Wiley Blackwell, Hoboken, New Jersey, 2021. ISBN 1119086205.

Grana, D., Azevedo, L., de Figueiredo, L., Connolly, P., and Mukerji, T. Probabilistic inversion of seismic data for reservoir petrophysical characterization: Review and examples. *GEOPHYSICS*, 87(5): M199–M216, 2022. doi: 10.1190/geo2021-0776.1.

Graves, R. W. Simulating seismic wave propagation in 3D elastic media using staggered-grid finite differences. *Bulletin of the Seismological Society of America*, 86(4): 1091–1106, 1996. doi: 10.1785/BSSA0860041091.

Haskell, N. A. The dispersion of surface waves on multilayered media. *Bulletin of the Seismological Society of America*, 43(1): 17–34, 1953. doi: 10.1785/BSSA0430010017.

Kennett, B. L. N. Reflections, rays, and reverberations. *Bulletin of the Seismological Society of America*, 64(6): 1685–1696, 1974. doi: 10.1785/BSSA0640061685.

Kennett, B. L. N. *Seismic wave propagation in stratified media*. ANU E Press, Canberra, new edition, 2009. ISBN 9781921536731.

Knopoff, L. A matrix method for elastic wave problems. *Bulletin of the Seismological Society of America*, 54(1): 431–438, 1964. doi: 10.1785/BSSA0540010431.

Knott, C. G. III. Reflexion and refraction of elastic waves, with seismological applications. *The London, Edinburgh, and Dublin Philosophical Magazine and Journal of Science*, 48(290): 64–97, 1899.

Kolbjørnsen, O., Buland, A., Hauge, R., Røe, P., Ndingwan, A. O., and Aker, E. Bayesian seismic inversion for stratigraphic horizon, lithology, and fluid prediction. *GEOPHYSICS*, 85(3): R207–R221, 2020. doi: 10.1190/geo2019-0170.1.

Kosloff, D. D. and Baysal, E. Forward modeling by a Fourier method. *GEOPHYSICS*, 47(10): 1402–1412, 1982. doi: 10.1190/1.1441288.

Krail, P. M. and Brysk, H. Reflection of spherical seismic waves in elastic layered media. *GEOPHYSICS*, 48(6): 655–664, 1983. doi: 10.1190/1.1441496.

Krebes, E. S. Seismic forward modeling. *CSEG Recorder*, 29(4): 28–39, 2004.

Larsen, A. L., Ulvmoen, M., Omre, H., and Buland, A. Bayesian lithology/fluid prediction and simulation on the basis of a Markov-chain prior model. *GEOPHYSICS*, 71 (5): R69–R78, 2006. doi: 10.1190/1.2245469.

Levander, A. R. Fourth-order finite-difference P-SV seismograms. *GEOPHYSICS*, 53 (11): 1425–1436, 1988. doi: 10.1190/1.1442422.

Li, J., Wang, S., Wang, J., Dong, C., and Yuan, S. Frequency-Dependent Spherical-Wave Reflection in Acoustic Media: Analysis and Inversion. *Pure and Applied Geophysics*, 174(4): 1759–1778, 2017. doi: 10.1007/s00024-017-1489-y.

Liu, H., Li, J., Chen, X., Hou, B., and Chen, L. Amplitude variation with offset inversion using the reflectivity method. *GEOPHYSICS*, 81(4): R185–R195, 2016. doi: 10.1190/GEO2015-0332.1.

Liu, J. S. *Markov Chains and Their Convergence*, pages 245–269. In: Monte Carlo Strategies in Scientific Computing. Springer Series in Statistics. Springer, New York, 2004. ISBN 9780387763712.

Liu, W., Wang, Y.-C., Li, J.-Y., Liu, X.-Q., and Xie, W. Prestack AVA joint inversion of PP and PS waves using the vectorized reflectivity method. *Applied Geophysics*, 15 (3-4): 448–465, 2018a. doi: 10.1007/s11770-018-0695-4.

Liu, X., Guo, Z., and Han, X. Full waveform seismic AVAZ signatures of anisotropic shales by integrated rock physics and the reflectivity method. *Journal of Geophysics and Engineering*, 15(3): 980–994, 2018b. doi: 10.1088/1742-2140/aaa3d3.

Liu, X., Chen, X., Chen, L., and Li, J. Nonlinear prestack inversion using the reflectivity method and quantum particle swarm optimization. *Journal of Seismic Exploration*, 29: 305–326, 2020.

Mallick, S. Model-based inversion of amplitude-variations-with-offset data using a genetic algorithm. *GEOPHYSICS*, 60(4): 939–954, 1995. doi: 10.1190/1.1443860.

Mallick, S. Some practical aspects of prestack waveform inversion using a genetic algorithm: An example from the east Texas Woodbine gas sand. *GEOPHYSICS*, 64(2): 326–336, 1999. doi: 10.1190/1.1444538.

Mallick, S. and Adhikari, S. Amplitude-variation-with-offset and prestack-waveform inversion: A direct comparison using a real data example from the Rock Springs Uplift, Wyoming, USA. *GEOPHYSICS*, 80(2): B45–B59, 2015. doi: 10.1190/geo2014-0233.1.

Mallick, S. and Frazer, L. N. Practical aspects of reflectivity modeling. *GEOPHYSICS*, 52(10): 1355–1364, 1987. doi: 10.1190/1.1442248.

Mittet, R. On the internal interfaces in finite-difference schemes. *GEOPHYSICS*, 82(4): T159–T182, 2017. doi: 10.1190/geo2016-0477.1.

Mittet, R. On the pseudospectral method and spectral accuracy. *GEOPHYSICS*, 86(3): T127–T142, 2021. doi: 10.1190/geo2020-0209.1.

Mosegaard, K. and Tarantola, A. Monte Carlo sampling of solutions to inverse problems. *Journal of Geophysical Research: Solid Earth*, 100(B7): 12431–12447, 1995. doi: 10.1029/94JB03097.

Müller, G. The reflectivity method: a tutorial. *Journal of Geophysics - Zeitschrift für Geophysik*, 58: 153–174, 1985.

Müller, G. Theory of Elastic Waves. Scientific technical report, Deutsches GeoForschungszentrum Potsdam, Potsdam, 2007.

Oliveira, S. A. M., Braga, I. L. S., Lacerda, M. B., Ouverney, G. F., and de Franco, A. W. P. Extending the useful angle range for elastic inversion through the amplitude-versus-angle full-waveform inversion method. *GEOPHYSICS*, 83(3): R213–R226, 2018. doi: 10.1190/geo2017-0168.1.

Ostrander, W. J. Plane-wave reflection coefficients for gas sands at nonnormal angles of incidence. *GEOPHYSICS*, 49(10): 1637–1648, 1984. doi: 10.1190/1.1441571.

Philip, N., Ball, M., Riley, D., and Tillotson, P. Well Ties for Converted Wave Data with an Example from the Clair Field, UKNS. *Conference Proceedings, 80th EAGE Conference and Exhibition*, 2018(1): 1–5, 2018. doi: 10.3997/2214-4609.201801211.

Phinney, R. A., Odom, R. I., and Fryer, G. J. Rapid generation of synthetic seismograms in layered media by vectorization of the algorithm. *Bulletin of the Seismological Society of America*, 77(6): 2218–2226, 1987. doi: 10.1785/BSSA0770062218.

Richards, P. G. and Frasier, C. W. Scattering of elastic waves from depth-dependent inhomogeneities. *GEOPHYSICS*, 41(3): 441–458, 1976. doi: 10.1190/1.1440625.

Robertsson, J. O. A., Blanch, J. O., and Symes, W. W. Viscoelastic finite-difference modeling. *GEOPHYSICS*, 59(9): 1444–1456, 1994. doi: 10.1190/1.1443701.

Ross, C. P. and Kinman, D. L. Nonbright-spot AVO: Two examples. *GEOPHYSICS*, 60 (5): 1398–1408, 1995. doi: 10.1190/1.1443875.

Russell, B. H. *2. Part 2 - The Convolutional Model*, pages 2–1–2–19. Society of Exploration Geophysicists, 1988. doi: 10.1190/1.9781560802303.ch2.

Rutherford, S. R. and Williams, R. H. Amplitude-versus-offset variations in gas sands. *GEOPHYSICS*, 54(6): 680–688, 1989. doi: 10.1190/1.1442696.

Sen, M. K. Seismic, Reflectivity Method. In Gupta, H. K., editor, *Encyclopedia of Solid Earth Geophysics*, Encyclopedia of Earth Sciences Series, pages 1592–1602. Springer International Publishing, Cham, 2021. ISBN 9783030586300.

Sen, M. K. and Pal, A. A reflectivity method for laterally varying media: Homogeneous layers with curved interfaces. *Geophysical Journal International*, 178(2): 792–812, 2009. doi: 10.1111/j.1365-246X.2009.04172.x.

Sen, M. K. and Roy, I. G. Computation of differential seismograms and iteration adaptive regularization in prestack waveform inversion. *GEOPHYSICS*, 68(6): 2026–2039, 2003. doi: 10.1190/1.1635056.

Sen, M. K. and Stoffa, P. L. Nonlinear one-dimensional seismic waveform inversion using simulated annealing. *GEOPHYSICS*, 56(10): 1624–1638, 1991. doi: 10.1190/1.1442973.

Shuey, R. T. A simplification of the Zoeppritz equations. *GEOPHYSICS*, 50(4): 609–614, 1985. doi: 10.1190/1.1441936.

Simm, R. and Bacon, M. *Seismic Amplitude: An Interpreter's Handbook*. Cambridge University Press, Cambridge, 2014. ISBN 1107011507.

Skopintseva, L., Ayzenberg, M., Landrø, M., Nefedkina, T., and Aizenberg, A. M. Long-offset AVO inversion of PP reflections from plane interfaces using effective reflection coefficients. *GEOPHYSICS*, 76(6): C65–C79, 2011. doi: 10.1190/geo2010-0079.1.

Sommerfeld, A. *Über die Ausbreitung der Wellen in der drahtlosen Telegraphie*. Verlag der Königlich Bayerischen Akademie der Wissenschaften, Munich, 1909.

Sommerfeld, A. *Partial differential equations in physics*. Academic press, New York, 1949.

Stephen, R. A. A comparison of finite difference and reflectivity seismograms for marine models. *Geophysical Journal International*, 72(1): 39–57, 1983. doi: 10.1111/j.1365-246X.1983.tb02803.x.

Stoffa, P. L. and Sen, M. K. Nonlinear multiparameter optimization using genetic algorithms: Inversion of plane-wave seismograms. *GEOPHYSICS*, 56(11): 1794–1810, 1991. doi: 10.1190/1.1442992.

Stovas, A., Landrø, M., and Avseth, P. AVO attribute inversion for finely layered reservoirs. *GEOPHYSICS*, 71(3): C25–C36, 2006. doi: 10.1190/1.2197487.

Sun, J., Niu, Z., Innanen, K. A., Li, J., and Trad, D. O. A theory-guided deep-learning formulation and optimization of seismic waveform inversion. *GEOPHYSICS*, 85(2): R87–R99, 2020. doi: 10.1190/geo2019-0138.1.

Sun, J., Innanen, K. A., and Huang, C. Physics-guided deep learning for seismic inversion with hybrid training and uncertainty analysis. *GEOPHYSICS*, 86(3): R303–R317, 2021. doi: 10.1190/geo2020-0312.1.

Symes, W. W. and Vdovina, T. Interface error analysis for numerical wave propagation. *Computational geosciences*, 13(3): 363–371, 2009. doi: 10.1007/s10596-008-9124-8.

Tarantola, A. *Inverse Problem Theory and Methods for Model Parameter Estimation*. Society for Industrial and Applied Mathematics, Philadelphia, 2005. doi: 10.1137/1.9780898717921.

Thomson, W. T. Transmission of Elastic Waves through a Stratified Solid Medium. *Journal of Applied Physics*, 21(2): 89–93, 1950. doi: 10.1063/1.1699629.

Tschache, S., Vinje, V., Lie, J. E., and Iversen, E. Quantifying amplitude-variation-with-offset uncertainties related to calcite-cemented beds using a Monte Carlo simulation. *Interpretation*, 11(2): T315–T329, 2023. doi: 10.1190/int-2022-0084.1.

Tsvankin, I. *Seismic wavefields in layered isotropic media*. Samzidat Press, Colorado School of Mines, Golden, CO, 1995.

Ulvmoen, M. and Omre, H. Improved resolution in Bayesian lithology/fluid inversion from prestack seismic data and well observations: Part 1 — Methodology. *GEOPHYSICS*, 75(2): R21–R35, 2010. doi: 10.1190/1.3294570.

Ulvmoen, M., Omre, H., and Buland, A. Improved resolution in Bayesian lithology/fluid inversion from prestack seismic data and well observations: Part 2 — Real case study. *GEOPHYSICS*, 75(2): B73–B82, 2010. doi: 10.1190/1.3335332.

Ursenbach, C. P., Haase, A. B., and Downton, J. E. Efficient spherical-wave AVO modeling. *The Leading Edge*, 26(12): 1584–1589, 2007. doi: 10.1190/1.2821946.

Ursin, B. and Stovas, A. Reflection and transmission responses of a layered isotropic viscoelastic medium. *GEOPHYSICS*, 67(1): 307–323, 2002. doi: 10.1190/1.1451803.

Vashisth, D. and Mukerji, T. Direct estimation of porosity from seismic data using rock- and wave-physics-informed neural networks. *The Leading Edge*, 41(12): 840–846, 2022. doi: 10.1190/tle41120840.1.

Virieux, J. P-SV wave propagation in heterogeneous media: Velocity-stress finite-difference method. *GEOPHYSICS*, 51(4): 889–901, 1986. doi: 10.1190/1.1442147.

Wapenaar, K., van Wijngaarden, A., van Geloven, W., and van der Leij, T. Apparent AVA effects of fine layering. *GEOPHYSICS*, 64(6): 1939–1948, 1999. doi: 10.1190/1.1444700.

Weyl, H. Ausbreitung elektromagnetischer Wellen über einem ebenen Leiter. *Annalen der Physik*, 365(21): 481–500, 1919.

Yan, B., Wang, S., Ji, Y., Huang, X., and da Silva, N. V. Frequency-dependent spherical-wave reflection coefficient inversion in acoustic media: Theory to practice. *GEOPHYSICS*, 85(4): R425–R435, 2020. doi: 10.1190/geo2019-0643.1.

Yang, D. H., Liu, E., Zhang, Z. J., and Teng, J. Finite-difference modelling in two-dimensional anisotropic media using a flux-corrected transport technique. *Geophysical Journal International*, 148(2): 320–328, 2002. doi: 10.1046/j.0956-540x.2001.01575.x.

Yang, Z. and Lu, J. Thin interbed AVA inversion based on a fast algorithm for reflectivity. *Acta Geophysica*, 68: 1007–1020, 2020. doi: 10.1007/s11600-020-00448-7.

Zhang, Y., Zhang, H., and Zhang, G. A stable TTI reverse time migration and its implementation. *GEOPHYSICS*, 76(3): WA3–WA11, 2011. doi: 10.1190/1.3554411.

Zhao, H., Ursin, B., and Amundsen, L. Frequency-wavenumber elastic inversion of marine seismic data. *GEOPHYSICS*, 59(12): 1868–1881, 1994. doi: 10.1190/1.1443574.

Zheng, Y. Elastic Pre-stack Seismic Inversion in Stratified Media Using Machine Learning. *Conference Proceedings, 81st EAGE Conference and Exhibition 2019*, 2019(1): 1–5, 2019. doi: 10.3997/2214-4609.201901524.

Zhu, X. and McMechan, G. A. Elastic inversion of near- and postcritical reflections using phase variation with angle. *GEOPHYSICS*, 77(4): R149–R159, 2012. doi: 10.1190/geo2011-0230.1.

Zhu, X. and McMechan, G. A. Amplitude and phase versus angle for elastic wide-angle reflections in the τ-p domain. *GEOPHYSICS*, 80(1): N1–N9, 2015. doi: 10.1190/geo2013-0191.1.

Zoeppritz, K. VII b. Über Reflexion und Durchgang seismischer Wellen durch Unstetigkeitsflächen [On the Reflection and Transmission of Seismic Waves at Surfaces of Discontinuity]. *Nachrichten von der Gesellschaft der Wissenschaften zu Göttingen, Mathematisch-Physikalische Klasse*, pages 66–84, 1919.

Červený, V. *Seismic ray theory*. Cambridge University Press, Cambridge, 2001. ISBN 0521366712.

Scientific results

This chapter contains the three research articles that present the scientific results of this thesis. Articles I and II are published online and have undergone peer review. Article III is a manuscript submitted to the journal for peer review. Note that the articles have individual bibliographies and page numbers in the page footers. Articles II and III are written in American English to comply with the journal requirements.

Article I: On the accuracy and spatial sampling of finite-difference modelling in discontinuous models

Saskia Tschache
Vetle Vinje
Einar Iversen

Journal of Applied Geophysics, **206**, 104789 (2022)

DOI: https://doi.org/10.1016/j.jappgeo.2022.104789

Journal of Applied Geophysics 206 (2022) 104789

Contents lists available at ScienceDirect

Journal of Applied Geophysics

journal homepage: www.elsevier.com/locate/jappgeo

On the accuracy and spatial sampling of finite-difference modelling in discontinuous models

Saskia Tschache [a,b,*], Vetle Vinje [a], Einar Iversen [b]

[a] CGG Services (Norway) AS, Lilleakerveien 6A, 0216 Oslo, Norway
[b] Department of Earth Science, University of Bergen, P.O.box 7803, 5020 Bergen, Norway

ARTICLE INFO

Keywords:
Modelling
Seismic
Finite difference
Reflectivity method

ABSTRACT

Finite-difference modelling estimates the wavefield in the subsurface by solving the elastic or acoustic wave equation numerically in a discrete version of the subsurface. The derivatives in the wave equation are approximated by their finite-difference counterparts. In this paper, we investigate the accuracy of acoustic finite-difference modelling as a function of the spatial sampling rate, the frequency, the source-receiver offset and the model parameters and parametrisation. To represent discontinuities in a regular grid, we apply a tapered low-pass wavenumber filter to densely sampled compliance and density models using the Nyquist wavenumber of the desired grid as cut-off wavenumber. A long filter taper improves the finite-difference modelling accuracy but also leads to longer oscillations in the model grids. We use a 2D acoustic central-grid pseudospectral scheme and compare it to analytical solutions of the wave equation and the reflectivity method. We show that previous recommendations for the spatial sampling of four grid points per shortest wavelength in staggered-grid schemes also apply to central-grid schemes. In the case of a single thin layer, the accuracy of finite-difference modelling is dependent on the impedance contrast and the layer thickness. For accurate wide-angle reflection amplitudes of a thin layer with a strong impedance contrast, a denser grid sampling than four grid points per shortest wavelength is required. Furthermore, we demonstrate that the presented wavenumber filtering approach is better suited for the downsampling of regularly sampled compliance and density data derived from well logs than Backus averaging.

1. Introduction

Finite-difference (FD) modelling of seismic wave propagation is the engine of reverse time migration (RTM) and full-waveform inversion (FWI). It is also a valuable tool in the interpretation of seismic images. Because the FD technique finds wide application in the seismic industry, a thorough understanding of its accuracy is important.

Although most applications of seismic FD modelling, such as RTM and classical diving-wave FWI, are performed on models with relatively smoothly varying properties, realistic geological models often contain discontinuities. One example is the seabed that acts as a sharp contrast of acoustic impedance in marine seismic exploration (Yao et al., 2018). Additionally, strong guided waves resulting from the free surface and the fluid-solid boundary reflection can be produced in the water column. For instance, FWI in shallow-water North Sea data is challenged by water bottom reflections and guided waves (Raknes et al., 2015). Other examples of discontinuities encountered in seismic exploration are sediment-salt boundaries (Jones and Davison, 2014), basalt (Gallagher and Dromgoole, 2008), dolerite intrusions (Scheiber-Enslin et al., 2021), or thin layers (Juhlin and Young, 1993). Currently, FWI tends to produce models with high resolution so that the FD modelling is performed on models with more variations (Routh et al., 2017).

In this paper, we study the accuracy of acoustic FD modelling in the presence of discontinuities from a practical viewpoint. The focus is on the following research questions: How should discontinuous models be represented in regular grid models for FD modelling? What grid sampling is needed for an accurate modelling of models with a step, a thin layer or a stack of layers? Does the accuracy vary with offset? What consequences does a too coarse grid sampling have for the amplitude and phase of each frequency component? The answers to these questions give insight into the expected errors of acoustic FD applications and how to mitigate them.

Discontinuous (Aoi and Fujiwara, 1999) and adaptive (Pei et al., 2009) spatial grids and finite-element methods (De Basabe and Sen,

* Corresponding author at: CGG Services (Norway) AS, Lilleakerveien 6A, 0216 Oslo, Norway.
E-mail address: saskia.tschache@uib.no (S. Tschache).

https://doi.org/10.1016/j.jappgeo.2022.104789
Received 22 December 2021; Received in revised form 5 August 2022; Accepted 17 August 2022
Available online 22 August 2022

2007) have been proposed for accurate and efficient modelling of wave propagation in heterogeneous media. However, adaptive grids make the implementation more complex and come with challenges in data management, grid generation and high-performance computing (Zhang and Zhang, 2022). Typically, anisotropic acoustic modelling schemes on central, uniform grids are used in FWI (Warner et al., 2013; Agudo et al., 2018) and RTM (Zhang et al., 2011). We restrict our investigation to acoustic modelling on central, uniform grids without considering anisotropy.

Stephen (1983) and Levander (1988) compared FD modelling to the reflectivity method. They observed high agreement between these two modelling techniques when they were applied to a set of simple models provided suitable numerical parameters were chosen. However, a comparison for finely layered models has not, to our knowledge, been published before.

Gustafsson and Mossberg (2004) and Gustafsson and Wahlund (2004, 2005) analysed the errors associated with models containing discontinuities for time compact staggered-grid schemes of order two and four in both space and time. They showed that the error can be split into grid dispersion error and an interface error caused by a discontinuity. Grid dispersion can be controlled by using higher-order schemes in space (Gustafsson and Wahlund, 2005). Gustafsson and Wahlund (2004) demonstrated that the interface error is of first order even if the schemes they investigated had second- and fourth-order accuracy for smoothly varying model properties. Symes et al. (2008), and Symes and Vdovina (2009) estimated the interface error for a second-order in time and space staggered FD scheme and confirmed that the interface error is of first order. They observed a time shift proportional to the time step and the distance between the interface and the staggered computational grids. To summarize these observations, we can conclude that there are two types of errors, the error caused by grid dispersion and the interface error. While the grid dispersion can be controlled by higher-order schemes, the interface error is of first order in staggered-grid schemes irrespective of their order in space (Symes et al., 2008; Symes and Vdovina, 2009).

To increase accuracy, Moczo et al. (2002) constructed a heterogeneous staggered-grid scheme based on an averaged medium that represents a material discontinuity. Volume harmonic averaging of bulk and shear moduli and arithmetic averaging of density were applied. Lisitsa et al. (2010) and Vishnevsky et al. (2014) showed that second-order accuracy of common staggered-grid schemes could be preserved by applying such a parameter averaging.

Various methods have been proposed to reduce the interface error in central-grid schemes. Cohen and Joly (1996) achieved second-order accuracy for a fourth-order scheme by using an optimal averaging procedure based on plane-wave analysis. Zhang and Le Veque (1997) developed an immersed interface method to achieve second-order accuracy. Another member in the family of interface methods is the explicit simplified interface method proposed by Lombard and Piraux (2004).

Mittet (2017) studied the interface error in acoustic FD modelling using high-order and pseudospectral staggered-grid schemes. He observed that four points per shortest wavelength were required for spatial derivatives to avoid this type of error. In a related study, Mittet (2021a) confirmed that the pseudospectral method could only provide "half-spectral" accuracy in discontinuous media, in the sense that four instead of two points (corresponding to spectral accuracy) per shortest wavelength were required. This type of spatial aliasing error occurred also in high-order finite-difference schemes (Mittet, 2021a). In another study, Mittet (2021b) observed an accuracy limit of the order of 1/10 of the grid sampling interval for the implementation of interfaces by applying a band-limited Heaviside step function to the grids. In this way, even layers as thin as 1/1000 of the grid sampling interval could be represented properly leading to a small spectral amplitude error of $\pm 2.5\%$ and a negligible traveltime error. However, the experiments on thin-layer models were done in 1D and did not investigate the error for non-vertically incident waves. Staggered-grid high-order FD and pseudospectral schemes were used in these experiments.

The majority of studies analysed the interface error associated with staggered-grid schemes. However, many forward-modelling-based applications in the seismic industry use central-grid schemes that do not include special treatment of discontinuities. Central-grid schemes avoid numerical inaccuracies introduced by the interpolation necessary in staggered-grid schemes (Zhang et al., 2011). It is therefore important to investigate the interface error associated with central-grid schemes.

The cited studies restrict the numerical experiments to simple models for which the analytical solution exists. To go further, we use the reflectivity method as a reference to include thin-layer and multi-layer models. In this way, a better understanding of the accuracy of the FD method in more realistic scenarios can be gained.

In contrast to many other studies, we use a broadband wavelet with a uniform amplitude over a large frequency range to study the errors in amplitude and phase for each frequency component. Such an investigation yields more insight than a visual comparison of waveforms or simple error estimates as has been demonstrated by Mittet (2017, 2021a, 2021b). Furthermore, we study the variation of amplitude and phase errors with offset, which is especially relevant in the context of amplitude and phase variation with offset studies.

In this study, we compare the results of acoustic FD modelling to a true reference and investigate the interface error on simple (but not necessarily analytical) cases. In the simple case of a two-layer model, the analytical solution is computed by the Cagniard-de Hoop method (Cagniard, 1939, 1962; De Hoop, 1960). In multi-layer cases, modelling results of the reflectivity method (Fuchs and Müller, 1971; Müller, 1985; Kennett, 2009) serve as a reference. This modelling technique allows full-waveform modelling for horizontally layered media and is accurate for layers of any thickness (Daley and Hron, 1982). In order to save computation time in the FD modelling, the numerical experiments are done in 2D. The findings are still relevant for 3D modelling, since numerical errors persist when the dimensionality of the simulation is increased (Mittet, 2021a).

The paper is structured as follows: In section 2, we introduce the three modelling methods used in this study: the Cagniard-de Hoop method, the reflectivity method and the acoustic FD method. Another important aspect in section 2 is the preparation of grid models for FD modelling. In section 3, we analyse the accuracy of acoustic FD modelling results compared to the true reference for a step model, a thin-layer model and a realistic multi-layer model derived from a well log. Sections 4 and 5 are devoted to a discussion of the results and our conclusions for acoustic FD modelling in practice.

2. Methods

2.1. Cagniard-de Hoop method

The Cagniard-de Hoop method provides an analytical solution for wave propagation in stratified media. Diaz and Ezziani (2010) implemented this method for simple two-layer models and wave propagation in 2D (see Diaz and Ezziani, 2015). We used this code to calculate the analytical solution for the step model (section 3.1). Strictly speaking, the solution is quasi-analytical, since a numerical convolution is involved, but we refer to it as an analytical solution in this article.

2.2. Reflectivity method

We used the reflectivity method (RM) as the modelling technique for thin-layer and multi-layer models. The RM proved to be highly accurate when compared to the analytical solution computed by the Cagniard-de Hoop method for a step model.

Only the relevant principles of the RM are explained here and the reader is referred to Müller (1985) and Kennett (2009) for details. The RM is based on the Sommerfeld integral, which itself can be derived

from the Weyl integral for cylindrical symmetry (Müller, 2007). By the Sommerfeld integral, a spherical wave can be expressed as a superposition of conical waves (Aki and Richards, 2002). The RM was first proposed by Thomson (1950) and later developed by Fuchs and Müller (1971), Kennett (1979), Fryer (1980) and others. Typically expressed as a numerical integration over a part of the real and positive horizontal slowness axis, we found it beneficial to change the integration variable as proposed by Fuchs (1968). A review of the derivation of the relevant equations, which were used to produce the reference solutions for thin-layer and multi-layer modelling examples, is provided in Appendix A.

For the computation of synthetic seismograms in time, first the overall P-P reflectivity R_{PP} is computed by Kennett's method (Kennett, 1974) for a range of frequencies ω and angles of incidence θ to obtain $R_{PP}(\omega,\theta)$. This recursive computation involves the frequency-independent plane-wave reflection and transmission coefficients given by the Zoeppritz equations (Aki and Richards, 2002) as well as phase terms. The frequency dependency is introduced by those phase terms, which are responsible for correct traveltimes and interference of scattering. For a large number of layers, the task of computing $R_{PP}(\omega,\theta)$ is the most demanding in terms of computation time. In the next step, the integral over θ (see Eqs. (A.5) and (A.6)) is computed by numerical integration using the trapezoidal rule. In practice, the integrand should be inspected to find a suitable upper integration limit. Furthermore, a taper at the upper integration limit is recommended (Mallick and Frazer, 1987). After integration, a multiplication with the factors in Eqs. (A.5) and (A.6) including the source excitation function is performed. Finally, the inverse Fourier transform is used to compute the pressure signals in time.

By relationships between the source excitation $F(t)$ of an explosive pressure point or line source and the resulting waveform at any distance given by Müller (2007), it is possible to calculate the source function that gives rise to a desired wavelet at a specific distance from the source. In our modelling examples, we used the tapered Ormsby wavelet shown in Fig. 1. As a broadband wavelet with a flat amplitude spectrum over a wide frequency range, it allows us to analyse the interface error of each frequency component. The tapered Ormsby wavelet has the corner frequencies 6 Hz, 10 Hz, 100 Hz and 120 Hz, a peak time of 0.1 s, a duration of 0.2 s and a maximum amplitude of 1.

2.3. Finite-difference method

The 2D acoustic wave equation for pressure $P(\mathbf{x},t)$ at position $\mathbf{x}=(x,z)$ and time t is given by Eq. (1)

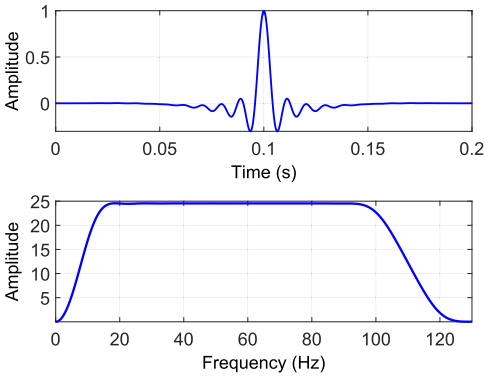

Fig. 1. Tapered Ormsby wavelet (top) used in all numerical experiments and its amplitude spectrum (bottom).

$$\kappa(\mathbf{x})\frac{\partial^2 P(\mathbf{x},t)}{\partial t^2}-\nabla\cdot\left(\frac{1}{\rho(\mathbf{x})}\nabla P(\mathbf{x},t)\right)=S(\mathbf{x},t), \tag{1}$$

where $\kappa(\mathbf{x})$ and $\rho(\mathbf{x})$ denote compliance and density, respectively, and $S(\mathbf{x},t)$ is the source term. The compressional wave velocity α is $\alpha=\sqrt{(\kappa\rho)^{-1}}$.

We used the Fourier method (Fornberg, 1975; Kosloff and Baysal, 1982), also called the pseudospectral method, where the spatial derivatives are computed in the Fourier domain. The spatial derivatives are exact up to the Nyquist wavenumber making a sampling of two grid points per shortest wavelength sufficient in theory.

For the time derivatives, a fourth-order finite-difference approximation (Etgen, 1986) was used. We used small time steps to ensure stability according to the Courant-Friedrichs-Lewy condition, avoid errors in the source injection, and to reduce temporal dispersion. The maximum relative dispersion error was computed to be $<10^{-5}$ so that a correction was not required.

The simulations were performed on a uniform, central grid. Perfectly matched layers as well as model extension were used at all model boundaries to avoid any model boundary reflections interfering with the target reflection signal.

2.4. Tapered low-pass wavenumber filtering of models

To find the optimal representation of a discontinuity in a regular grid, we devised an aliasing-protected algorithm similar to a procedure proposed by Mittet (2017). Starting from ideal models with sharp contrasts, very densely sampled models of P-wave velocity α and density ρ with a sampling interval of $\Delta z'$=0.001 m were created. In the next step, the compliance $\kappa=\rho^{-1}\alpha^{-2}$, the inverse of the bulk modulus, was computed.

The application of a non-windowed low-pass filter to the models would lead to long tails of Gibbs oscillations in the filtered models. These oscillations would be eventually sharply truncated at the model boundaries. Moreover, source and receivers would be located in a weakly varying medium instead of a homogeneous medium. In order to have a better control over the truncation and to understand its effect on the simulation result, we created a tapered low-pass filter. A window of length $N'\Delta z'=N\Delta z$ was defined, where Δz is the desired spatial sampling interval and N', $N>0$ are even numbers. The ideal filter coefficients f_j of a low-pass filter with the Nyquist wavenumber $k_{cut}=\frac{1}{2\Delta z}$ of the desired grid sampling as cut-off wavenumber represent a discrete sinc function, here expressed for $N'+1$ samples as

$$f_j=2k_{cut}\frac{sin\left(j\pi\frac{k_{cut}}{k_{Ny}}\right)}{j\pi\frac{k_{cut}}{k_{Ny}}}, \tag{2}$$

where $k_{Ny}=\frac{1}{2\Delta z'}$, $j=0,\pm1,\pm2,\ldots,\pm\frac{N'}{2}$. The filter coefficients f_j were multiplied by a flat-top window function w_j (D'Antona and Ferrero, 2006)

$$w_j=a_0-a_1cos\frac{2\pi\left(j+\frac{1}{2}N'\right)}{N'}+a_2cos\frac{4\pi\left(j+\frac{1}{2}N'\right)}{N'} -a_3cos\frac{6\pi\left(j+\frac{1}{2}N'\right)}{N'}+a_4cos\frac{8\pi\left(j+\frac{1}{2}N'\right)}{N'}, \tag{3}$$

where $a_0=0.21557895$, $a_1=0.41663158$, $a_2=0.277263158$, $a_3=0.083578947$, $a_4=0.006947368$, to create a tapered low-pass filter. This filter was applied to the densely sampled models V_i, $i=1,\ldots,L$ of compliance or density, respectively,

$$V_i^{filt}=V_i*\left(w_jf_j\right). \tag{4}$$

Finally, the densely sampled filtered model V_i^{filt} was resampled to the desired spatial sampling Δz. The velocity can then be computed from filtered compliance and density models.

Because of the application of a window function to the filter, only $N + 1$ grid points of the resampled model will be affected by a jump in a material property. Fig. 2 illustrates the tapered Gibbs oscillations for two different values of N. The windowing of the low-pass filter implies that the wavenumber filter has a less steep slope, i.e., its transition zone becomes wider as N becomes smaller. Hence, a limited portion of wavenumbers above the Nyquist wavenumber will remain after filtering. To evaluate the error associated with the tapering, we compared FD modelling results from tapered models with different window lengths $N\Delta z$ to modelling results from a non-tapered version. In this test, the source and receivers had a vertical distance of 500 m from the interface as shown in Fig. 3, so that the Gibbs oscillations have decayed almost entirely in the non-tapered version. We used a spatial sampling of $\Delta z = 2$ m. The L^2-norm error E was computed for each trace as

$$E = \frac{\sum_{l=0}^{S-1} (f_N(l\Delta t) - f(l\Delta t))^2}{\sum_{l=0}^{S-1} (f(l\Delta t))^2}, \tag{5}$$

where S is the number of trace samples, Δt the time sampling interval, f_N represents a trace modelled using a tapered model and f represents a trace modelled using a non-tapered model. In Fig. 2, the L^2-norm error averaged over all traces is given as an estimate of the error that is caused by applying the taper. Our numerical experiments showed that choosing N between 10 and 20 appeared to be a good trade-off to keep the Gibbs oscillations short and the taper-induced error low.

Fig. 4 illustrates how the location of the reflector relative to the grid determines where the filtered function is sampled. If the reflector is located at the centre of a grid cell, the maximum roughness of the Gibbs oscillation is captured (cf. Mittet, 2017) with the samples being located at the peaks and troughs of the oscillations as shown in Figs. 2 and 4d. If the reflector is located at the boundary of a grid cell (Fig. 4a), the samples are located close to the inflection points of the oscillations. We will investigate later what impact the interface location with respect to the grid has on the FD modelling result.

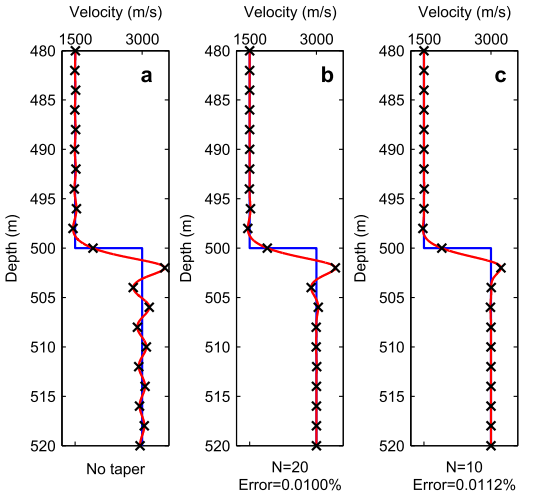

Fig. 2. Illustration of tapered low-pass wavenumber filtering of a 1D velocity step model. The densely sampled model (blue) is low-pass filtered (red) with a non-tapered filter (a) and tapered filters (b, c) so that N + 1 grid points are affected by the step. Black crosses show the grid samples with an interval of Δz = 2.0 m. Note that the Gibbs oscillations are asymmetric because the filtering is done in compliance and density. Average L^2-norm errors of FD modelling results caused by the taper are given below the plots. (For interpretation of the references to colour in this figure legend, the reader is referred to the web version of this article.)

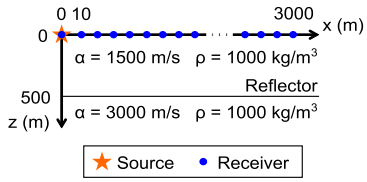

Fig. 3. Source and receiver locations in all modelling experiments. Receiver spacing is 10 m. Layer properties of the step model with constant density are given.

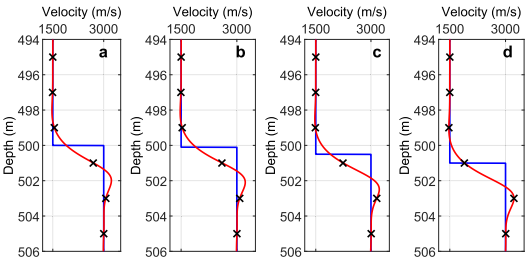

Fig. 4. Tapered low-pass wavenumber filtering of a 1D velocity step model with varying locations of the step relative to the grid. The densely sampled model (blue) is low-pass filtered (red) using a tapered filter of N = 10. Black crosses show the grid samples with an interval of Δz = 2.0 m. The step is located at z = 500.0 m (a), z = 500.1 m (b), z = 500.5 m (c) and z = 501.0 m (d), while the samples at z = 499 m, 501 m, etc. represent the centres of grid cells. (For interpretation of the references to colour in this figure legend, the reader is referred to the web version of this article.)

3. Results

3.1. Step model

In the first example of this study, we analyse the modelling error of the acoustic finite-difference (FD) method compared to the analytical solution for a single flat reflector. This reflector is located around 500 m below the source and receivers, which are all positioned at the same depth as visualised in Fig. 3. It separates two homogeneous half spaces with the properties given in Fig. 3. We applied the algorithm described above to create the grid models for the FD method using a taper of $N = 10$.

The direct wave was removed from all modelling results by subtraction. In this way, we can compare the single reflection event. We computed the normalised amplitude $R(\omega)$ and the phase difference expressed as the traveltime error $\Delta\tau(\omega)$ in milliseconds for a specific pair of source and receiver by Eqs. (6) and (7)

$$R(\omega) = \frac{A_{FD}(\omega)}{A_{Ref}(\omega)}, \tag{6}$$

$$\Delta\tau(\omega) = 1000\frac{\phi_{FD}(\omega) - \phi_{Ref}(\omega)}{\omega}, \tag{7}$$

where $A_{FD}(\omega)$ and $\phi_{FD}(\omega)$ denote the amplitude and phase spectrum of the FD signal and $A_{Ref}(\omega)$ and $\phi_{Ref}(\omega)$ denote the amplitude and phase spectrum of the reference signal, which is the analytical solution in this case.

3.1.1. Varying reflector location with respect to grid

In a first experiment, we analysed the impact of the reflector location with respect to the grid on the FD modelling accuracy. Fig. 5 illustrates various locations of an interface related to a grid cell of $\Delta x = \Delta z = 4.0$ m that is located between $z = 500$ m and $z = 504$ m. We tested four different reflector depths. At $z = 500$ m, the reflector is aligned with the boundary of a grid cell. At $z = 500.66$ m and $z = 501.33$ m, the reflector crosses a grid cell. At $z = 502$ m, the reflector is aligned with the centre of a grid cell. These locations can be expressed as 500 m + $a\Delta z$ depth with $a = 0$, $a = \frac{1}{6}$, $a = \frac{1}{3}$ and $a = \frac{1}{2}$. The amplitude and phase errors for these four scenarios are given in Fig. 6. It turns out that the best accuracy in terms of both amplitude and phase is achieved if the reflector is aligned with a grid cell boundary or, in other words, is located mid-way between two grid nodes. The largest error is observed if the reflector is located at the centre of a grid cell. This case represents the most challenging scenario and will be the focus of subsequent experiments to evaluate the accuracy of FD modelling. From Figs. 2 and 4, we can observe that the grid captures the maximum roughness of the Gibbs oscillations if the interface is located at the centre of a grid cell.

3.1.2. Varying grid sampling

Having identified the least and most challenging location of reflector position relative to the grid, we tested various grid samplings $\Delta x = \Delta z$ in these two locations using a taper size of $N = 10$. The normalised amplitude and traveltime errors are shown in Fig. 7. The Fourier method used in this study requires a spatial sampling of at least two grid points per shortest wavelength. With a maximum frequency of 120 Hz and a minimum velocity of 1500 m/s, the shortest wavelength is 12.5 m long. Theoretically, a grid sampling of 6.0 m should be sufficient to avoid grid dispersion. In the optimal case, where the interface is aligned with the grid cell boundaries, all tested grid samplings gave accurate modelling results. However, in the most challenging scenario, where the interface is aligned with the centres of the grid cells, the accuracy deteriorates with increasing frequency and grid sampling interval. We observe a slight amplitude loss in the high-frequency components for $\Delta x = \Delta z =$ 2.0 m. This effect is even more dramatic for larger spatial sampling intervals. For $\Delta x = \Delta z = 3.0$ m, the amplitudes are reliable up to about 80 Hz. In the case of a grid sampling of 4.0 m, the limit is already reached at about 60 Hz and additionally a small phase error is observed at high frequencies. At long offset, that is, for wide-angle reflections, the amplitude and phase errors vanish for all tested grid sampling intervals. This observation is demonstrated by Fig. 8, which shows the normalised amplitude and traveltime error at 1000 m offset corresponding to an incidence angle of 45°.

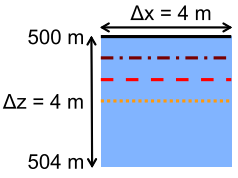

Fig. 5. Finite-difference grid cell (blue) of size $\Delta x = \Delta z = 4.0$ m and various reflector depths indicated by lines: z = 500.0 m (black, solid), z = 500.66 m (dark red, dash-dotted), z = 501.33 m (red, dashed) and z = 502.0 m (orange, dotted). (For interpretation of the references to colour in this figure legend, the reader is referred to the web version of this article.)

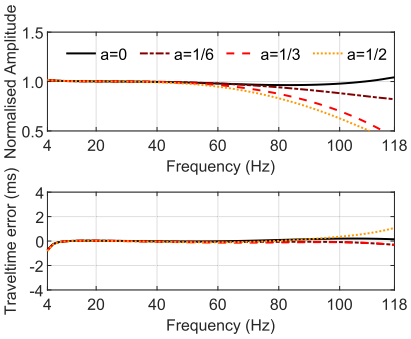

Fig. 6. Normalised amplitude (top) and traveltime error (bottom) of the reflection signal from a reflector at 500 m + $a\Delta z$ depth observed at 100 m offset and modelled by the acoustic FD method using a spatial sampling $\Delta x = \Delta z =$ 4.0 m. The factor a determines the location of the reflector relative to the grid as shown in Fig. 5.

3.1.3. Varying taper size

The aim of our next experiment was to analyse the impact the taper, which is used in the wavenumber filtering of the grid models, has on the accuracy of the FD modelling results. We focus on the most challenging reflector location where it is aligned with the grid cell centres. Instead of using a taper size of $N = 10$, we increase N to 20 and 100, which means that longer tails of Gibbs oscillations away from the interface are included (see Fig. 2). The accuracy of the FD modelling results is shown in Fig. 9. Allowing more grid points to sample the Gibbs oscillations and represent the parameter jump improves the modelling results by shifting the amplitude accuracy limit to higher frequencies for each grid sampling. We observe that the limit is shifted up by about 20 Hz for $N = 20$ compared to the previous example where a taper of size $N = 10$ was used (Fig. 7, right). When using $N = 100$, highly accurate modelling results up to a grid sampling of 3.0 m are achieved. These results suggest that there is a trade-off between shortness of the operator containing the Gibbs oscillations on the one hand and required minimum grid sampling for full-bandwidth accuracy on the other.

3.1.4. Model grid in compliance vs. slowness

Another interesting question concerns which material property the tapered low-pass wavenumber filtering should be applied to in order to create the model grids. For this experiment, we added a jump in density from 1000 kg/m^3 to 2000 kg/m^3 at the same location as the velocity increase from 1500 m/s to 3000 m/s. We applied the tapered filter to compliance $\kappa = \rho^{-1}\alpha^{-2}$ (the inverse of bulk modulus) and density ρ (Fig. 10, left) and to slowness α^{-1} and density ρ (Fig. 10, right). The reflector was aligned with the grid cell centres to create the most challenging scenario. A taper of size $N = 10$ was used. Fig. 10 shows the normalised amplitude and traveltime errors for various grid sampling intervals. While performing the wavenumber filtering in slowness yields amplitude accuracy up to higher frequencies compared to the case of filtering in compliance, increasing phase errors occur with increasing spatial sampling. Already for a grid sampling of 2.0 m, a small traveltime error can be observed, which is present for all frequencies. The results suggest that using compliance results in best accuracy in phase, while using slowness results in best accuracy in amplitude. Note that slowness is not decoupled from density. It was demonstrated by Mittet (2017) that compliance and density are the best choice of material properties on which to perform the filtering operation. This observation is in agreement with the averaging derived by Backus (1962) and Moczo et al. (2002). We therefore decided to do the wavenumber filtering procedure in compliance and density in the subsequent tests.

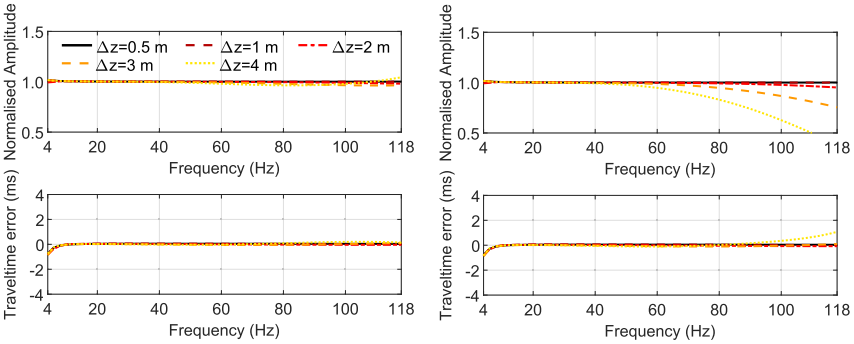

Fig. 7. Normalised amplitude (top) and traveltime error (bottom) of the reflection signal from a single reflector aligned with grid cell boundaries (left) and aligned with grid cell centres (right) observed at 100 m offset and modelled by the acoustic FD method using varying spatial sampling $\Delta x = \Delta z$.

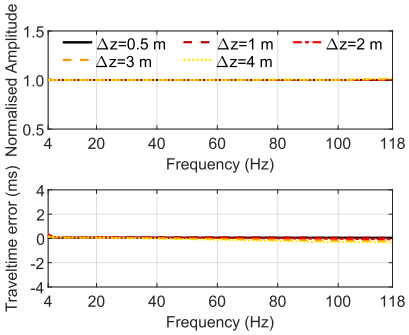

Fig. 8. Normalised amplitude (top) and traveltime error (bottom) of the reflection signal from a single reflector aligned with grid cell centres observed at 1000 m offset and modelled by the acoustic FD method using varying spatial sampling $\Delta x = \Delta z$.

3.2. Thin-layer model

In this experiment, we analyse the accuracy of the FD modelling of a reflection response from a thin, flat layer. The background model has a velocity of 1500 m/s and a density of 1000 kg/m^3. At a depth of about 500 m below the source and receivers (located as shown in Fig. 3), a thin layer with a thickness of 2 m, a velocity of 3000 m/s and a density of 2000 kg/m^3 was inserted. Wavenumber filtering and model sampling were performed in compliance and density using a taper size of $N = 10$. Similar to the previous examples, the direct wave was removed by subtraction prior to analysis of the reflection signal. The reference signal was calculated by the reflectivity method. The normalised amplitude of the FD modelling results and the traveltime error were computed by Eqs. (6) and (7).

With a thickness of 2 m and a velocity of 3000 m/s, the layer can be regarded as thin according to the Widess criterion of a thickness below $\lambda/8$ (Widess, 1973), where λ denotes the wavelength computed by the velocity of the thin layer and the maximum frequency of the wavelet. In such a case and opposite polarity reflectivity, the thin layer acts as an approximate time derivative operator to the wavelet. Fig. 11 illustrates how the initially flat spectrum is now altered such that there is a maximum amplitude at approximately 96 Hz. The figure also demonstrates the high accuracy of amplitudes for a grid sampling of up to 1.0 m and a weak amplitude loss for $\Delta x = \Delta z = 2.0$ m.

We investigated two different cases for the location of the thin layer with respect to the grid. In one case, the layer centre is aligned with a grid cell boundary, in the other case, it is aligned with a grid cell centre. Fig. 12 illustrates the velocity models after wavenumber filtering in compliance and density and the sample locations in these two cases for two different layer thicknesses. If the layer is centred at a grid cell boundary (Fig. 12a, c), the samples do not capture the maximum of the filtered function, but they capture the oscillations away from the layer. If the layer centre is aligned with the centre of a grid cell (Fig. 12b, d), the

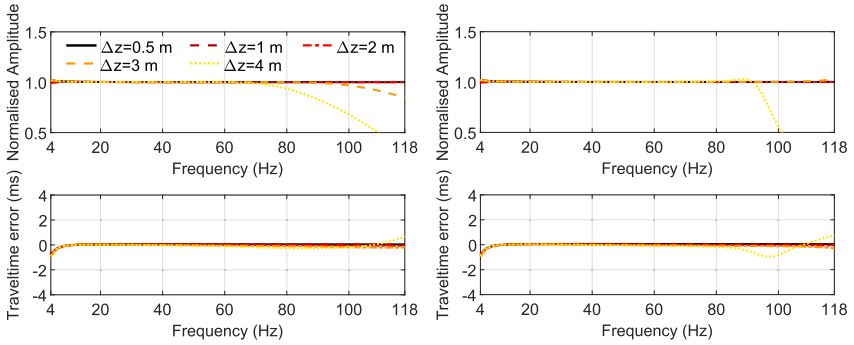

Fig. 9. Normalised amplitude (top) and traveltime error (bottom) of the reflection signal from a single reflector aligned with grid cell centres observed at 100 m offset and modelled by the acoustic FD method using varying spatial sampling $\Delta x = \Delta z$ and using a taper size of $N = 20$ (left) and $N = 100$ (right) to prepare the grids.

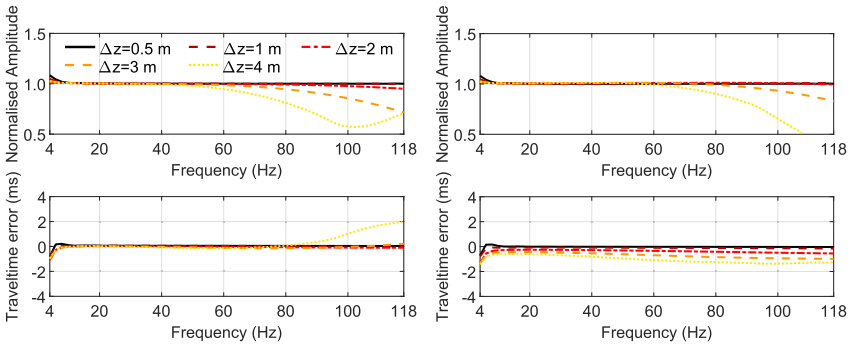

Fig. 10. Normalised amplitude (top) and traveltime error (bottom) of the reflection signal from a single reflector aligned with grid cell centres observed at 100 m offset and modelled by the acoustic FD method using varying spatial sampling $\Delta x = \Delta z$. Left: The discontinuity was filtered in compliance and density. Right: The discontinuity was filtered in slowness and density.

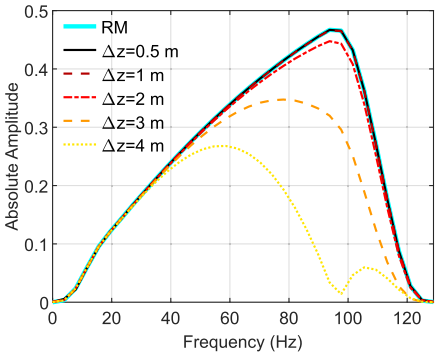

Fig. 11. Absolute amplitude of the reflection signal from a 2 m thick layer centred at grid cell boundaries observed at 100 m offset. The cyan graph shows the reference amplitude spectrum modelled by the reflectivity method (RM). The other graphs display the amplitude spectra of the acoustic FD modelling results using a varying spatial sampling $\Delta x = \Delta z$.

maximum of the filtered function is sampled, but the oscillations away from the layer are only weakly represented in the sample locations. Fig. 13 shows the normalised amplitude and traveltime error for varying spatial sampling if a 2 m thick layer is centred at grid cell boundaries and if its centre is aligned with grid cell centres.

For a thin layer, the FD modelling result is better if the layer centre is aligned with the centre of a grid cell. In this ideal case, full bandwidth accuracy up to $\Delta x = \Delta z = 3.0$ m can be achieved. By analogy with the step model, this is the case in which the oscillations represented by grid samples are the weakest. We have also seen that the maximum of the filtered velocity is captured by a sample, which supports amplitude accuracy. In the most challenging case where the layer is centred at the boundary of a grid cell, good accuracy is observed for the fine grid samplings of 0.5 m and 1.0 m. A weak amplitude loss occurs at the high-frequency components of the signal for $\Delta x = \Delta z = 2.0$ m, but the accuracy is still acceptable. For a larger spatial sampling, significant amplitude errors at high frequencies are seen. The traveltimes are correct except for $\Delta x = \Delta z = 4.0$ m above 95 Hz. It should be noted that the relative amplitude and phase errors seem to be large at low frequencies but are small in absolute values because the amplitudes are very low at such low frequencies (see Fig. 11).

Fig. 14 shows how the normalised amplitude varies with incidence angle for a layer thickness of 2.0 m (solid lines) and 0.2 m (dashed lines). In addition, an example with a weaker contrast in material properties is shown (dash-dotted lines). In this model, the velocity is increased by 200 m/s and the density is increased by 200 kg/m^3 in the 0.2 m thin layer. We used the most challenging scenario where the layer is centred at the grid cell boundaries and plotted the normalised amplitude at 60 Hz.

Unlike the step model, where amplitude and phase errors were reduced with increasing offset, in a thin-layer case, we observe an amplitude loss which increases as the angle of incidence or offset increases. This amplitude error is frequency-independent. It strongly depends on the layer thickness and the contrast in material properties. For all examples, we see that the amplitude error increases with increasing grid sampling. The results suggest that it is challenging to obtain an accurate amplitude variation with offset (AVO) response by FD modelling when very thin layers with strong contrasts in material properties are present. Traveltime errors were negligible in all shown examples.

3.3. Multi-layer model

After evaluating the accuracy of FD modelling for simple discontinuous models, we analysed the accuracy of the FD method in a more realistic model. At the same time, we compared the model downsampling by wavenumber filtering used in this study to the widely used Backus average (Backus, 1962). Based on well log data, we built a multi-layer model consisting of a stack of thin layers with a constant thickness of 0.2 m between 500 m and 600 m depth and extrapolated constant model properties upwards and downwards. We applied the tapered low-pass wavenumber filtering to the compliance and density models of the original sampling $\Delta z' = 0.2$ m to create models of sampling $\Delta z = 3.0$ m and $\Delta z = 4.0$ m using $N = 14$ and $N = 20$, respectively. An alternative approach to downsample densely sampled elastic properties is to use the Backus average. For our case of acoustic, isotropic layers, the equations reduce to an averaging of compliance and an averaging of density. Hence, for $\Delta z = 3.0$ m, 15 layers of thickness 0.2 m contribute to one sample point. For $\Delta z = 4.0$ m, averaging is done over 20 layers. Fig. 15 demonstrates that the resulting downsampled models of wavenumber filtering and Backus average are similar but not identical. It should be noted that the Backus averaging is only valid if Δz is much smaller than the seismic wavelength, that is, maximum 1/10 of the wavelength (Mavko et al., 2009). With the shortest wavelength being 15.5 m in this example, the criterion is not fulfilled for $\Delta z = 3.0$ m or larger.

Source and receiver locations are the same as in previous experiments (see Fig. 3). We used the reflectivity method to produce a reference dataset based on the original densely sampled model with $\Delta z' = 0.2$ m. Fig. 16 shows the FD modelling results for the model versions

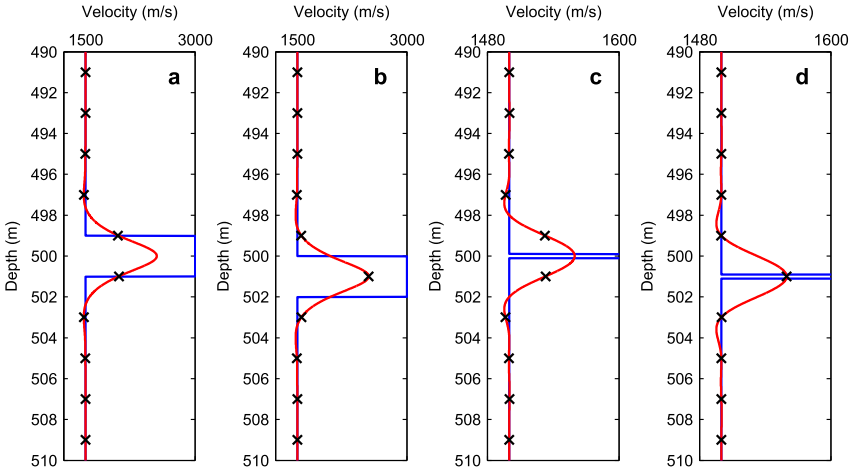

Fig. 12. Tapered low-pass wavenumber filtering of a 1D velocity model of a thin layer with increased velocity of 3000 m/s compared to the background velocity of 1500 m/s for varying locations of the layer centre relative to the grid. The densely sampled model (blue) is low-pass filtered (red) with a tapered filter of taper size $N = 10$. Black crosses show the grid samples with an interval of $\Delta z = 2.0$ m. a: 2 m thick layer centred at a grid cell boundary. b: 2 m thick layer centred at a grid cell centre. c: 0.2 m thick layer centred at a grid cell boundary. d: 0.2 m layer centred at a grid cell centre. The velocity axis is clipped in c and d. (For interpretation of the references to colour in this figure legend, the reader is referred to the web version of this article.)

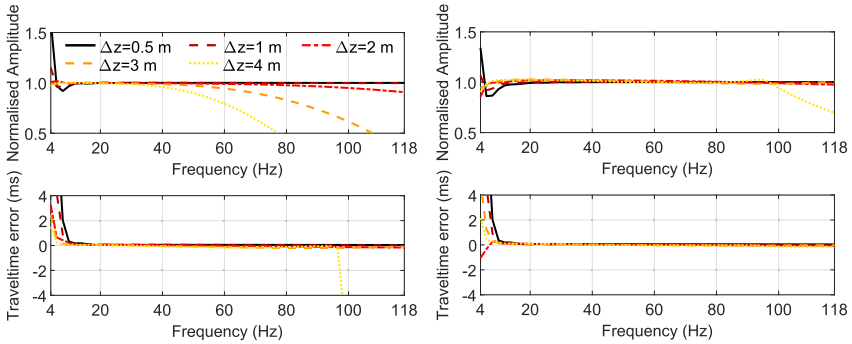

Fig. 13. Normalised amplitude (top) and traveltime error (bottom) of the reflection signal from a thin layer of 2 m thickness with its centre being aligned with grid cell boundaries (left) and grid cell centres (right) observed at 100 m offset and modelled by the acoustic FD method using varying spatial sampling $\Delta x = \Delta z$.

downsampled to $\Delta z = 3.0$ m compared to the reference dataset. The FD modelling results for the models resampled by the tapered low-pass wavenumber filter are in good agreement with the reference dataset and superior to the modelling results for the models produced by Backus averaging although differences are small. As noted before, the Backus average loses validity if the layer thickness becomes too large with respect to the wavelength.

Using a grid sampling interval of 4.0 m, which results in less than four points per shortest wavelength, yields poorer results as can be seen in Fig. 17. At short offsets, the high-frequency components of the FD modelling results based on the models produced by wavenumber filtering are too low in amplitude. At longer offset, the accuracy is satisfactory. As for 3.0 m sampling, the model created by Backus averaging leads to larger errors. The observations support the conclusion from the simple step model that four to five grid points per shortest wavelength are needed for full bandwidth accuracy. Similar to the step model, this requirement can be relaxed at long offsets.

4. Discussion

The reflectivity method can be regarded as a pseudo-analytical solution of the wave equation for layered models and has been used as a reference in other studies dealing with the accuracy of the FD method (Levander, 1988). By using the reflectivity method as a reference, we were able to analyse the offset-dependent accuracy of acoustic FD modelling for finely layered models.

Symes and Vdovina (2009) demonstrated that a discontinuity without special treatment leads to an interface error in finite-difference (FD) modelling. The interface error is purely in phase, thus, creating a time shift. It arises from misalignment between material discontinuities and computational grids. Mittet (2017) proposed the use of a band-limited Heaviside step function to properly implement a parameter jump in the simulation grid. The wavenumber limit is defined by the Nyquist wavenumber of the grid. By following this approach, the location of the interface is arbitrary and the phase error caused by

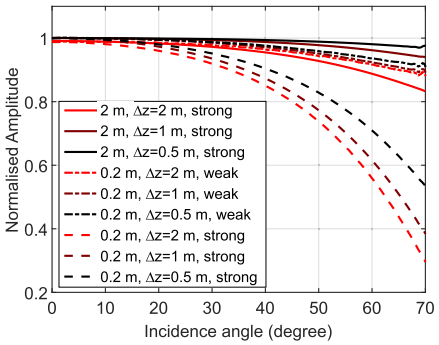

Fig. 14. Amplitude variation with incidence angle of the normalised amplitude at 60 Hz of the reflection signal from a thin layer for a varying spatial sampling $\Delta x = \Delta z$. Solid lines represent the example with a layer thickness of 2.0 m, dashed lines represent the example of a 0.2 m layer thickness and dash-dotted lines correspond to a 0.2 m layer thickness and a weaker contrast in acoustic impedance.

misalignment with the grid (when there is no special treatment of the interface) is corrected. In our study, we used a similar approach to limit the wavenumbers to the Nyquist wavenumber of the simulation grid. In all examples, we have shown that there is no phase error if discontinuities are filtered in compliance and density and the grid sampling is sufficiently fine.

Regarding the accuracy of amplitudes in the step-model example, we make similar observations to the staggered-grid observations of Mittet (2017, 2021a). For the general case, where the location of the discontinuity is not aligned with the grid, Mittet (2017) concluded from experiments using staggered-grid schemes that four to five grid points per shortest wavelength are required. In our experiments using a central-grid scheme, we observed that a spatial sampling of $\Delta x = \Delta z = 3.0$ m, corresponding to four grid points per shortest wavelength, is sufficient for accuracy in amplitude and phase when allowing $N + 1 = 101$ grid points to sample a discontinuity in material properties. Using a grid sampling of 4.0 m, corresponding to only 3 grid points per shortest wavelength, leads to inaccuracies in amplitude and phase for the high-frequency components. The amplitude error is dominant over traveltime error.

Reducing the taper size N shifts the accuracy limit for each grid sampling towards lower frequencies, so that a grid sampling of $\Delta x = \Delta z =$ 3.0 m is no longer sufficient for full bandwidth accuracy when $N = 20$ or $N = 10$. Using a small N makes the accuracy of the FD modelling more dependent on the location of the discontinuity relative to the grid. In agreement with Mittet (2017), we concluded that the most challenging scenario is reached when the interface is aligned with the centre of a grid cell. In such a situation, the grid samples capture the peaks and troughs of the Gibbs oscillations (see Fig. 4). An interesting observation is that the strict requirement concerning the number of grid points per shortest wavelength can be relaxed in the case of a wide-angle reflection from a single interface (see Fig. 8).

We have shown that the wavenumber filtering is ideally done in compliance and density for optimal accuracy. This choice is in agreement with the Backus average that reduces to an averaging in compliance and density for the isotropic, acoustic case and with the averaging proposed by Moczo et al. (2002).

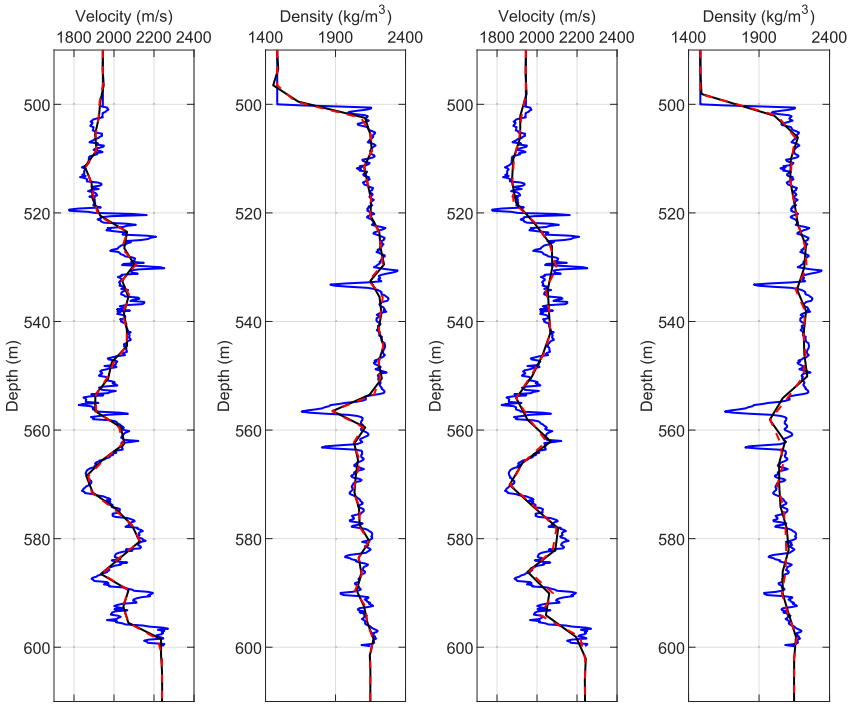

Fig. 15. Resampling of densely sampled models with $\Delta z' = 0.2$ m (blue, solid line) using Backus averaging (red, dashed line) and tapered low-pass wavenumber filtering (black, solid line). From left to right: velocity and density resampling to $\Delta z = 3.0$ m, velocity and density resampling to $\Delta z = 4.0$ m.

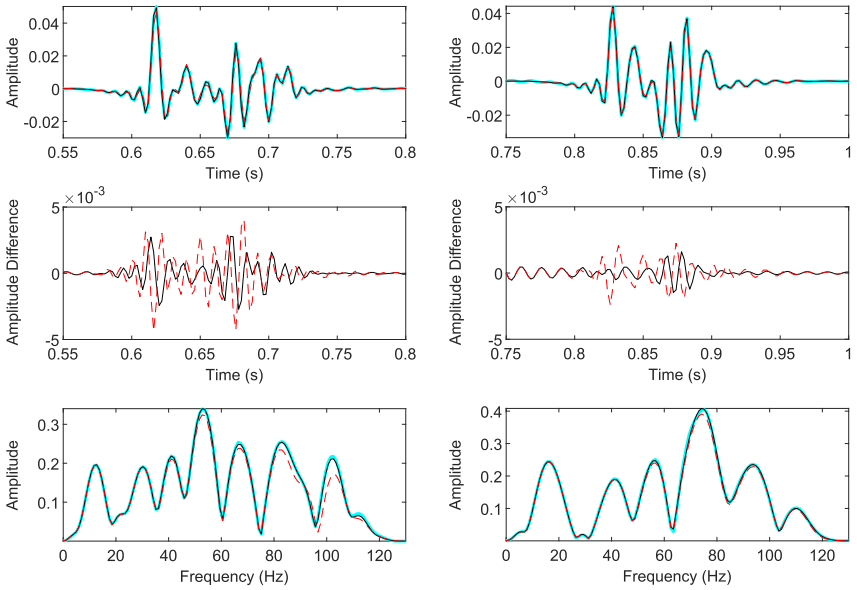

Fig. 16. FD modelling results (top) and corresponding amplitude spectra (bottom) for models downsampled from 0.2 m to 3.0 m spatial sampling by Backus averaging (red, dashed line) and tapered low-pass wavenumber filtering (black, solid line) compared to the reference dataset computed by the reflectivity method for the densely sampled model (cyan, solid line). The reflection response of the 500–600 m interval (Fig. 15) is shown after removal of the direct wave. Centre: difference between FD modelling results and reference. Left: observed at 100 m offset. Right: observed at 1000 m offset. (For interpretation of the references to colour in this figure legend, the reader is referred to the web version of this article.)

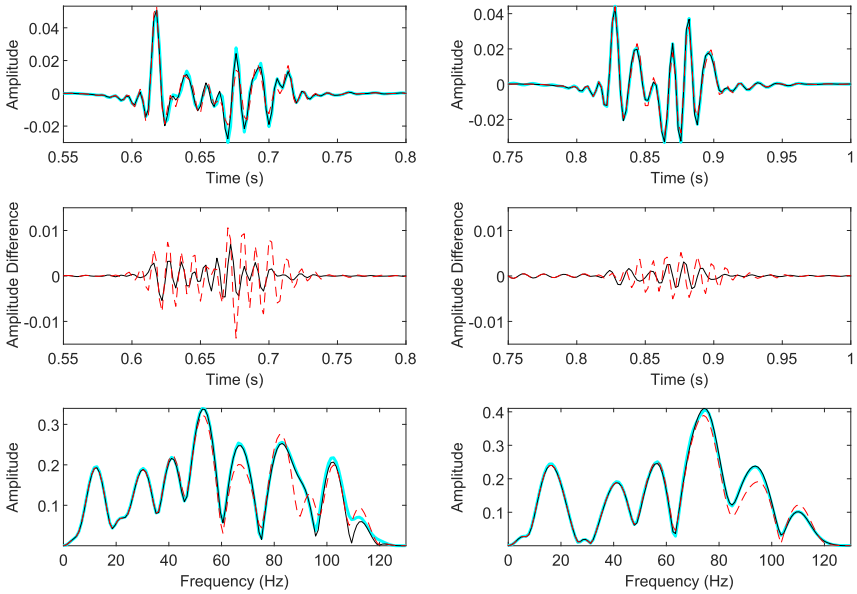

Fig. 17. FD modelling results (top) and corresponding amplitude spectra (bottom) for models downsampled from 0.2 m to 4.0 m spatial sampling by Backus averaging (red, dashed line) and tapered low-pass wavenumber filtering (black, solid line) compared to the reference dataset computed by the reflectivity method for the densely sampled model (cyan, solid line). The reflection response of the 500–600 m interval (Fig. 15) is shown after removal of the direct wave. Centre: difference between FD modelling results and reference. Left: observed at 100 m offset. Right: observed at 1000 m offset. (For interpretation of the references to colour in this figure legend, the reader is referred to the web version of this article.)

A typical application of these findings would be seabed reflections. Mittet (2021b) proposed a method to perform the parameter smoothing locally for continuous horizons. In this way, the seabed can be properly implemented in the simulation grid. With the right choice of taper size N and a grid sampling such that the requirement of four to five grid points per shortest wavelength is fulfilled, the seabed reflection will be accurate in amplitude and phase for the full bandwidth of the signal.

Although the tapered wavenumber filtering approach allows the representation of layers that are thinner than a grid cell, increasing amplitude accuracy problems were observed with increasing incidence angle, decreasing layer thickness and increasing contrast in material properties. Mittet (2021b) observed a slightly increased amplitude error but acceptable accuracy even for layers that were significantly thinner than a grid cell, e.g., an amplitude error of $\pm 2.5\%$ for a layer thickness 1/1000 of the grid step length. However, he did not investigate the offset-dependency of the amplitude error and used a considerably larger number of grid cells to capture the effect of a thin layer in the grid. Our results suggest that thin layers with strong parameter contrasts pose a challenge to the FD method, especially if an accurate amplitude variation with offset (AVO) response is needed. In such a case, decreasing the grid sampling further may help, as Fig. 14 suggests, but may also increase computational costs dramatically. Tests have shown that increasing the taper size N will only slightly reduce the amplitude error. Our work demonstrates that the reflectivity method provides a fast and efficient alternative for modelling the AVO effects of thin layers provided that lateral variations in material properties can be neglected. It should be noted that such extreme opposite polarity contrasts in acoustic impedance rarely occur in realistic subsurface models.

The multi-layer experiment confirmed that minimum four grid points per shortest wavelength are required to obtain an accurate FD modelling result. The model contains moderate contrasts in material properties such that the extreme case tested in the thin-layer example does not need to be considered. We have seen that the tapered low-pass wavenumber filtering in compliance and density yields similar results to averaging of compliance and density following the procedure proposed by Backus, adapted to acoustic and isotropic media. Mittet (2017) has already noted that the low-pass filtering in wavenumber domain resembles an averaging although there is no averaging done in the strict mathematical sense. For the downsampling of densely sampled models to build coarser regular grids for FD modelling, Backus averaging is not accurate enough because the spatial sampling becomes too large with respect to the wavelength. We have shown that the wavenumber filtering approach is a better alternative for such a case. Similar but more advanced downsampling methods were discussed by Capdeville et al. (2010) and Fichtner and Hanasoge (2017).

The experiments have shown that in the presence of discontinuities a finer grid sampling is required than for smooth models. Because our observations agree well with those of Mittet (2017, 2021a), we conclude that the recommendation of four to five grid points per shortest wavelength also apply to non-staggered, central-grid schemes, which are widely used in the seismic industry. This requirement assumes a proper representation of the discontinuity in the grid, limited to the Nyquist wavenumber of the grid. To achieve this, we used an adaptable wavenumber filtering procedure in compliance and density for optimal results. Although this representation of a discontinuity should guarantee invariance of the interface location relative to the grid, we observed that this was not generally the case when a taper was used with the filter. The most challenging situation for a single interface was created when the interface was aligned with the centre of a grid cell. For a single thin layer, the most challenging scenario was created when the layer was centred at a grid cell boundary. We have seen that the choice of taper size N affects amplitude accuracy. Allowing more grid cells to sample the Gibbs oscillations by choosing a larger N, generally improves accuracy. In other words, a coarser spatial sampling is then sufficient to achieve good accuracy for the full bandwidth of the signal. On the other hand, a large N creates models with wider zones of Gibbs oscillations, which might be unwanted. The parameter N allows easy adaption of the filter to specific needs.

The tapered low-pass wavenumber filtering of a finely sampled model as demonstrated here is a valid, effective and adaptable approach for models which vary only in one dimension. However, in the case of 2D or 3D models, this approach becomes computationally costly. Mittet (2021b) proposed a more efficient algorithm for continuous horizons. We agree with Mittet (2021a) that the study results for 2D wave propagation should also be applicable to 3D wave propagation. Similar numerical experiments for elastic, visco-elastic and anisotropic models are beyond the scope of this research, but the methodology and setup of the experiments presented in this paper will be useful for future studies on the topic. Mittet (2017) included an elastic example in his study and found that the same grid step was required as in the acoustic case, but higher wavenumbers had to be included in the grid generation. The consequences of the investigated inaccuracy of FD modelling in discontinuous models for applications such as full-waveform inversion and reverse time migration should be analysed in more detail in separate studies.

5. Conclusion

In this study, we investigated the accuracy of acoustic finite-difference modelling using the Fourier method for spatial derivatives when it is applied to a step model, a thin-layer model and a multi-layer model by comparing it to the analytical solution and modelling by the reflectivity method. The reflectivity method enabled us to extend existing studies that were restricted to simple models, where the analytical solution is available, and allowed us to study the accuracy of finite-difference modelling for finely layered models. We showed that previous recommendations for staggered-grid schemes to apply a low-pass wavenumber filter to densely sampled compliance and density models and to use a spatial sampling of minimum four grid points per shortest wavelength also apply to central-grid schemes. An exception are thin layers with very strong parameter contrasts, where the accuracy of finite-difference modelling deteriorates with increasing incidence angle. A denser spatial sampling is required in such a case. The presented aliasing-protected algorithm to represent discontinuities in a regular grid for finite-difference modelling includes an adaptable taper size. The taper size determines the steepness of the filter slope and the extent to which Gibbs oscillations are present in the model. Including more oscillations increases the accuracy. We have shown that this algorithm is better suited for the downsampling of densely sampled well logs for the finite-difference method than using Backus averaging.

Data availability statement

The data that support the findings of this study are available from the corresponding author upon reasonable request.

Declaration of Competing Interest

The authors declare that they have no known competing financial interests or personal relationships that could have appeared to influence the work reported in this paper.

Data availability

Data will be made available on request.

Acknowledgements

We are grateful to Volodya Hlebnikov, Peng Zhao and Thomas de Jonge for their assistance in running the numerical experiments. Jeremie Messud, Nabil Masmoudi, Rob Schouten and two anonymous reviewers are thanked for helpful comments to improve the manuscript.

Sara Pink-Zerling is thanked for proofreading. We would like to thank the developers of Gar6more2D for making their code available under a free software license. This work was funded by the Research Council of Norway under grant no. 310441.

Appendix A. Computing 2D pressure seismograms by the reflectivity method

To explain the theory of the reflectivity method, we assume a layered medium of plane horizontal, isotropic and homogeneous layers and cylindrical symmetry. We further assume that the first layer is a fluid and that the source and receivers are located in this layer, so that only P-waves are generated and measured. The source is assumed to be located at $z = 0$ and the z-axis is pointing downwards. To make the modelling comparisons easier, the free surface is not included here but could be implemented in general. Under these assumptions, we can express the incident and reflected wavefield from a point pressure source measured by a receiver at offset x and depth z in terms of the compression potentials Φ_{inc} and Φ_{refl} by eqs. (A.1) and (A.2), respectively (cf. Müller, 2007)

$$\Phi_{inc}(x,z,t) = \frac{1}{2\pi}\int_{-\infty}^{+\infty} \widehat{F}(\omega)e^{i\omega t}\int_0^{\infty} \frac{k_x}{ik_{z,1}}J_0(k_x x)e^{-ik_{z,1}|z|}\,dk_x\,d\omega, \tag{A.1}$$

$$\Phi_{refl}(x,z,t) = \frac{1}{2\pi}\int_{-\infty}^{+\infty} \widehat{F}(\omega)e^{i\omega t}\int_0^{\infty} \frac{k_x}{ik_{z,1}}J_0(k_x x)R_{PP}(\omega,k_x)e^{-ik_{z,1}|z|}\,dk_x\,d\omega, \tag{A.2}$$

where $\widehat{F}(\omega)$ denotes the Fourier transform of the source excitation function $F(t)$, t is time, ω is the angular frequency, k_x is the horizontal wavenumber, $k_{z,1}$ is the vertical wavenumber of the first layer, i is the imaginary unit, J_0 denotes the Bessel function of first kind and order zero, and $R_{PP}(\omega,k_x)$ denotes the complex overall P-P reflection coefficient of the stack of layers. It should be noted that $R_{PP}(\omega,k_x)$ is computed by an iterative scheme introduced by Kennett (1974) and contains all single and multiple reflections, mode conversions and evanescent waves. The phase terms in this computation lead to the frequency dependency. The outer integral in Eqs. (A.1) and (A.2) is an inverse Fourier transform back to the time domain while the inner integral is a Sommerfeld integral.

Following the derivations by Tsvankin (1995), the Sommerfeld integrals in Eqs. (A.1) and (A.2) can be expressed in terms of the departing or incidence angle θ instead of the horizontal wavenumber k_x by using the definition of the wavenumber k, the length of the wavenumber vector, $k = \frac{\omega}{\alpha_1}$ with α_1 being the P-wave velocity in the uppermost fluid layer. Using the following identities: $k_x = k\sin\theta$, $k_{z,1} = k\cos\theta$, $k_x dk_x = k^2 \sin\theta\cos\theta d\theta$, we can now exchange the integration variable in Eq. (A.2) and find the Sommerfeld integral for the reflected wavefield to be

$$\widehat{\Phi}_{refl}(x,z,\omega) = -ik\widehat{F}(\omega)\int_{\Gamma} J_0(kxsin\theta)R_{PP}(\omega,\theta)e^{-ik|z|cos\theta}sin\theta\,d\theta. \tag{A.3}$$

The integration path Γ goes along the real axis from 0 to $\frac{\pi}{2}$ and then parallel to the imaginary axis from $\frac{\pi}{2}+i0$ to $\frac{\pi}{2}+i\infty$ in order to include homogeneous and inhomogeneous plane waves.

Using the derivations by Amundsen and Reitan (1994), we can transform Eq. (A.3) so that it gives the corresponding compression potential for a line source and 2D propagation instead of a point source and 3D propagation. This expression is relevant because we want to perform the numerical examples in 2D to save computational cost in the finite-difference modelling. The corresponding Eq. (A.4) for the potential in 2D is

$$\widehat{\Phi}^{2D}_{refl}(x,z,\omega) = -2i\widehat{F}(\omega)\int_{\Gamma} cos(kxsin\theta)R_{PP}(\omega,\theta)e^{-ik|z|cos\theta}\,d\theta. \tag{A.4}$$

Using the relationship between pressure P and compression potential Φ, $\widehat{P}(\omega) = \omega^2\rho_1\widehat{\Phi}(\omega)$ in a fluid with density ρ_1 (Müller, 2007), we can express the full reflection response of a stack of layers in pressure in the case of a line source (2D) and point source (3D) by the following Eqs. (A.5) and (A.6), respectively,

$$\widehat{P}^{2D}_{refl}(x,z,\omega) = -2i\omega^2\rho_1\widehat{F}(\omega)\int_{\Gamma} cos(kxsin\theta)R_{PP}(\omega,\theta)e^{-ik|z|cos\theta}\,d\theta, \tag{A.5}$$

$$\widehat{P}^{3D}_{refl}(x,z,\omega) = -ik\omega^2\rho_1\widehat{F}(\omega)\int_{\Gamma} J_0(kxsin\theta)R_{PP}(\omega,\theta)e^{-ik|z|cos\theta}sin\theta\,d\theta. \tag{A.6}$$

The corresponding horizontal and vertical displacement components, u_x and u_z, can be derived by taking the derivative of the potential Φ with respect to x and z, respectively. The incident wavefield in pressure can be derived from Eq. (A.1) in the same way as shown here for the reflection wavefield.

Typically, the reflectivity method is expressed using a limited integral over the horizontal wavenumber k_x or the horizontal slowness p, with $k_x = \omega p$ (Fryer, 1980; Aki and Richards, 2002). As can be seen from Eq. (A.2), the integrand attains very large values when the vertical wavenumber approaches zero. In general, poles that correspond to surface wave modes lie on the real k_x- or p-axis and hence on the integration path (Aki and Richards, 2002). These poles lead to difficulties in the numerical integration and to artefacts in the resulting synthetic seismograms. A common way to mitigate this difficulty is to introduce attenuation through complex velocities (see for example Müller, 1985). In our study, however, we wanted to compare to results from finite-difference modelling without attenuation and therefore needed a way to compute attenuation-free synthetic data by the reflectivity method. We found that changing the integration variable to the incidence angle θ is beneficial because the resulting integral no longer has a denominator that can approach zero (see Eqs. (A.3) to (A.6)). Several authors have made similar modifications to the traditional Sommerfeld integral (Fuchs, 1968; Fuchs and Müller, 1971). However, the expression of the Sommerfeld integral using the incidence angle is less advantageous if the method needs to be extended to anisotropic media. Note that the reflectivity method is a (visco-)elastic modelling tool, but acoustic modelling can be achieved by assuming very low S-wave velocities in all layers.

References

Agudo, Ò.C., da Silva, N.V., Warner, M., Morgan, J., 2018. Acoustic full-waveform inversion in an elastic world. Geophysics 83 (3), R257–R271. https://doi.org/10.1190/geo2017-0063.1.

Aki, K., Richards, P.G., 2002. Quantitative Seismology, 2nd ed. University Science Books, Sausalito, Calif.

Amundsen, L., Reitan, A., 1994. Transformation from 2-D to 3-D wave propagation for horizontally layered media. Geophysics 59 (12), 1920–1926. https://doi.org/10.1190/1.1443579.

Aoi, S., Fujiwara, H., 1999. 3D finite-difference method using discontinuous grids. Bull. Seismol. Soc. Am. 89 (4), 918–930. https://doi.org/10.1785/BSSA0890040918.

Backus, G.E., 1962. Long-wave elastic anisotropy produced by horizontal layering. J. Geophys. Res. 67 (11), 4427–4440. https://doi.org/10.1029/JZ067i011p04427.

Cagniard, L., 1939. Réflexion et Réfraction des Ondes Séismiques Progressives. Gauthier-Villars, Paris.

Cagniard, L., 1962. Reflection and Refraction of Progressive Seismic Waves. McGraw-Hill, New York.

Capdeville, Y., Guillot, L., Marigo, J.-J., 2010. 1-D non-periodic homogenization for the seismic wave equation. Geophys. J. Int. 181 (2), 897–910. https://doi.org/10.1111/j.1365-246X.2010.04529.x.

Cohen, G., Joly, P., 1996. Construction and analysis of fourth-order finite difference schemes for the acoustic wave equation in nonhomogeneous media. SIAM J. Numer. Anal. 33 (4), 1266–1302. https://doi.org/10.1137/S0036142993246445.

Daley, P.F., Hron, F., 1982. Ray-reflectivity method for SH-Waves in stacks of thin and thick layers. Geophys. J. Int. 69 (2), 527–535. https://doi.org/10.1111/j.1365-246X.1982.tb04963.x.

D'Antona, G., Ferrero, A., 2006. Digital Signal Processing for Measurement Systems: Theory and Applications. Information Technology: Transmission, Processing, and Storage. Springer, New York.

De Basabe, J.D., Sen, M.K., 2007. Grid dispersion and stability criteria of some common finite-element methods for acoustic and elastic wave equations. Geophysics 72 (6), T81–T95. https://doi.org/10.1190/1.2785046.

De Hoop, A.T., 1960. A modification of Cagniard's method for solving seismic pulse problems. Appl. Sci. Res. Sec. B 8 (1), 349–356. https://doi.org/10.1007/BF02920068.

Diaz, J., Ezziani, A., 2010. Analytical solution for waves propagation in heterogeneous acoustic/porous media. Part I: the 2D case. Commun. Comput. Phys. 7 (1), 171–194. https://doi.org/10.4208/cicp.2009.08.148.

Diaz, J., Ezziani, A., 2015. Gar6more2D (version 2.0). http://gar6more2d.gforge.inria.fr.

Etgen, J.T., 1986. High-order finite-difference reverse time migration with the 2-way non-reflecting wave equation. Stanford Explor. Project 133–146.

Fichtner, A., Hanasoge, S.M., 2017. Discrete wave equation upscaling. Geophys. J. Int. 209 (1), 353–357. https://doi.org/10.1093/gji/ggx016.

Fornberg, B., 1975. On a Fourier method for the integration of hyperbolic equations. SIAM J. Numer. Anal. 12 (4), 509–528. https://doi.org/10.1137/0712040.

Fryer, G.J., 1980. A slowness approach to the reflectivity method of seismogram synthesis. Geophys. J. Int. 63 (3), 747–758. https://doi.org/10.1111/j.1365-246X.1980.tb02649.x.

Fuchs, K., 1968. The reflection of spherical waves from transition zones with arbitrary depth-dependent elastic moduli and density. J. Phys. Earth 16 (Special), 27–41. https://doi.org/10.4294/jpe1952.16.Special_27.

Fuchs, K., Müller, G., 1971. Computation of synthetic seismograms with the reflectivity method and comparison with observations. Geophys. J. Int. 23 (4), 417–433. https://doi.org/10.1111/j.1365-246X.1971.tb01834.x.

Gallagher, J.W., Dromgoole, P.W., 2008. Seeing below the basalt – offshore Faroes. J. Article Geophys. Prospect. 56 (1), 33–45. https://doi.org/10.1111/j.1365-2478.2007.00670.x.

Gustafsson, B., Mossberg, E., 2004. Time compact high order difference methods for wave propagation. SIAM J. Sci. Comput. 26 (1), 259–271. https://doi.org/10.1137/030602459.

Gustafsson, B., Wahlund, P., 2004. time compact difference methods for wave propagation in discontinuous media. SIAM J. Sci. Comput. 26 (1), 272–293. https://doi.org/10.1137/S1064827503425900.

Gustafsson, B., Wahlund, P., 2005. time compact high order difference methods for wave propagation, 2D. J. Sci. Comput. 25 (1), 195–211. https://doi.org/10.1007/BF02728988.

Jones, I.F., Davison, I., 2014. Seismic imaging in and around salt bodies. Interpretation 2 (4), SL1–SL20. https://doi.org/10.1190/INT-2014-0033.1.

Juhlin, C., Young, R., 1993. Implications of thin layers for amplitude variation with offset (AVO) studies. Geophysics 58 (8), 1200–1204. https://doi.org/10.1190/1.1443504.

Kennett, B.L.N., 1974. Reflections, rays, and reverberations. Bull. Seismol. Soc. Am. 64 (6), 1685–1696. https://doi.org/10.1785/BSSA0640061685.

Kennett, B.L.N., 1979. Theoretical reflection seismograms for elastic media. Geophys. Prospect. 27 (2), 301–321. https://doi.org/10.1111/j.1365-2478.1979.tb00972.x.

Kennett, B.L.N., 2009. Seismic Wave Propagation in Stratified Media, New ed. ANU E Press, Canberra, ACT, Australia. https://doi.org/10.22459/SWPSM.05.2009.

Kosloff, D.D., Baysal, E., 1982. Forward modeling by a Fourier method. Geophysics 47 (10), 1402–1412. https://doi.org/10.1190/1.1441288.

Levander, A.R., 1988. Fourth-order finite-difference P-SV seismograms. Geophysics 53 (11), 1425–1436. https://doi.org/10.1190/1.1442422.

Lisitsa, V., Podgornova, O., Tcheverda, V., 2010. On the interface error analysis for finite difference wave simulation. Comput. Geosci. 14 (4), 769–778. https://doi.org/10.1007/s10596-010-9187-1.

Lombard, B., Piraux, J., 2004. Numerical treatment of two-dimensional interfaces for acoustic and elastic waves. J. Comput. Phys. 195 (1), 90–116. https://doi.org/10.1016/j.jcp.2003.09.024.

Mallick, S., Frazer, L.N., 1987. Practical aspects of reflectivity modeling. Geophysics 52 (10), 1355–1364. https://doi.org/10.1190/1.1442248.

Mavko, G., Mukerji, T., Dvorkin, J., 2009. The Rock Physics Handbook: Tools for Seismic Analysis of Porous Media. Cambridge University Press, Cambridge.

Mittet, R., 2017. On the internal interfaces in finite-difference schemes. Geophysics 82 (4), T159–T182. https://doi.org/10.1190/geo2016-0477.1.

Mittet, R., 2021a. On the pseudospectral method and spectral accuracy. Geophysics 86 (3), T127–T142. https://doi.org/10.1190/geo2020-0209.1.

Mittet, R., 2021b. Small-scale medium variations with high-order finite-difference and pseudospectral schemes. Geophysics 86 (5), T387–T399. https://doi.org/10.1190/geo2020-0210.1.

Moczo, P., Kristek, J., Vavrycuk, V., Archuleta, R.J., Halada, L., 2002. 3D heterogeneous staggered-grid finite-difference modeling of seismic motion with volume harmonic and arithmetic averaging of elastic moduli and densities. Bull. Seismol. Soc. Am. 92 (8), 3042–3066. https://doi.org/10.1785/0120010167.

Müller, G., 1985. The reflectivity method: a tutorial. J. Geophys. Zeitschrift für Geophysik 58, 153–174.

Müller, G., 2007. Theory of elastic waves, (Scientific Technical Report STR; 07/03), Potsdam : Deutsches GeoForschungsZentrum GFZ, p. 228. https://doi.org/10.2312/GFZ.b103-07037.

Pei, Z.-L., Fu, L.-Y., Yu, G.-X., Zhang, L.-X., 2009. A wavelet-optimized adaptive grid method for finite-difference simulation of wave propagation. Bull. Seismol. Soc. Am. 99 (1), 302–313. https://doi.org/10.1785/0120080002.

Raknes, E.B., Arntsen, B., Weibull, W., 2015. Three-dimensional elastic full waveform inversion using seismic data from the Sleipner area. Geophys. J. Int. 202 (3), 1877–1894. https://doi.org/10.1093/gji/ggv258.

Routh, P., Neelamani, R., Lu, R., Lazaratos, S., Braaksma, H., Hughes, S., Saltzer, R., Stewart, J., Naidu, K., Averill, H., Gottumukkula, V., Homonko, P., Reilly, J., Leslie, D., 2017. Impact of high-resolution FWI in the Western Black Sea: Revealing overburden and reservoir complexity. Lead. Edge 36 (1), 60–66. https://doi.org/10.1190/tle36010060.1.

Scheiber-Enslin, S.E., Manzi, M., Webb, S.J., 2021. Seismic imaging of dolerite sills and volcanic vents in the Central Karoo, South Africa: implications for shale gas potential. S. Afr. J. Geol. 124 (2), 465–480. https://doi.org/10.25131/sajg.124.0043.

Stephen, R.A., 1983. A comparison of finite difference and reflectivity seismograms for marine models. Geophys. J. Int. 72 (1), 39–57. https://doi.org/10.1111/j.1365-246X.1983.tb02803.x.

Symes, W.W., Vdovina, T., 2009. Interface error analysis for numerical wave propagation. Comput. Geosci. 13 (3), 363–371. https://doi.org/10.1007/s10596-008-9124-8.

Symes, W.W., Terentyev, I.S., Vdovina, T.W., 2008. Gridding requirements for accurate finite difference simulation. In: SEG Technical Program Expanded Abstracts, 2008, pp. 2077–2081. https://doi.org/10.1190/1.3059300.

Thomson, W.T., 1950. Transmission of elastic waves through a stratified solid medium. J. Appl. Phys. 21 (2), 89–93. https://doi.org/10.1063/1.1699629.

Tsvankin, Ilya, 1995. Seismic wavefields in layered isotropic media. Samizdat Press, Colorado School of Mines, Golden, CO.

Vishnevsky, D., Lisitsa, V., Tcheverda, V., Reshetova, G., 2014. Numerical study of the interface errors of finite-difference simulations of seismic waves. Geophysics 79 (4), T219–T232. https://doi.org/10.1190/geo2013-0299.1.

Warner, M., Ratcliffe, A., Nangoo, T., Morgan, J., Umpleby, A., Shah, N., Vinje, V., Štekl, I., Guasch, L., Win, C., Conroy, G., Bertrand, A., 2013. Anisotropic 3D full-waveform inversion. Geophysics 78 (2), R59–R80. https://doi.org/10.1190/geo2012-0338.1.

Widess, M.B., 1973. How thin is a thin bed? Geophysics 38 (6), 1176–1180. https://doi.org/10.1190/1.1440403.

Yao, G., da Silva, N.V., Debens, H.A., Wu, D., 2018. Accurate seabed modeling using finite difference methods. Comput. Geosci. 22 (2), 469–484. https://doi.org/10.1007/s10596-017-9705-5.

Zhang, C., Le Veque, R.J., 1997. The immersed interface method for acoustic wave equations with discontinuous coefficients. Wave Motion 25 (3), 237–263. https://doi.org/10.1016/S0165-2125(97)00046-2.

Zhang, C., Zhang, W., 2022. Efficient 2D acoustic wave finite-difference numerical simulation in strongly heterogeneous media using the adaptive mesh refinement technique. Geophysics 87 (1), T29–T42. https://doi.org/10.1190/geo2020-0801.1.

Zhang, Y., Zhang, H., Zhang, G., 2011. A stable TTI reverse time migration and its implementation. Geophysics 76 (3). https://doi.org/10.1190/1.3554411. WA3–WA11.

Article II: Quantifying amplitude-variation-with-offset uncertainties related to calcite-cemented beds using a Monte Carlo simulation

Saskia Tschache
Vetle Vinje
Jan Erik Lie
Einar Iversen

Interpretation, Volume **11**, Issue 2, T315–T329 (2023)

DOI: https://doi.org/10.1190/INT-2022-0084.1

DOI:10.1190/INT-2022-0084.1

Quantifying amplitude-variation-with-offset uncertainties related to calcite-cemented beds using a Monte Carlo simulation

Saskia Tschache[1], Vetle Vinje[2], Jan Erik Lie[3], and Einar Iversen[4]

Abstract

Calcite cement often occurs locally, forming thin layers of calcite-cemented sandstone characterized by high seismic velocities and densities. Because of their strong impedance contrast with the surrounding rock, calcite-cemented intervals produce detectable seismic reflection signals that may interfere with target reflections at the top of a reservoir. In this case, the amplitude-variation-with-offset (AVO) of the effective seismic signature will be altered and may even create a false hydrocarbon indication. From the Monte Carlo simulation, we find that the presence of thin calcite-cemented beds increases the uncertainty of the Bayesian pore-fluid classification based on the AVO attributes intercept and gradient. In the case example of a North Sea turbiditic oil and gas field, the probability of a false-positive hydrocarbon indication increases from 3%–5% to 18%–21% assuming an equal probability of the occurrence of brine, oil, and gas. The results confirm that calcite-cemented beds can create a pitfall in AVO analysis. Realistic estimates of the AVO uncertainty are crucial for the risk assessment of well placement decisions.

Introduction

Tight beds of calcite-cemented sandstone often are observed in shallow marine sandstones (Bjørkum and Walderhaug, 1990a) and have been documented in several North Sea reservoir rocks (Kantorowicz et al., 1987; Saigal and Bjørlykke, 1987; Walderhaug et al., 1989; Walderhaug and Bjørkum, 1992; Gibbons et al., 1993). Thus far, the main interest in studying the distribution, geometry, and geochemical evolution of calcite cementation in sandstones has been motivated by their effect on reservoir quality (Kantorowicz et al., 1987; Saigal and Bjørlykke, 1987; Walderhaug et al., 1989; Bjørkum and Walderhaug, 1990b). As noted by Kantorowicz et al. (1987), laterally continuous beds of calcite-cemented rock act as impermeable barriers to fluid flow and can compartmentalize a reservoir. In some cases, calcite-cemented beds make up a significant proportion of a reservoir and thereby reduce its net-to-gross ratio (Walderhaug and Bjørkum, 1992). From well-log data, it is known that calcite-cemented beds are characterized by a significant increase in acoustic impedance compared with uncemented formation (Bakke, 1996). Although these beds are thin (with a typical thickness of 0.1–1.5 m in our study area) compared with the seismic wavelength, we demonstrate that they can produce a detectable seismic reflection signal owing to their high acoustic impedance contrast to the embedding rock.

In this study, we show that interference with calcite stringer reflections may affect the observed reflection amplitudes of target reflectors, and consequently, it may alter their amplitude-variation-with-offset (AVO) attributes. AVO attributes play an important role in hydrocarbon exploration (Castagna and Backus, 1993; Chopra and Castagna, 2014). There are many examples from the oil and gas industry, such as the Zumba prospect (Avseth et al., 2016) or the Blåveis prospect in the Tertiary turbidites offshore Norway (J. E. Lie, personal communication, 2022), where hard-cemented beds are suspected to create AVO pitfalls. The aim of our study is to quantify the uncertainty of hydrocarbon prediction from the AVO attributes in the presence and absence of calcite-cemented beds. We do not attempt to decrease the uncertainty of the pore-fluid prediction. Nevertheless, the results of our investigation provide useful estimations for risk assessment of well placement decisions in areas where calcite cementation or similar thin high-impedance layers are present. The workflow, that we demonstrate using a case example from the Alvheim Field, can be applied to other regions where well data are available. In frontier areas with

[1]CGG Services (Norway), Oslo, Norway and University of Bergen, Department of Earth Science, Bergen, Norway. E-mail: saskia.tschache@uib.no (corresponding author).
[2]CGG Services (Norway), Oslo, Norway. E-mail: vetle.vinje@cgg.com.
[3]Aker BP, Lysaker, Norway. E-mail: jan.erik.lie@akerbp.com.
[4]University of Bergen, Department of Earth Science, Bergen, Norway. E-mail: einar.iversen@uib.no.

Manuscript received by the Editor 15 August 2022; revised manuscript received 13 December 2022; published ahead of production 23 January 2023; published online 3 April 2023. This paper appears in *Interpretation*, Vol. 11, No. 2 (May 2023); p. T315–T329, 13 FIGS., 2 TABLES.
http://dx.doi.org/10.1190/INT-2022-0084.1.

poor well control, statistical properties derived from analog areas can be used in the workflow.

Unlike quartz cement, calcite cement is not distributed evenly in the rock but accumulated in certain zones, where the pores are filled by calcite cement (Bjørkum and Walderhaug, 1990a). Bjørkum and Walderhaug (1990a) distinguish between three forms of calcite-cemented sandstone as (1) layers of continuously cemented rock, (2) layers where cementation is not continuous and calcite-cemented concretions occur strata bound, and (3) randomly scattered concretions. They present a nucleation and growth model that can explain these three observed types of calcite cementation, which has been discussed further in Walderhaug and Bjørkum (1998). The main source of calcite cement in shallow marine sandstones is carbonate fossils (Bjørkum and Walderhaug, 1990a). Figure 1 shows how a continuously cemented layer forms starting from a layer rich in carbonate fossils. A study on deeply buried marine sandstones showed that calcite cement precipitated at a shallow burial depth and at a depth of approximately 1.5 km and there was no evidence of late cementation (Saigal and Bjørlykke, 1987). The lateral extent of calcite-cemented beds is variable but can reach several kilometers (Bryant et al., 1988; Walderhaug et al., 1989). Their thicknesses typically range from 0.05 to 5 m in the North Sea shallow marine sandstones (Walderhaug et al., 1989; Walderhaug and Bjørkum, 1992; Gibbons et al., 1993). Although in some regions, the vertical spacing of calcite-cemented beds has a cyclic nature (Bryant et al., 1988; Gibbons et al., 1993), in other regions, the spacing appears random (Cavazza and Dahl, 1990; McBride et al., 1995).

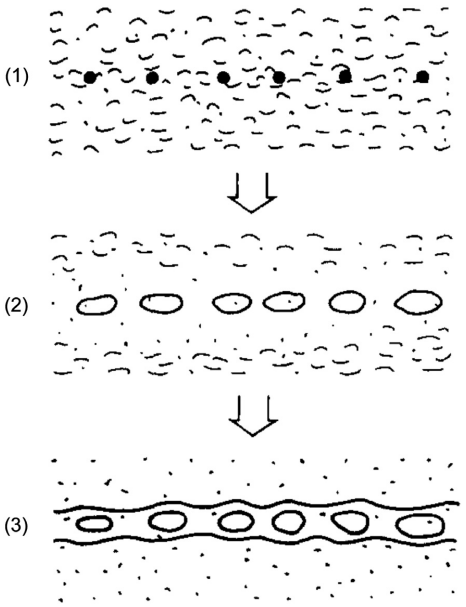

Figure 1. Formation of a calcite-cemented bed starting from a layer rich in carbonate fossils. (1) Nucleation points in the fossil-rich layer grow into (2) calcite concretions that eventually consolidate to (3) a continuously cemented layer. Modified after Bjørkum and Walderhaug (1990a).

The AVO of single thin beds, of which calcite-cemented intervals are an example, has been studied by several authors (Juhlin and Young, 1993; Bakke and Ursin, 1998; Liu and Schmitt, 2003; Pan and Innanen, 2013; Yang et al., 2016).

Gibson (2004, 2005) investigates the effect of internal reservoir stratification on AVO using the propagator matrix method. Stovas et al. (2006) study the effect of the net-to-gross ratio on AVO and propose a simultaneous AVO attribute inversion for the net-to-gross ratio and fluid saturation. These studies considered internal reservoir heterogeneity but did not include any thin layers with high contrasts in acoustic impedance.

Specific research on the impact of calcite-cemented beds on reflection seismic data is extremely sparse. The doctoral thesis by Bakke (1996) on the prediction of calcite cement distribution from seismic data is one of the few published resources. Dutta et al. (2008) analyze the seismic response of calcite cement in sandstones from a rock-physics viewpoint.

In the Bayesian framework, prior probability distributions are updated to posterior probability distributions by means of data (Avseth et al., 2005). Bayesian classification and inversion are frequently applied in seismic reservoir characterization because the nonuniqueness of the solution is honored and uncertainties can be assessed (Grana et al., 2022). Lörtzer and Berkhout (1992) formulate a Bayesian lithologic inversion. Eidsvik et al. (2002) use the Bayesian framework to predict the reservoir properties of a turbidite oil field in the North Sea. Buland and Omre (2003) develop a Bayesian AVO inversion based on the convolutional modeling method and a linearized approximation of the Zoeppritz equations. Larsen et al. (2006) propose a Bayesian prediction of lithology/fluid classes along 1D profiles using the Markov-chain prior models. This approach was extended by Ulvmoen and Omre (2010) and Ulvmoen et al. (2010) to three dimensions by modeling lateral continuity. They achieve high-resolution inversion results identifying thin shale units.

Rimstad et al. (2012) perform lithology and fluid prediction in the Alvheim Field using a hierarchical Bayesian AVO inversion, but the effect of calcite cementation was ignored in the approach. Although quartz cementation was the focus of earlier studies, the presence of tight calcite-cemented beds was merely mentioned. However, these beds were not included as a distinct facies class (Avseth et al., 2009, 2021). Occasionally, unclassified units in lithofacies classification were interpreted as thin units of locally cemented sand (Avseth et al., 2003).

In the first part, we analyze using seismic modeling if a single calcite-cemented bed may produce a reflection signal that, when interfering with a target reflection, can alter the target AVO. Then, we explain, showcase, and

discuss a workflow to quantify the AVO uncertainty caused by calcite-cemented beds.

Effect of a single thin high-impedance layer on target reflection AVO

In the following text, we use the terms "calcite stringers" or "stringers" to refer to thin intervals of calcite-cemented sand. Inspired by a well log from the Alvheim Field that reveals a calcite stringer only a few meters above the top of the reservoir formation, we built a set of three simple models (Figure 2a, 2e, and 2i). Model 1 contains only the caprock (shale) – reservoir (sandstone) interface. The second model contains a 1 m thick calcite stringer embedded in shale. In the third model, a 1 m thick calcite stringer is located 6 m above the caprock-reservoir interface. All models were overlain by a water layer of 120 m, in which the source and receivers are located. The free surface was not included in the modeling. The elastic properties used in the modeling are provided in Table 1. Shale and sandstone properties were read from the logs and S-wave velocity was estimated using an empirical relation. The properties of the calcite-cemented bed were estimated using a Hill mixing (Hill, 1952) of quartz and 35% calcite.

We applied three different seismic modeling methods and compared their results in the depth domain for a

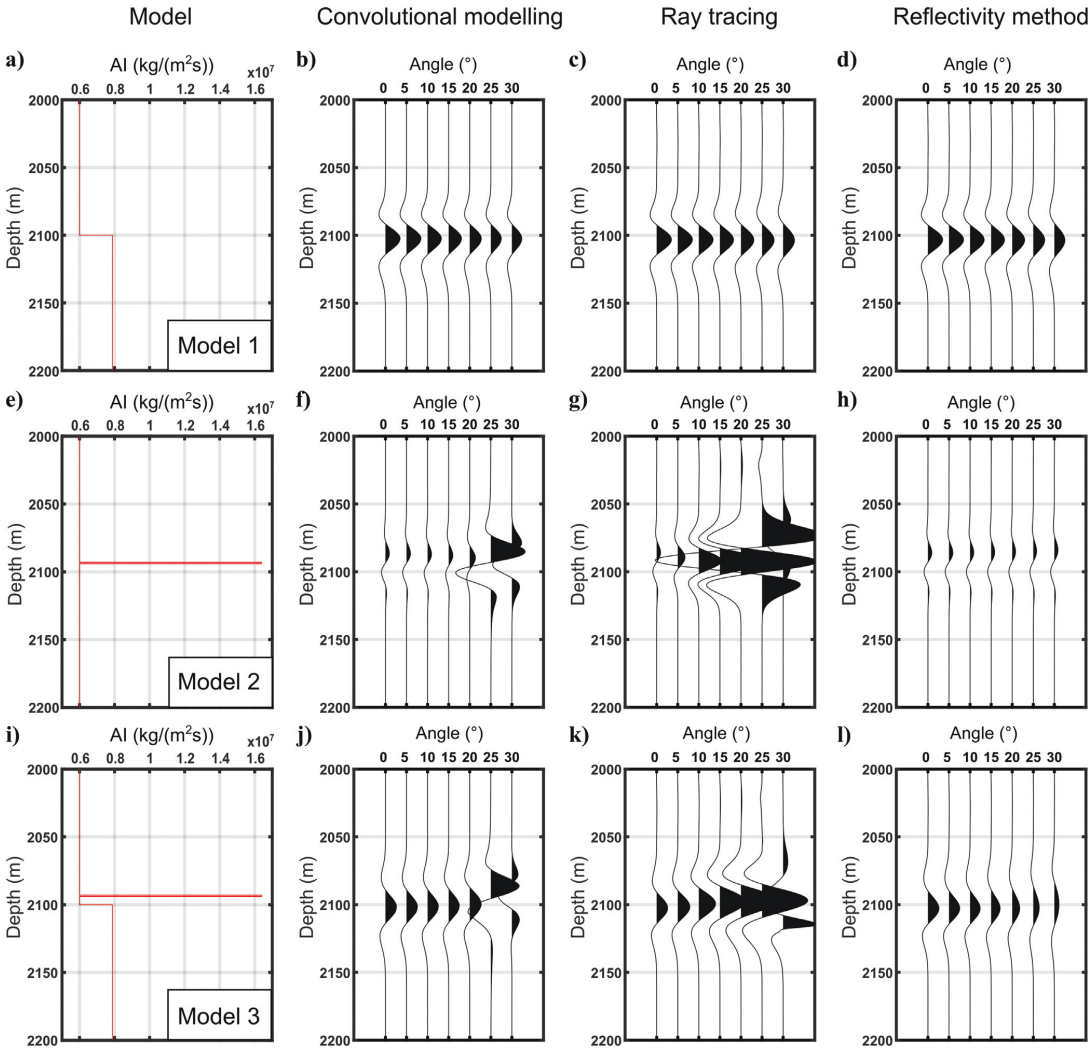

Figure 2. Seismic modeling of (a–l) three simple models. (a, e, and i) The acoustic impedance profiles of the 1D models and (b, f, j), (c, g, k), and (d, h, l) the angle gathers from convolutional modeling, ray tracing, and the reflectivity method, respectively.

DOI:10.1190/INT-2022-0084.1

Ricker wavelet with a dominant frequency of 30 Hz. The first method was the primary-only convolutional modeling method (Russell, 1988) using the Zoeppritz reflection coefficients, which is typically applied in a prestack inversion. Angle-dependent reflectivity series were convolved with the wavelet and the resulting traces were converted to depth. For better comparison, we used the same smoothed velocity model for time-to-depth mapping as for migration of the shot gathers from the other two modeling methods. The second method was a primary-only ray-tracing-based convolutional modeling. In this method, ray tracing provided the traveltimes, incidence angles, and geometric-spreading factors, and the Zoeppritz equations provided reflection coefficients so that synthetic shot gathers could be generated by convolution. The third modeling technique was the reflectivity method (Kennett, 1979; Müller, 1985; Kennett, 2009), which computes the elastic full-wavefield spherical-wave response including all internal multiples and mode conversions. The reflectivity method provides an exact solution of the elastic wave equation for horizontally layered media (Gisolf et al., 2021), even when layers are thin (Tschache et al ., 2022). The synthetic shot gathers produced by ray-tracing-based convolutional modeling and the reflectivity method were migrated by a true-amplitude Kirchhoff prestack depth migration (Hanitzsch et al., 1994) using a smoothed version of the true velocity profile. The migration involved ray tracing in the smoothed velocity model to compute traveltimes and incidence angles, which were used for offset-angle mapping.

The angle gathers for the three models and the three different modeling methods are compared in Figure 2. The convolutional modeling and the ray-tracing-based modeling use the plane-wave P-wave reflection coefficients computed by the Zoeppritz equations directly under the assumption of plane waves. However, it is well known that this assumption breaks down when the incidence angle approaches the critical angle (Červený, 1961; Červený and Ravindra, 1971; Krail and Brysk, 1983; Alhussain et al., 2008; Alulaiw and Gurevich, 2013). This failure can be clearly seen in the modeling results of the convolutional modeling and the ray tracing for models 2 and 3. As a result of the strong impedance contrast at the top of the calcite stringer, the critical angle is already reached at 24° causing a very large Zoeppritz reflection coefficient at this angle and complex reflection coefficients beyond. The ray-tracing modeling results show a noticeable difference to reflectivity-method modeling results at low angles for models 2 and 3. These errors are caused by the strong ray-bending effect of the thin layer leading to different incidence angles at the layer top and bottom. The reflectivity method computes the spherical-wave response as an integral of many plane-wave contributions (Aki and Richards, 2002) and represents the correct solution. It also includes internal multiples and mode conversions that were neglected in the other primary-only modeling techniques. We see that all modeling methods agree well for model 1, where no thin layer with high impedance contrast is present and no critical angle is encountered. It is evident from this experiment that the reflectivity method should be used as a modeling engine rather than convolutional modeling or ray tracing in the presence of thin high-impedance layers.

The response of a single calcite stringer as shown in model 2 in Figure 2 is formed by the interference of the opposite reflections at the top and bottom of the stringer and is approximately a scaled derivative of the wavelet (Widess, 1973). The amplitude is weaker compared with the reflection amplitude of the shale-sandstone interface but is detectable. In the synthetic data for model 3, we see the interference of the calcite stringer reflection with the shale-sandstone reflection. It is noticeable that the amplitude variation with an angle is different from that of model 1.

The maximum amplitudes of the synthetic data modeled by the reflectivity method were picked in a window ±10 m around the top of the reservoir. By least-squares fitting, the AVO attributes intercept $R(0)$ and gradient G were obtained. In Figure 3, the estimated AVO intercept $R(0)$ and gradient G of models 1 and 3 are shown. In both cases, the intercept is positive and the gradient is negative. In this example, the tuning with the calcite stringer response (model 3) causes a shift in the gradient in the negative direction and a subtle decrease of $R(0)$. The simple example proves that the presence

Table 1. Elastic properties of the lithologies used in seismic modeling.

Lithology	V_P (m/s)	V_S (m/s)	Density (kg/m^3)
Shale	2500	1087	2400
Sandstone	3500	1824	2250
Calcite stringer	6136	3838	2670

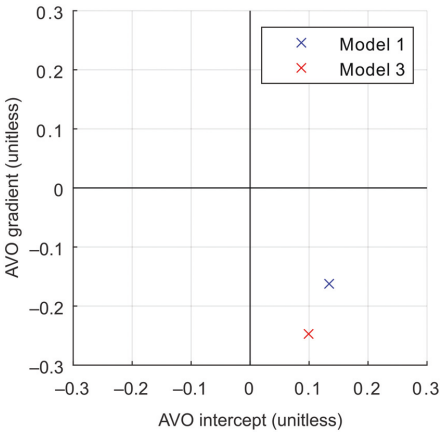

Figure 3. Crossplot of AVO intercept $R(0)$ and gradient G for model 1 (the blue) and model 3 (the red). The tuning with the calcite stringer response in model 3 causes a considerable shift in the $R(0)$-G plane.

of a thin high-impedance layer in the vicinity of the shale-sandstone interface can perturb the target AVO attributes. Typically, in the interpretation of the AVO intercept and gradient, deviations from a background trend are regarded as potential hydrocarbon indicators (Castagna et al., 1998). Other effects creating similar deviations from a background trend can therefore be a serious pitfall in the AVO analysis.

Although the simple example is illustrative, a question arises of how the uncertainty in pore-fluid prediction based on the widely used AVO attributes, intercept and gradient, is affected by the presence of several thin calcite-cemented beds intercalated in the caprock and reservoir zone. To investigate this research question, we developed a workflow and applied it to data from the Alvheim Field.

Methods

The Bayesian classification

For our investigation, we assume that there is a known target horizon, which is the top of a reservoir rock overlain by a caprock. The analysis focuses on the AVO at this target. The target zone is defined to a range ±100 m around the target depth. Furthermore, we assume that well-log data are available in the study area.

In the first step, rock-physics analysis of the well-log data should be performed to define a region-specific set of N classes c_j representing the dominant lithofacies and pore fluids in the target zone. According to the Bayes' theorem, the posterior probability $P(c_j \mid R(0), G)$ of each class c_j given a pair of AVO attributes intercept and gradient $(R(0), G)$ is given by

$$P(c_j \mid R(0), G) = \frac{P(R(0), G \mid c_j)P(c_j)}{P(R(0), G)}, \tag{1}$$

where $P(R(0), G \mid c_j)$ is the conditional probability of an observation $(R(0), G)$ given a class c_j, $P(c_j)$ denotes the prior probability of class c_j, and $P(R(0), G) = \sum_j P(R(0), G \mid c_j)P(c_j)$ is a normalizing divisor. The prior probability $P(c_j)$ describes the probability of the occurrence of class c_j without any knowledge of the AVO attributes. Prior probabilities can be estimated using a priori knowledge from the well data or reservoir models (Avseth et al., 2005). In our approach, the conditional probability density functions (PDFs) $P(R(0), G \mid c_j)$ for each class are computed by a Monte Carlo simulation from trivariate PDFs $P(V_P, V_S, \rho \mid c_j)$ of the elastic properties P-wave velocity V_P, S-wave velocity V_S, and density ρ for each class c_j. These PDFs are computed from the well-log data of (ideally several) wells from the study area as nonparametric probability density distributions by multivariate kernel density estimation using a Gaussian kernel. Alternatively, parametric distributions can be used if they adequately describe the probability density distribution of the data. The trivariate class PDFs take the correlation among V_P, V_S, and ρ into account.

Bayesian classification is done using the Bayes' decision rule,

$$c_k = \underset{j \in \{1, \ldots, N\}}{\operatorname{argmax}} P(R(0), G \mid c_j)P(c_j), \tag{2}$$

assigning the class c_k to a given set of variables $(R(0), G)$ that has the highest posterior probability among all classes $c_j, j = 1, \ldots, N$. In practice, the decision rule can be modified to minimize the expected financial loss of a company (Avseth et al., 2005). By applying the Bayes' decision rule to many examples, it is possible to estimate the probabilities of the correct classification $P(c_k \mid \text{prediction} = c_k)$ and misclassification $P(c_j \mid \text{prediction} = c_k), j \neq k$ for each individual class.

A Monte Carlo simulation for base models

Usually, the two-term approximation of Shuey (1985) is used in a Monte Carlo simulation to estimate $P(R(0), G \mid c_j)$ from $P(V_P, V_S, \rho \mid c_j)$ of the upper and lower medium (Avseth et al., 2001a, 2001b, 2003). As seen from our simple experiment, synthetic seismic data generated by the reflectivity method are needed to investigate the effect of calcite stringers on the AVO attributes. The computational cost of the reflectivity method increases with the number of layers in the model. In the Monte Carlo simulation, we used simplified base models consisting of a 120 m thick water layer, which was followed by a 1980 m thick homogeneous caprock layer and, finally, a homogeneous reservoir layer without a lower boundary. The simplified models represent the average observed water bottom and top reservoir depths of the study area. In our case study, the caprock layer was always of class shale, whereas the reservoir layer could be one out of the three classes brine, oil, and gas corresponding to brine-, oil-, and gas-saturated sandstone, respectively.

For each of the three pore-fluid types, 1000 models were generated and their corresponding AVO attributes, intercept and gradient, were calculated by applying these steps:

1) Draw one shale example (V_P, V_S, ρ) from the shale PDF $P(V_P, V_S, \rho \mid \text{shale})$ and use these properties for the caprock layer.
2) Combine the caprock layer with a reservoir layer using one example drawn from each of the three pore-fluid class PDFs $P(V_P, V_S, \rho \mid \text{brine})$, $P(V_P, V_S, \rho \mid \text{oil})$, and $P(V_P, V_S, \rho \mid \text{gas})$. Note that the three resulting models are not related to each other, except for having the same caprock properties.
3) Generate synthetic seismic shot gathers by the reflectivity method using a Ricker wavelet with a peak frequency of 30 Hz.
4) Apply true-amplitude Kirchhoff prestack depth migration (Hanitzsch et al., 1994) to each offset class using ray tracing in a smoothed version of the true velocity model. The smoothing was done in slowness using a 100 m long Gaussian kernel.

DOI:10.1190/INT-2022-0084.1

5) Extract seismic amplitudes at the target depth.
6) Fit a linear function $R(\theta) = R(0) + G\sin^2\theta$ by the least-squares method to obtain AVO intercept $R(0)$ and AVO gradient G.

Step 3 simulates the true wave propagation in the layered elastic earth creating realistic shot gathers. The modeling was done with an absorbing water surface so that we simulated a seismic processing sequence that perfectly removed the surface-generated multiples.

A Monte Carlo simulation for stringer models

For investigating the impact of the presence of calcite stringers on the resulting PDFs $P(R(0), G \mid c_j)$, many random models containing realistic distributions of several calcite stringers were required. From interpreted well data, we estimated the approximate PDF $P(n)$ for the number n of calcite stringers per well in the target zone (±100 m around the defined target). Using well logs and core images, the PDFs $P(d)$ of the calcite stringer thickness d and $P(z)$ of the vertical location z of the stringer top relative to the target depth were estimated. Furthermore, a PDF $P(V_P, V_S, \rho \mid \text{stringer})$ of the elastic properties of the calcite stringers was needed. It could be either estimated from available data or by using rock-physics mixing models. For simplification, we assumed that each calcite stringer could be approximated by a thin layer with homogeneous elastic properties.

The workflow of a Monte Carlo simulation for the stringer models comprised the following steps, which were performed iterating through the base model data set for $i = 1, \ldots, 1000$:

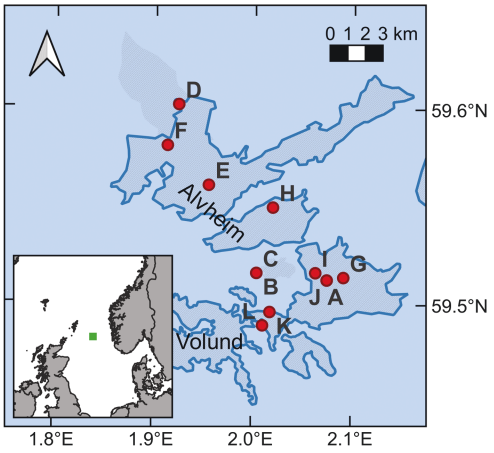

Figure 4. Location of the Alvheim Field in the North Sea (the green square in the small inset map) and map of the Alvheim Field showing the wells A–L (the red markers) included in this case study. Note that some wells share the same surface location because of sidetracks. Discoveries (the shaded areas) and field outlines (the dark blue outlines) are shown for orientation.

1) Draw the calcite stringer properties from the corresponding PDFs: at first the number of stringers n from $P(n)$, then thickness d, vertical location z, and elastic properties P-wave velocity V_P, S-wave velocity V_S, and density ρ for each individual stringer.
2) Insert this specific set of n calcite stringers into the three base models of iteration i.

Then, steps 3–6 of the aforementioned workflow for the base models were applied.

Application of workflow to the Alvheim Field

Definition and characterization of lithology/fluid classes

The Alvheim Field is an oil and gas field on the Norwegian continental shelf (Figure 4). The main reservoirs are turbidite deposits of the Paleocene age of the Heimdal Formation at depths of approximately 2100 m (Norwegian Petroleum Directorate, n.d.). For our case study, we defined the top of the Heimdal Formation as our target. The caprock is predominantly shale belonging to the Lista Formation. The well data revealed that the shale is sometimes interrupted by thin hard beds that were interpreted as calcite-cemented sandstone. Such intercalated sand layers are typical for turbidite deposits (Rimstad et al., 2012).

The Heimdal Formation consists primarily of sands. Quartz cementation of the sand initiates at a temperature of approximately 70°C, which corresponds to a burial depth of approximately 2000 m in the North Sea area (Bjørlykke, 1998). Therefore, unconsolidated sands and quartz-cemented sands are expected around the target depth, as also confirmed by rock-physics analysis (Avseth et al., 2021). Quartz cementation stiffens the rock frame, reduces the fluid sensitivity of the rock, and changes the rock's AVO signature (Avseth et al., 2008, 2009).

Calcite stringers were interpreted in all well logs that were included in our workflow. An example of a calcite-cemented interval of approximately 1.1 m thickness is shown in the core image in Figure 5. Figure 6 shows exemplarily well logs from well E in the target zone with the calcite stringer locations indicated by the arrows. Note that several calcite stringers in the caprock and the reservoir zone were interpreted. In a rock-physics analysis of the Alvheim Field, such calcite-cemented stringers stood out above the stiff sand bound (Avseth et al., 2021).

We defined five different lithology/fluid classes for this case study: shale for the caprock; brine, oil, and gas corresponding to brine-, oil-, and gas-saturated sandstone in the reservoir unit; and stringer corresponding to calcite-cemented sandstone beds that may traverse the caprock and the reservoir unit. Except for the stringer class, the same lithology/fluid classes were used in the study by Rimstad et al. (2012) on the Alvheim area.

DOI:10.1190/INT-2022-0084.1

Estimation of lithology/fluid class PDFs

We used the well logs of nine wells (D–L in Figure 4), which penetrated the target zone, to extract data samples of the P-wave velocity V_P, S-wave velocity V_S, and density ρ for the classes shale, brine, oil, and gas. The aim was to estimate PDFs that represent the variability of the rock physical parameters in the Alvheim Field realistically. For each well, we used only the data in the target zone ±100 m around the target (top of the Heimdal Formation). We excluded the calcite stringer and heterolithic zones. We will discuss subsequently how the elastic properties of the calcite stringers were obtained.

Five of the wells did not have any S-wave information. For the estimation of V_S from V_P using locally derived empirical relations, we applied a procedure proposed by de Sousa et al. (2019), which has proven successful for other North Sea wells. The method included the Gassmann fluid substitution (Gassmann, 1951) for hydrocarbon zones. The comparison of the estimated and measured V_S (where possible) confirmed that the V_S estimation is robust.

Figure 7 shows the well-log-derived rock-physical properties for the lithology/fluid classes in a crossplot of V_P/V_S and acoustic impedance ρV_P. In the crossplot, the data points of all four classes cluster nicely. Shale samples are well separated from the sandstone data points. Brine data points are separated from hydrocarbon data points and the hydrocarbon trend toward lower acoustic impedance and lower V_P/V_S is visible. The oil and gas data points are not fully separated.

For each of the four classes, shale, brine, oil, and gas, we computed a nonparametric probability density distribution by multivariate kernel density estimation using the Gaussian kernels. The kernel bandwidths were computed by the Silverman's rule of thumb (Silverman, 1986). The resulting trivariate class-conditional probability density distributions $P(V_P, V_S, \rho \mid c_j)$ are visualized as 3D contours of equal probability density in Figure 8.

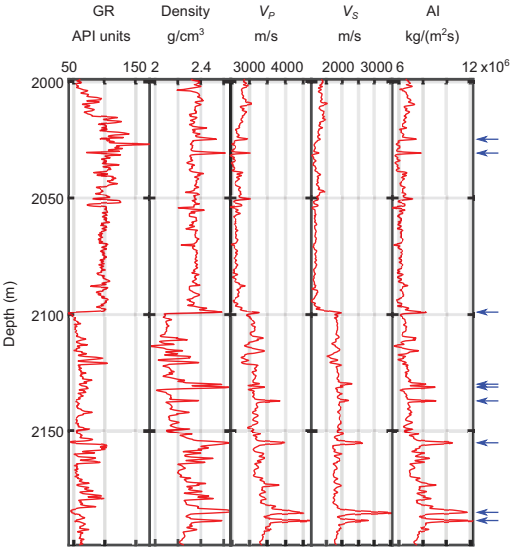

Figure 6. Gamma ray, density, P-wave velocity, S-wave velocity, and acoustic impedance logs in the target zone of well E. Interpreted calcite stringer locations are indicated by the blue arrows. The top of the Heimdal Formation is at a depth of 2099 m. Log data courtesy of Diskos.

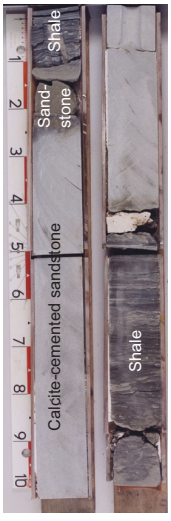

Figure 5. Core image from one of the wells included in the case study showing a 1.1 m interval of calcite-cemented sandstone. Image (without labels) courtesy of Norwegian Petroleum Directorate.

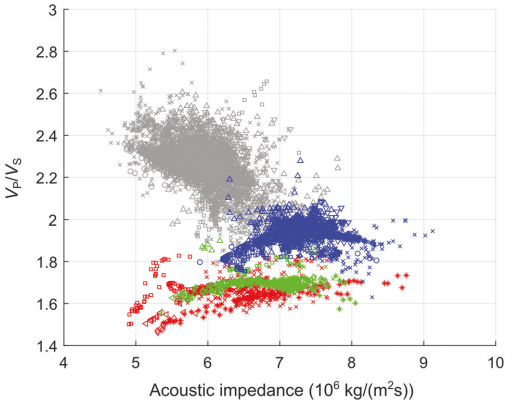

Figure 7. Rock-physics properties of the four classes shale (the gray), brine (the blue), oil (the green), and gas (the red) derived from well logs of nine wells. Different markers represent different wells.

The number of interpreted calcite stringers n counted in the target zone ranged from 5 to 11. Although the data set was very sparse with only nine wells, we fitted a Poisson distribution for $P(n)$ as shown in Figure 9a. In Figure 9b, the statistics of the vertical location z of the individual calcite stringers relative to the reservoir top are shown. Interestingly, there is no preferred location and there are almost as many stringers in the shale (negative relative locations) as in the sandstone intervals (positive relative locations). Therefore, we assumed a uniform distribution of $P(z)$.

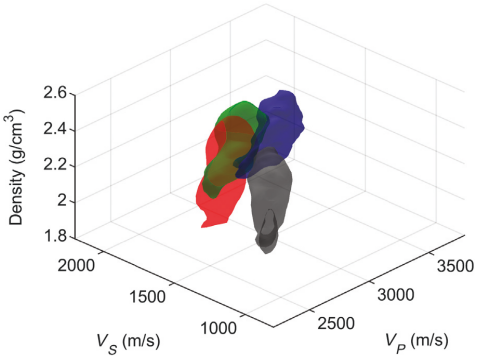

Figure 8. Surfaces of the equal probability density of 10^{-5} for the classes shale (the gray), brine (the blue), oil (the green), and gas (the red).

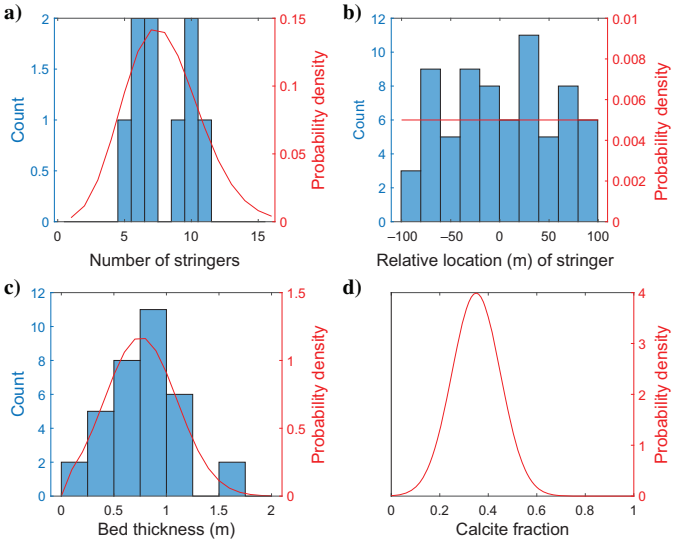

Figure 9. Statistics of the observed calcite stringer properties (the blue) and fitted or assumed probability density distributions (the red). (a) Number of stringers in the target zone per well (sparse data set), (b) vertical location of individual stringer top relative to the target depth, (c) stringer thickness, and (d) assumed probability density distribution of the calcite fraction (no data available).

The analysis of well-log data at the interpreted calcite stringer locations revealed a wide range in V_P, V_S, and density values. We concluded that the calcite stringers were so thin that the log measurements were severely affected by averaging effects of the specific tools and shoulder-bed effects. These effects also hampered the measurement of calcite stringer bed thickness. Therefore, we used core images to measure the individual bed thicknesses. Comparison with the microresistivity logs revealed that the resolution of these measurements was high enough to obtain a good estimate of the bed thickness. Where no core images were available, we used the microresistivity logs (when available) to estimate bed thicknesses. The resulting distribution of the observed bed thicknesses d shown in Figure 9c agreed well with other studies on calcite-cemented intervals in the North Sea sands (Walderhaug et al., 1989; Walderhaug and Bjørkum, 1992). We fitted a truncated normal distribution to the bed thickness data to obtain $P(d)$.

We looked in the literature for typical compositions of the calcite-cemented North Sea sandstones. The main components are typically quartz and calcite minerals, and the porosity is usually low (Saigal and Bjørlykke, 1987; Walderhaug and Bjørkum, 1992). As an approximation, we assumed that the calcite stringers are composed of quartz and calcite minerals without any porosity. We further assumed that the calcite fraction probability density is normally distributed with a maximum of 35% (see Figure 9d). Using the Hill mixing law (Hill, 1952), we computed the resulting P-wave velocity V_P, S-wave velocity V_S, and density ρ depending on the calcite fraction. For a calcite fraction of 35%, we obtained values of V_P = 6136 m/s, V_S = 3838 m/s, and ρ = 2.671 g/cm^3. These values were in reasonably good agreement with the assumptions made by Bakke (1996) of V_P = 6520 m/s and ρ = 2.68 g/cm^3 for calcite-cemented intervals. By using a normally distributed calcite fraction, we could account for the variability in calcite content observed in studies (Saigal and Bjørlykke, 1987) and the related variability in elastic properties.

Results of Monte Carlo simulations

Figure 10 shows the PDFs resulting from the Monte Carlo simulations of base and stringer models after following the workflow described in the "Methods" section. In the case of the base models, there is a good separation between the brine and the hydrocarbon classes in the $R(0)$-G domain with only limited overlap of the PDFs. The PDF of class gas has its peak at a lower intercept amplitude compared with the maximum of the PDF of oil. The overlap of

the PDFs of gas and oil is significant, suggesting that the discrimination between the presence of oil and gas by the AVO intercept and gradient alone is challenging in the Alvheim Field.

The PDFs of the stringer models are different from those of the base models, and all align along the same linear trend. There is considerable overlap between the three class-conditional PDFs, indicating that the pore-fluid discrimination by the AVO intercept and gradient is reduced by the presence of calcite stringers. Especially the brine PDF moved toward the hydrocarbon PDFs. A single calcite stringer produces a peak-trough-shaped seismic signal as seen in the simple modeling example. Depending on its location above or below the top reservoir, the AVO intercept (zero-offset amplitude) measured at the reservoir top can be decreased or increased because of the interference. The AVO gradient is affected by offset-dependent tuning and shows more variability than the AVO intercept.

Results of the Bayesian classification

Using the class-conditional PDFs $P(R(0), G \mid c_j)$, the Bayesian confusion matrices can be estimated showing the probabilities of the correct and incorrect classification for each class. These values are important for evaluating the uncertainty of the Bayesian classification. Figure 11 shows the confusion matrices of the Bayesian classifiers derived from the base and stringer models assuming equal prior probabilities $P(\text{brine}) = P(\text{oil}) = P(\text{gas}) = 1/3$. Each matrix element in row i and column j represents the conditional probability $P_{ij} = P(\text{true class} = c_i \mid \text{predicted class} = c_j)$. The diagonal elements contain the probabilities of correct classification, whereas the off-diagonal elements contain misclassification probabilities. The column-wise sum of probabilities is one.

Comparing the two confusion matrices, we see that all probabilities of correct classification are decreased and almost all misclassification probabilities are increased for the stringer models compared with the base models. In general, we can state that the presence of the calcite stringers significantly increases the uncertainty of pore-fluid prediction from the AVO attributes intercept and gradient. More specifically, the probability of correctly classifying brine has decreased from 87% to 55%, and the probabilities to predict a hydrocarbon, when there is brine (false positive), and predicting brine, when there is a hydrocarbon (false negative), are clearly increased. The confusion between oil and gas is similar for base and stringer model classifiers.

Bootstrap analysis

Bootstrapping (Efron, 1979) is a common statistical tool to measure the accuracy of statistical estimates. It gives us an estimate of the variability and, thus, the certainty of the classification probabilities. We used 100 bootstrap data sets created by drawing from the original data set with replacement.

Figure 12 shows the resulting histograms for the probabilities of correct classification $P(c_i \mid c_i)$ for the base and stringer model classifiers. The histograms indicate that the variability in the probabilities is small. For both classifiers, the probability of correctly predicting oil is the lowest. This is not surprising because the PDF of oil is in between brine and gas causing more misclassification when there is oil. All of the probabilities of correct classification are reduced for the stringer model classifier compared with the base model classifier with the most dramatic decrease observed for brine.

The probability of a false-positive hydrocarbon indication $P(\text{brine} \mid \text{oil} \cup \text{gas})$, i.e., a dry hole, was estimated by summing the error probabilities $P(\text{brine} \mid \text{oil})$ and $P(\text{brine} \mid \text{gas})$ (Avseth et al., 2005). In Figure 13, the Bootstrap histograms of false-positive probabilities

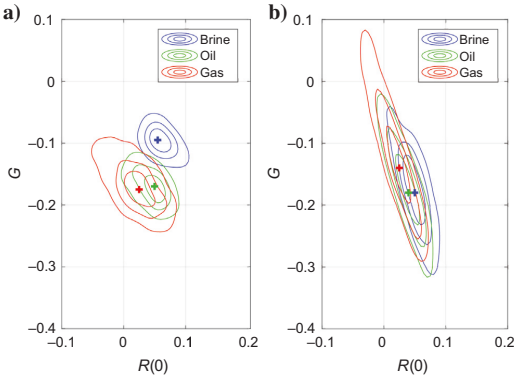

Figure 10. Class-conditional PDFs $P(R(0), G \mid c_j)$ resulting from a Monte Carlo simulation for (a) base models and (b) stringer models. Crosses show the locations of the maxima.

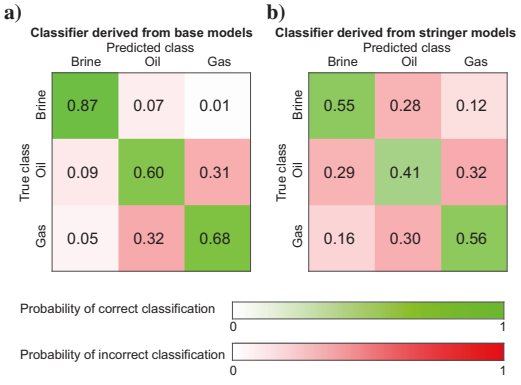

Figure 11. Confusion matrices showing the probabilities of different kinds of errors in the Bayesian classification for (a) the classifier derived from base models and (b) the classifier derived from stringer models assuming equal prior probabilities. Figures are rounded to two decimals.

DOI:10.1190/INT-2022-0084.1

$P(\text{brine} \mid \text{oil} \cup \text{gas})$ for base and stringer models are shown. The probability of a false-positive hydrocarbon indication increased from 3%–5% to 18%–21%. It should be noted that these results are valid under the assumption of equal prior probability, which should be replaced by a more realistic estimate in practice.

Tests on synthetic seismic data at well locations

Ideally, the Bayesian classifiers should be tested on seismic data at locations, where the pore-fluid class is known. In our case study, we used synthetic seismic data generated from well logs from the Alvheim Field using the reflectivity method. This approach has the advantage that the encountered pore fluids at the well locations are known. We included three test wells A–C that had not been used in the workflow and the nine training wells D–L that were used to estimate the lithology/fluid class PDFs. The 12 test models were built by using the target zone of the well logs (in true vertical depth, if available) and upward extrapolation to the water bottom. If necessary, V_S was estimated from V_P using the same procedure as mentioned previously. At calcite stringer locations, we assumed a V_P/V_S ratio of 1.67. Steps 3–6 of the workflow described in the "Methods" section were applied to the test data sets.

Table 2 shows the resulting posterior probabilities using the class-conditional PDFs derived from base models $P_b(c_j \mid R(0), G)$ and stringer models $P_s(c_j \mid R(0), G)$ in comparison to the true pore fluids, assuming equal prior probabilities for brine, oil, and gas. Despite their remarkable differences, the class-conditional PDFs from the base and stringer models performed surprisingly well in the Bayesian classification. Using the PDFs derived from the base models gave correct predictions in nine out of 12 cases, and the PDFs derived from the stringer models led to correct predictions in 10 out of 12 cases.

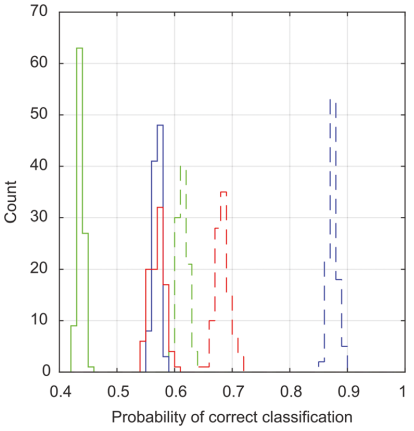

Figure 12. Bootstrapping results for the probabilities of the correct classification of the brine (the blue), oil (the green), and gas (the red) for the base model classifier (the dashed lines) and the stringer model classifier (the solid lines).

The better performance of the stringer model classifier indicates that the PDFs derived from stringer models provide a better estimate of probabilities than the PDFs derived from base models when calcite stringers are present. In wells C and K, the hydrocarbon columns are so short that their effect on the AVO is probably too small, and it is not surprising that classification based on the AVO attributes is prone to fail in these situations. Both classifiers failed to identify the oil zone in well H. As we had already observed previously, the discrimination between oil and gas based on the AVO attributes is challenging in the Alvheim Field. Many wells encountered a gas zone and an oil zone underneath. The probabilities at these wells are typically highest for gas, followed by oil. The test results indicate that the discrimination between hydrocarbon and brine is robust. Due to the overlap of the class-conditional PDFs derived from stringer models, in some cases the uncertainty can be high, as for wells B and K. Because these models include calcite stringers and are therefore more realistic, we expect that the PDFs derived from stringer models give better uncertainty estimates in the Bayesian classification.

One weakness of this approach for testing is that the test models were built based on raw well logs, which can be inaccurate at the calcite stringer locations. We expect that the measurements of V_P, V_S, and density are potentially underestimated and smeared out in depth at such locations.

Suggestions for further study

The approach of considering many realizations of the simple models of a homogeneous caprock and reservoir is a simplification that is commonly used (Avseth et al., 2001a, 2001b; Grana and Bronston, 2015). In fact, in these earlier studies, the AVO attributes were directly derived from rock-physics properties instead of via a seismic modeling procedure. Alternatively, convolutional seismic

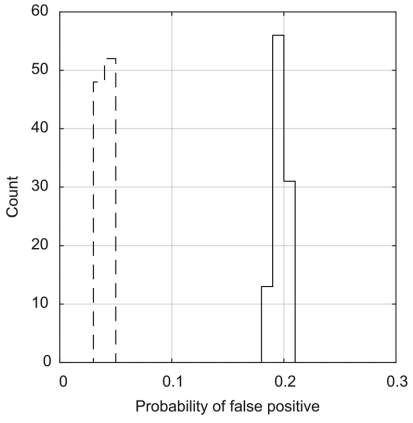

Figure 13. Bootstrapping results for the probability of a false-positive classification for the base models (the dashed lines) and stringer models (the solid lines).

modeling was used in other studies (Rimstad et al., 2012). Our approach involved advanced and realistic seismic forward modeling and migration because the inclusion of thin high-impedance layers required it. In addition, the procedure resembled the processing of seismic field data which should make the resulting PDFs more applicable to measured seismic attributes. The seismic modeling and migration were computationally more costly but still allowed a Monte Carlo simulation where many realizations are needed. We found that approximately 15 h were required to run 1000 realizations on a regular modern business laptop.

The usage of well-log data from several wells in the area helped to capture the variability of rock-physics properties vertically and laterally. In our case study, it was crucial to include wells at various locations because effects such as quartz cementation can lead to different seismic signatures (Avseth et al., 2009). We considered upscaling the well logs first to bring the rock-physics properties to the seismic scale (Avseth et al., 2005). However, this process reduced the variance of the data a lot and would have led to a strong imprint of individual wells on the resulting PDFs.

Turbidite reservoirs are characterized by depositional variability and complex distributions of sand lobes (Rimstad et al., 2012). Fluid discrimination by rock physics and the AVO can be hampered by the interplay of geologic factors such as quartz cementation, sorting, net-to-gross ratio, and shale anisotropy (Avseth et al., 2009; Golikov et al., 2013). We did not consider these factors directly in our study where we focused specifically on the effect of calcite cement. Another simplification is the assumption of full saturation by one pore fluid at a time, whereas actual rocks can be partially saturated by several fluids and many wells encountered a gas and an oil zone. One possibility would be to distinguish only between the brine and hydrocarbon in the workflow.

Accounts of the elastic properties of calcite-cemented beds in the literature are sparse. We came to the same conclusion as Bakke (1996) that the well-log measurements are unreliable in these very thin and hard intervals due to the averaging effects and shoulder-bed effects. Our approach of applying the Hill mixing law assuming a mixture of quartz and calcite grain can be considered as an approximation that needs to be confirmed, for example, by laboratory measurements. P-wave velocities above 6000 m/s were measured in some calcite-cemented intervals suggesting that our assumed values were realistic.

The AVO intercept and gradient are common AVO attributes in the seismic industry and the estimation by least-squares fitting of a straight line to measured amplitudes is a standard procedure (Chopra and Castagna, 2014). The tuning with calcite stringers can increase the misfit because the assumptions for the two-term AVO are not valid anymore. A large misfit could be used as an indicator for tuning with calcite stringers but might be masked by noise, residual multiples, etc., in field data.

We compared the class-conditional PDFs and Bayesian classification uncertainty in the absence of calcite stringers (base models) and the presence of calcite stringers (stringer models). For this purpose, it was beneficial to work with synthetic seismic data. There are several aspects that need to be considered when the AVO attributes from field data are used in lithology/fluid classification. Several types of noise can affect the amplitudes of the data, including residual multiples. As the true velocity field is unknown, the migration result will be imperfect and residual moveout might need to be corrected. Measurement uncertainty can be included in a probabilistic model (Avseth et al., 2005). We tested peak/trough-guided amplitude picking instead of measuring amplitudes at constant depth lev-

Table 2. Bayesian classification results for test data at well locations in comparison to observed pore fluids.

Well	$P_b(\text{brine}\mid\cdot)$	$P_b(\text{oil}\mid\cdot)$	$P_b(\text{gas}\mid\cdot)$	$P_s(\text{brine}\mid\cdot)$	$P_s(\text{oil}\mid\cdot)$	$P_s(\text{gas}\mid\cdot)$	True observation
A	0.05	0.46	**0.49**	0.00	0.20	**0.79**	32 m gas, 9 m oil
B	**0.87**	0.08	0.06	**0.35**	0.32	0.34	Brine
C	0.21	**0.77**	0.01	0.06	0.19	**0.75**	6 m gas
D	**0.93**	0.04	0.02	**0.71**	0.18	0.11	Brine
E	0.02	0.48	**0.50**	0.08	0.41	**0.52**	52 m gas, 17 m oil
F	0.00	0.23	**0.77**	0.01	0.22	**0.77**	25 m gas, 28 m oil
G	0.01	0.39	**0.60**	0.08	0.41	**0.51**	3 m gas, 5 m oil
H	0.00	0.24	**0.75**	0.00	0.24	**0.76**	48 m oil
I	0.00	0.06	**0.94**	0.00	0.00	**1.00**	9 m gas, 7 m oil
J	0.33	0.24	**0.43**	0.06	0.35	**0.59**	42 m gas, 8 m oil
K	**0.79**	0.15	0.06	**0.40**	0.28	0.33	1 m oil
L	**0.97**	0.02	0.00	**0.74**	0.14	0.12	Brine

Here, $P_b(\cdot|\cdot)$ denotes the probabilities from the base model PDFs, whereas $P_s(\cdot|\cdot)$ denotes the probabilities from the stringer model PDFs. The condition of all probabilities represented by a dot in the table header is a pair of the AVO attributes $(R(0), G)$. Figures are rounded to two decimals and bold figures indicate the highest posterior probability. Observed hydrocarbon columns are gross intervals. Wells A–C are test wells and wells D–L belong to the training data.

els in our workflow, but we found this to be too prone to errors when zero-offset reflectivity was low. There are many pitfalls in estimating the AVO attributes from seismic data (Avseth et al., 2005). Another important step is the calibration of the seismic AVO attributes to PDFs derived from the well logs, which can be achieved by covariance matching (Avseth et al., 2005). It also should be noted that the wavelet will influence offset-dependent tuning.

In the tests on synthetic data at well locations, both classifiers performed well despite their differences. The stringer model classifier performed slightly better and typically predicted higher uncertainties showing that the PDFs derived from stringer models are more realistic than those derived from clean base models. We are aware that the test data set is too small to make a valid evaluation and that the classifiers should be tested on seismic field data in future work. It should be noted that it was not the goal of the study to create an optimal Bayesian classifier but rather to quantify the change in uncertainty that is caused by the presence of calcite stringers interfering with the target AVO.

We have several suggestions for future work on building an optimal Bayesian prediction model for the Alvheim Field. Other geologic factors, such as quartz cementation, sorting, net-to-gross ratio and shale anisotropy, and their depth dependency should be included. The probability of the presence of calcite stringers should be carefully assessed, for example, by evaluating all available well data. Furthermore, it should be attempted to estimate prior probabilities from the data instead of assuming equal prior probabilities. Once the class-conditional PDFs are derived from the data, the priors can be varied easily to analyze how sensitive the Bayesian classification is to varying a priori assumptions.

The presented workflow can be applied to estimate uncertainties of the AVO attributes in areas, where calcite stringers or similar thin high-impedance layers are present. The uncertainty estimates are valuable for risk assessment prior to drilling. As discussed, regionally adapted Bayesian classifiers can be created that include the potential amplitude tuning with calcite stringer reflections. Such classifiers then can be applied to field seismic AVO attributes.

Conclusion

With a simple example inspired by well data from the Alvheim Field, we have demonstrated that a thin calcite-cemented bed may lead to a detectable reflection response owing to its high acoustic impedance and that this signal can interfere with a target reflection response altering the AVO. Such a tuning effect might lead to a false hydrocarbon AVO indication. Therefore, the goal of this study was to quantify the uncertainty in the Bayesian pore-fluid classification from the AVO attributes caused by interference with calcite stringers. We have developed a workflow that estimates the PDFs from two types of models, one that ignored calcite stringers and one that included them. For these two types of models, we then evaluated the corresponding probabilities of correct and incorrect classification. The workflow was applied to well data from the Alvheim Field, where we found that the classification uncertainty was significantly increased by the presence of calcite stringers. The probability of a false-positive hydrocarbon indication increased from 3%–5% to 18%–21% when an equal probability of the occurrence of brine, oil, and gas was assumed. We tested two Bayesian classifiers, one ignoring and one including calcite stringers, on synthetic seismic data at well locations. Both classifiers achieved good classification results with a slightly better performance of the classifier that took calcite stringers into account. We concluded that calcite stringers may create an AVO pitfall and should not be ignored. Our proposed workflow provides uncertainty estimates that can be used in predrilling risk assessment for AVO anomalies in mature areas. In frontier areas with poor well control, the workflow could be applied using statistical properties derived from the analog areas.

Acknowledgments

We would like to thank P. Avseth and H. Hoeber for inspiring and fruitful discussions. We are thankful for the comments and suggestions from three anonymous reviewers that helped us to improve the manuscript. CGG Earth Data is acknowledged for assistance in gathering and processing the well data. E. Rietsch is acknowledged for developing and providing the MATLAB software package SeisLab. We used well-log data from the Diskos data repository. Well data (except logs) were distributed by the Norwegian Petroleum Directorate under the Norwegian Licence for Open Government Data (NLOD). The first author received funding from the Research Council of Norway under grant no. 310441.

Data and materials availability

The well logs used in this study are available for Diskos members at the Diskos data repository (the Norwegian National Data Repository for Petroleum data, https://www.npd.no/en/diskos). Further well-related data are publicly available at the Factpages of the Norwegian Petroleum Directorate (https://factpages.npd.no).

References

Aki, K., and P. G. Richards, 2002, Quantitative seismology, 2nd ed.: University Science Books.

Alhussain, M., B. Gurevich, and M. Urosevic, 2008, Experimental verification of spherical-wave effect on the AVO response and implications for three-term inversion: Geophysics, **73**, no. 2, C7–C12, doi: 10.1190/1.2837641.

Alulaiw, B., and B. Gurevich, 2013, Analytical wavefront curvature correction to plane-wave reflection coefficients for a weak-contrast interface: Geophysical

Prospecting, **61**, 53–62, doi: 10.1111/j.1365-2478.2012.01060.x.

Avseth, P., A. Dræge, A.-J. van Wijngaarden, T. A. Johansen, and A. Jørstad, 2008, Shale rock physics and implications for AVO analysis: A North Sea demonstration: The Leading Edge, **27**, 788–797, doi: 10.1190/1.2944164.

Avseth, P., H. Flesche, and A.-J. V. Wijngaarden, 2003, AVO classification of lithology and pore fluids constrained by rock physics depth trends: The Leading Edge, **22**, 1004–1011, doi: 10.1190/1.1623641.

Avseth, P., A. Janke, and F. Horn, 2016, AVO inversion in exploration — Key learnings from a Norwegian Sea prospect: The Leading Edge, **35**, 405–414, doi: 10.1190/tle35050405.1.

Avseth, P., A. Jørstad, A.-J. van Wijngaarden, and G. Mavko, 2009, Rock physics estimation of cement volume, sorting, and net-to-gross in North Sea sandstones: The Leading Edge, **28**, 98–108, doi: 10.1190/1.3064154.

Avseth, P., I. Lehocki, Ø. Kjøsnes, and O. Sandstad, 2021, Data-driven rock physics analysis of North Sea tertiary reservoir sands: Geophysical Prospecting, **69**, 608–621, doi: 10.1111/1365-2478.12986.

Avseth, P., T. Mukerji, A. Jørstad, G. Mavko, and T. Veggeland, 2001b, Seismic reservoir mapping from 3-D AVO in a North Sea turbidite system: Geophysics, **66**, 1157–1176, doi: 10.1190/1.1487063.

Avseth, P., T. Mukerji, and G. Mavko, 2005, Quantitative seismic interpretation: Applying rock physics tools to reduce interpretation risk: Cambridge University Press.

Avseth, P., T. Mukerji, G. Mavko, and J. A. Tyssekvam, 2001a, Rock physics and AVO analysis for lithofacies and pore fluid prediction in a North Sea oil field: The Leading Edge, **20**, 429–434, doi: 10.1190/1.1438968.

Bakke, N. E., 1996, Prediction of calcite cement distribution in shallow marine sandstone reservoirs using seismic data: Degree of Doktor Ingeniør thesis, Norwegian University of Science and Technology.

Bakke, N. E., and B. Ursin, 1998, Thin-bed AVO effects: Geophysical Prospecting, **46**, 571–587, doi: 10.1046/j.1365-2478.1998.00101.x.

Bjørkum, P. A., and O. Walderhaug, 1990a, Geometrical arrangement of calcite cementation within shallow marine sandstones: Earth-Science Reviews, **29**, 145–161, doi: 10.1016/0012-8252(90)90033-R.

Bjørkum, P. A., and O. Walderhaug, 1990b, Lateral extent of calcite-cemented zones in shallow marine sandstones, *in* A. T. Buller, E. Berg, O. Hjelmeland, J. Kleppe, O. Torsæter, and J. O. Aasen, eds., North Sea oil and gas reservoirs — II: Springer, 331–336.

Bjørlykke, K., 1998, Clay mineral diagenesis in sedimentary basins — A key to the prediction of rock properties. Examples from the North Sea Basin: Clay Minerals, **33**, 15–34, doi: 10.1180/000985598545390.

Bryant, I. D., J. D. Kantorowicz, and C. F. Love, 1988, The origin and recognition of laterally continuous carbonate-cemented horizons in the Upper Lias Sands of southern England: Marine and Petroleum Geology, **5**, 108–133, doi: 10.1016/0264-8172(88)90018-9.

Buland, A., and H. Omre, 2003, Bayesian linearized AVO inversion: Geophysics, **68**, 185–198, doi: 10.1190/1.1543206.

Castagna, J. P., and M. M. Backus, 1993, Offset-dependent reflectivity — Theory and practice of AVO analysis: SEG.

Castagna, J. P., H. W. Swan, and D. J. Foster, 1998, Framework for AVO gradient and intercept interpretation: Geophysics, **63**, 948–956, doi: 10.1190/1.1444406.

Cavazza, W., and J. Dahl, 1990, Note on the temporal relationships between sandstone compaction and precipitation of authigenic minerals: Sedimentary Geology, **69**, 37–44, doi: 10.1016/0037-0738(90)90099-F.

Červený, V., 1961, The amplitude curves of reflected harmonic waves around the critical point: Studia Geophysica et Geodaetica, **5**, 319–351, doi: 10.1007/BF02585404.

Červený, V., and R. Ravindra, 1971, Theory of seismic head waves: University of Toronto Press.

Chopra, S., and J. P. Castagna, 2014, AVO: SEG.

de Sousa, M. C., J. J. S. de Figueiredo, C. B. da Silva, and M. J. de S. Nascimento, 2019, Prediction of S-wave velocity by a hybrid model based on the Greenberg-Castagna equation: Journal of Petroleum Science and Engineering, **172**, 303–313, doi: 10.1016/j.petrol.2018.09.014.

Dutta, T., T. Mukerji, and G. Mavko, 2008, How does carbonate cementation in sandstones affect seismic response? 78th Annual International Meeting, SEG, Expanded Abstracts, 1675–1679, doi: 10.1190/1.3059230.

Efron, B., 1979, Bootstrap methods: Another look at the jackknife: The Annals of Statistics, **7**, 1–26, doi: 10.1214/aos/1176344552.

Eidsvik, J., H. Omre, T. Mukerji, G. Mavko, and P. Avseth, 2002, Seismic reservoir prediction using Bayesian integration of rock physics and Markov random fields: A North Sea example: The Leading Edge, **21**, 290–294, doi: 10.1190/1.1463780.

Gassmann, F., 1951, Über die Elastizität poröser Medien: Vierteljahrsschrift der Naturforschenden Gesellschaft in Zürich, **96**, 1–23.

Gibbons, K., T. Hellem, A. Kjemperud, S. D. Nio, and K. Vebenstad, 1993, Sequence architecture, facies development and carbonate-cemented horizons in the Troll Field reservoir, offshore Norway: Advances in Reservoir Geology, **69**, 1–31.

Gibson, R. L., Jr., 2004, Composite reflection coefficients for stratified reservoir models: 74th Annual International Meeting, SEG, Expanded Abstracts, 267–270, doi: 10.1190/1.1851263.

Gibson, R. L., Jr., 2005, Influence of internal reservoir structure on composite reflection coefficients: 75th Annual International Meeting, SEG, Expanded Abstracts, 312–315, doi: 10.1190/1.2144330.

Gisolf, A., P. R. Haffinger, and P. Doulgeris, 2021, AVO modelling and interpretation with the help of the 1.5D elastic wave-equation: First Break, **39**, 93–100, doi: 10.3997/1365-2397.fb2021025.

Golikov, P., P. Avseth, A. Stovas, and R. Bachrach, 2013, Rock physics interpretation of heterogeneous and anisotropic turbidite reservoirs: Geophysical Prospecting, **61**, 448–457, doi: 10.1111/j.1365-2478.2012.01073.x.

Grana, D., L. Azevedo, L. de Figueiredo, P. Connolly, and T. Mukerji, 2022, Probabilistic inversion of seismic data for reservoir petrophysical characterization: Review and examples: Geophysics, **87**, no. 5, M199–M216, doi: 10.1190/geo2021-0776.1.

Grana, D., and M. Bronston, 2015, Probabilistic formulation of AVO modeling and AVO-attribute-based facies classification using well logs: Geophysics, **80**, no. 4, D343–D354, doi: 10.1190/geo2014-0518.1.

Hanitzsch, C., J. Schleicher, and P. Hubral, 1994, True-amplitude migration of 2D synthetic data: Geophysical Prospecting, **42**, 445–462, doi: 10.1111/j.1365-2478.1994.tb00220.x.

Hill, R., 1952, The elastic behaviour of a crystalline aggregate: Proceedings of the Physical Society, Section A, **65**, 349–354, doi: 10.1088/0370-1298/65/5/307.

Juhlin, C., and R. Young, 1993, Implications of thin layers for amplitude variation with offset (AVO) studies: Geophysics, **58**, 1200–1204, doi: 10.1190/1.1443504.

Kantorowicz, J. D., I. D. Bryant, and J. M. Dawans, 1987, Controls on the geometry and distribution of carbonate cements in Jurassic sandstones: Bridport Sands, southern England and Viking Group, Troll Field, Norway: Geological Society, London, Special Publications 36.

Kennett, B. L. N., 1979, Theoretical reflection seismograms for elastic media: Geophysical Prospecting, **27**, 301–321, doi: 10.1111/j.1365-2478.1979.tb00972.x.

Kennett, B. L. N., 2009, Seismic wave propagation in stratified media, New ed.: ANU E Press.

Krail, P. M., and H. Brysk, 1983, Reflection of spherical seismic waves in elastic layered media: Geophysics, **48**, 655–664, doi: 10.1190/1.1441496.

Larsen, A. L., M. Ulvmoen, H. Omre, and A. Buland, 2006, Bayesian lithology/fluid prediction and simulation on the basis of a Markov-chain prior model: Geophysics, **71**, no. 5, R69–R78, doi: 10.1190/1.2245469.

Liu, Y., and D. R. Schmitt, 2003, Amplitude and AVO responses of a single thin bed: Geophysics, **68**, 1161–1168, doi: 10.1190/1.1598108.

Lörtzer, G. J. M., and A. J. Berkhout, 1992, An integrated approach to lithologic inversion — Part I: Theory: Geophysics, **57**, 233–244, doi: 10.1190/1.1443236.

McBride, E. F., K. L. Milliken, W. Cavazza, U. Cibin, D. Fontana, M. D. Picard, and G. G. Zuffa, 1995, Heterogeneous distribution of calcite cement at the outcrop scale in tertiary sandstones, northern Apennines, Italy: AAPG Bulletin, **79**, 1044–1062, doi: 10.1306/8D2B21C3-171E-11D7-8645000102C1865D.

Müller, G., 1985, The reflectivity method: A tutorial: Journal of Geophysics — Zeitschrift für Geophysik, **58**, 153–174.

Norwegian Petroleum Directorate, n.d., Factpages, https://factpages.npd.no/en, accessed 27 June 2022.

Pan, W., and K. A. Innanen, 2013, AVO/AVF analysis of thin beds in elastic media: 83rd Annual International Meeting, SEG, Expanded Abstracts, 373–377, doi: 10.1190/segam2013-0587.1.

Rimstad, K., P. Avseth, and H. Omre, 2012, Hierarchical Bayesian lithology/fluid prediction: A North Sea case study: Geophysics, **77**, no. 2, B69–B85, doi: 10.1190/geo2011-0202.1.

Russell, B. H., 1988, 2. Part 2 — The convolutional model, *in* S. N. Domenico, ed., Introduction to seismic inversion methods: SEG, 2-1–2-19.

Saigal, G. C., and K. Bjørlykke, 1987, Carbonate cements in clastic reservoir rocks from offshore Norway — Relationships between isotopic composition, textural development and burial depth: Diagenesis of Sedimentary Sequences, **36**, 313–324.

Shuey, R. T., 1985, A simplification of the Zoeppritz equations: Geophysics, **50**, 609–614, doi: 10.1190/1.1441936.

Silverman, B. W., 1986, Density estimation for statistics and data analysis: Chapman and Hall.

Stovas, A., M. Landrø, and P. Avseth, 2006, AVO attribute inversion for finely layered reservoirs: Geophysics, **71**, no. 3, C25–C36, doi: 10.1190/1.2197487.

Tschache, S., V. Vinje, and E. Iversen, 2022, On the accuracy and spatial sampling of finite-difference modelling in discontinuous models: Journal of Applied Geophysics, **206**, 104789, doi: 10.1016/j.jappgeo.2022.104789.

Ulvmoen, M., and H. Omre, 2010, Improved resolution in Bayesian lithology/fluid inversion from prestack seismic data and well observations: Part 1 — Methodology: Geophysics, **75**, no. 2, R21–R35, doi: 10.1190/1.3294570.

Ulvmoen, M., H. Omre, and A. Buland, 2010, Improved resolution in Bayesian lithology/fluid inversion from prestack seismic data and well observations: Part 2 — Real case study: Geophysics, **75**, no. 2, B73–B82, doi: 10.1190/1.3335332.

Walderhaug, O., and P. A. Bjørkum, 1992, Effect of meteoric water flow on calcite cementation in the Middle Jurassic Oseberg Formation, well 30/3-2, Veslefrikk Field, Norwegian North Sea: Marine and Petroleum Geology, **9**, 308–318, doi: 10.1016/0264-8172(92)90079-T.

Walderhaug, O., and P. A. Bjørkum, 1998, Calcite cement in shallow marine sandstones: Growth mechanisms and geometry, *in* S. Morad, ed., Carbonate cementation in sandstones: Blackwell Science, 179–192.

Walderhaug, O., P. A. Bjørkum, and H. M. N. Bolås, 1989, Correlation of calcite-cemented layers in shallow-marine sandstones of the Fensfjord Formation in the Brage Field, *in* J. D. Collinson, ed., Correlation in hydrocarbon exploration: Springer, 367–375.

Widess, M. B., 1973, How thin is a thin bed? Geophysics, **38**, 1176–1180, doi: 10.1190/1.1440403.

Yang, C., Y. Wang, and Y. Wang, 2016, Reflection and transmission coefficients of a thin bed: Geophysics, **81**, no. 5, N31–N39, doi: 10.1190/geo2015-0360.1.

Biographies and photographs of the authors are not available.

Article III: Estimation of net-to-gross ratio and net pay from seismic amplitude variation with offset using Bayesian inversion

Saskia Tschache
Vetle Vinje
Jan Erik Lie
Martin Brandtzæg Gundem
Einar Iversen

submitted to *Interpretation* 5 April 2023

Estimation of net-to-gross ratio and net pay from seismic amplitude variation with offset using Bayesian inversion

Saskia Tschache[1,2], Vetle Vinje[3], Jan Erik Lie[4], Martin Brandtzæg Gundem[4], and Einar Iversen[2]

[1]CGG, Crawley, UK
[2]Department of Earth Science, University of Bergen, Bergen, Norway
[3]CGG, Oslo, Norway
[4]AkerBP, Lysaker, Norway

April 5, 2023

Abstract

Net-to-gross ratio and net pay are essential properties for characterizing turbidite reservoirs. We present a Bayesian inversion that estimates the probability density distributions of the reservoir properties from the amplitude-variation-with-offset (AVO) attributes intercept and gradient, which are measured at the top of the reservoir. The method is adapted to the region-specific characteristics of the sand-shale interbedding as observed from well data. The likelihood function is estimated by a Monte Carlo simulation, pseudo-wells, and seismic modeling using the reflectivity method. In a North Sea oil field case example, the AVO gradient is most sensitive to variations in the net-to-gross ratio, while the AVO intercept is most sensitive to the type of pore fluid. The inversion was successfully tested on pseudo-wells and synthetic seismic AVO from well data. We show that the inversion can be applied to AVO maps to produce maps of the most likely estimates of the net-to-gross ratio and the net pay-to-net ratio, the resulting net pay, and the uncertainty.

Introduction

Turbidite reservoirs can be found in sedimentary basins around the world (Weimer and Link, 1991) and are important exploration targets for the oil and gas industry. Turbidite systems are often complex (Avseth, 2000) and characterized by a sand-shale interbedding with bed thicknesses below the seismic resolution (Lai and Gibson, 2005; Stovas et al., 2006). The sand-shale distribution of a reservoir determines the net-to-gross ratio (N/G), the fraction of reservoir-quality sand (net) of a gross reservoir thickness. This property is of great interest for reservoir characterization because it is related to the reservoir quality and the potential fluid content. Another interesting property is the net pay

of a reservoir, which comprises only those net reservoir intervals that are sufficiently saturated by hydrocarbons for economic production.

Several authors attempted the estimation of N/G from seismic data. Takahashi et al. (1999) estimated the sand-shale ratio from zero-offset seismic reflectivity using stochastic simulation and Bayesian inversion. They found that the sand-shale ratio is not well constrained by zero-offset reflectivity alone, leading to high uncertainty. Vernik et al. (2002) used volumes of acoustic impedance (AI) and shear impedance (SI) from seismic prestack inversion together with facies-dependent trends in the AI-SI domain to estimate the sand volume. Integration over the gross reservoir interval yielded N/G. Stovas et al. (2006) developed an amplitude-variation-with-offset (AVO) attribute inversion for N/G and fluid saturation based on binary effective media and considered the uncertainty of this estimation in Stovas and Landrø (2006). Connolly (2007) used band-limited impedance data from colored inversion to estimate seismic N/G and net pay after a detuning process. Rietsch (2008) proposed to determine the net-sand thickness of a reservoir by applying a probe function to the zero-offset seismic reflection response of a layered sand-shale package. Avseth et al. (2009) used effective medium theory to model the rock properties of interbedded sand-shale sequences considering different pore-fluid scenarios. Spikes (2009) applied a Bayesian classification scheme to invert seismic zero-offset amplitudes for saturation and N/G. Connolly and Hughes (2016) proposed a 1D stochastic inversion of band-limited impedance traces to estimate the mean and standard deviation of N/G. Pradhan and Mukerji (2020) applied Bayesian evidential learning to estimate N/G and average fluid saturation and the corresponding uncertainty from near- and far-offset seismic waveforms.

The usage of the seismic AVO attributes, intercept and gradient, is common in seismic exploration (Chopra and Castagna, 2014). The previously mentioned studies and the investigations by Vernik (2016) suggest that these attributes are sensitive to changes in N/G and fluid saturation. There is also a strong consensus in academic literature that the AVO gradient is more sensitive to variations in N/G than the AVO intercept (Stovas et al., 2006; Vernik, 2016).

It is important to note the scale dependency of seismic wave propagation in stratified media. Depending on the seismic wavelength and scale of heterogeneity, ray theory, scattering theory, or effective medium theory are applicable (Marion et al., 1994; Takahashi, 2000). Effective medium theory is valid if individual layers are considerably thinner than the seismic wavelength, while the exact limit depends on the reflectivity contrast (Stovas et al., 2006). As layers become thicker and the effective medium limit is transgressed, scattering effects need to be considered. To correctly simulate scattering in finely layered models, simple primaries-only convolutional modeling is not adequate (Stovas et al., 2006). Instead, full-wavefield propagator-matrix or reflectivity methods need to be used (Marion et al., 1994; Stovas et al., 2006).

Periodic binary models, as used in the modeling study by Stovas et al. (2006), are illustrative but neglect the variation of individual layer thickness and the variability of elastic properties of sand and shale beds. A method for generating more realistic stratified models of turbidite sequences was proposed by Lai and Gibson (2005) using well-data-derived cumulative density functions for bed thickness, velocity, and density. Takahashi et al. (1999) applied geostatistical sequential indicator simulation for the generation of layered models. In this way, equiprobable models for a certain sand-shale ratio can be generated that honor the vertical correlation observed in well data. 1D synthetic stratigraphic sequences with attached physical properties (pseudo-wells)

were used by many authors to better understand the relationship between seismic and lithology (Sinvhal and Khattri, 1983; Gancarski et al., 1994; Joseph et al., 1999). More recently, pseudo-wells have been used to train artificial neural networks (Das et al., 2019; Allo et al., 2021).

We build on the work by Takahashi et al. (1999) and Stovas et al. (2006) to study the level of confidence with which local reservoir properties can be determined based on AVO attributes measured at the reservoir top. As opposed to Takahashi et al. (1999), we use AVO intercept and gradient and not only zero-offset reflectivity. Additionally, we include the variability of the elastic properties of sand and shale layers and the pore-fluid effect. In contrast to Stovas et al. (2006) and many other studies, we do not use effective medium theory. As already shown by Takahashi et al. (1999), using an effective medium does not honor the actual non-uniqueness of N/G-estimation from seismic AVO attributes. As discussed, the effective medium limit is dependent on the ratio of wavelength to layer thickness and the acoustic impedance contrast. An increased seismic frequency, layer thickness, or impedance contrast (or a combination of the three) can easily make effective medium theory inaccurate and make the consideration of scattering effects necessary.

Recently, there has been increased interest and success in the probabilistic inversion of seismic data for reservoir properties (Grana et al., 2022). The advantage of probabilistic inversions, such as Bayesian methods, is that they honor the non-uniqueness of the inverse problem and provide an uncertainty estimate in addition to the most likely solution. Quantification of uncertainty is valuable for decision-making (Grana et al., 2022).

We apply a combination of stochastic simulation and full-wavefield seismic forward modeling to estimate probabilities of AVO attributes at the reservoir top for varying N/G and net pay of a reservoir to be used in a Bayesian inversion. The inversion is applied to pseudo-wells, synthetic seismic data at well locations, and AVO attributes from field data. We further investigate which seismic forward modeling technique is optimal for the proposed workflow and what impact the wavelet has on the extracted AVO attributes.

Method

We developed a Bayesian inversion that is adapted to the characteristics of a specific reservoir by well data. The idea behind our approach is to capture the depth (vertical) heterogeneity of the caprock and reservoir and the variability of rock physical properties observed from well data under the assumption that the reservoir is composed of sand and shale layers that determine the net-to-gross ratio N/G. We define N/G as the cumulative thickness of all sand layers in the reservoir interval divided by the gross reservoir thickness. Furthermore, we introduce the parameter net-pay-to-net ratio NP/N as the fraction of the cumulative thickness of oil-saturated sand intervals of the net reservoir. For simplicity, we assume that the sand intervals are fully saturated by one single pore fluid, either brine or oil. The NP/N determines the location of the oil-water contact (OWC). All sand intervals above the OWC are fully oil-saturated and all sand intervals below the OWC are fully brine-saturated. Figure 1 explains the defined variables with an example. The figure also illustrates that the theoretical sensitivity interval of the reflection response from the reservoir top is half the length of the respective wavelet.

The statistics (histograms, vertical correlation) obtained from many sand and shale layers sampled by well logs are used to produce a huge number of pseudo-wells composed

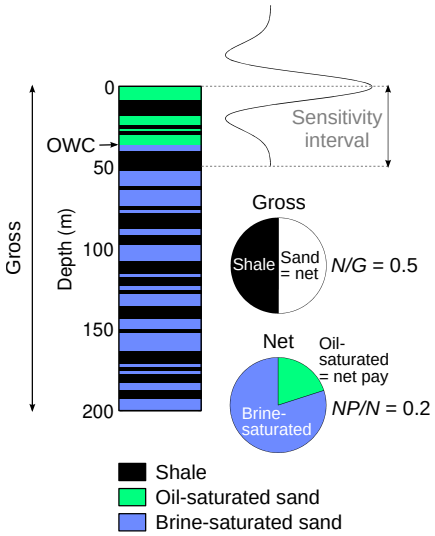

Figure 1: Illustration of the variables gross, net, net pay, and the oil-water-contact (OWC) on a simple example of a sand-shale interbedded reservoir with a net-to-gross ratio N/G of 50 % and a net-pay-to-net ratio NP/N of 20 %. The sensitivity interval of half a wavelet length is indicated. The example is a 30 Hz Ricker wavelet converted to depth using a constant velocity of 3000 m/s.

of sand and shale layers. For any given N/G and NP/N, many possible shale-sand interbedding scenarios in the form of pseudo-wells can be generated. This makes it possible to estimate the probability density distribution of AVO attributes given a fixed N/G and NP/N by using seismic modeling, amplitude picking at the reservoir top, and linear curve fitting to obtain AVO intercept $R(0)$ and gradient G. Available well data and other a priori information from regional stratigraphic studies can be used to build a model of prior probability $p(N/G, NP/N)$.

An overview of the complete workflow is shown in Figure 2. Once the probability density distributions are computed by the Monte Carlo simulation, the inversion can take AVO data, e.g., from AVO attribute maps of the reservoir top, as an input to yield a probability density function of N/G and NP/N for each data point ($R(0)$, G).

Generation of pseudo-wells

For the Monte Carlo simulation in our study, many pseudo-wells with a fixed N/G and NP/N are required. This can be achieved by geostatistical simulation (Takahashi et al., 1999). The pseudo-wells used in this study have the following structure from top to bottom: a 400 m thick shale overburden followed by a 100 m thick caprock unit and a 200 m thick reservoir unit that is bounded by a constant shale layer. The elastic properties of the overburden and the deepest layer are derived from well data. In our case example, we use a P-wave velocity V_P of 2600 m/s, an S-wave velocity V_S of 1136 m/s, and a density ρ of 2.33 g/cm^3. The simulation of the properties of the caprock and reservoir units is explained in the following two sub-subsections.

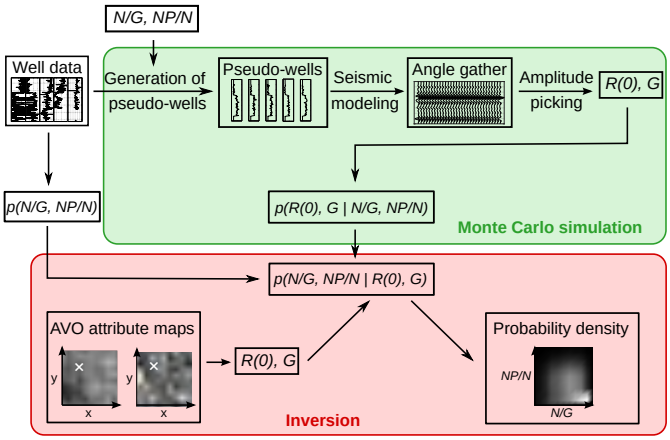

Figure 2: Workflow for the estimation of probability density distributions by Monte Carlo simulation to be used in a Bayesian inversion for net-to-gross ratio N/G and net-pay-to-net ratio NP/N given the AVO attributes intercept $R(0)$ and gradient G.

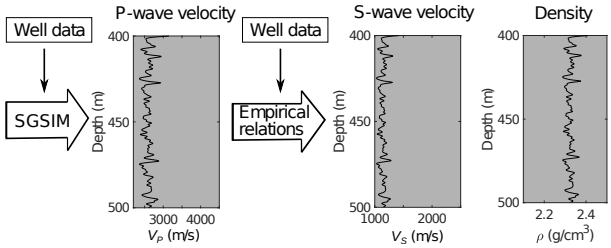

Figure 3: Workflow for the generation of the caprock interval of pseudo-wells. The P-wave velocity is simulated by Sequential Gaussian Simulation (SGSIM). The S-wave velocity and density are computed by empirical relations.

Caprock

The vertical heterogeneity of the caprock can impact the AVO of the composite top reservoir reflection response and, therefore, needs to be considered by the pseudo-wells. The workflow for the simulation of the caprock interval of the pseudo-wells is shown in Figure 3. The caprock properties of the well data in the interval above the reservoir top are analyzed to obtain the histogram of V_P, the spherical semivariogram model parameters of V_P, and the empirical linear relations between V_S and V_P and between ρ and V_P. A Sequential Gaussian Simulation (SGSIM; Deutsch and Journel, 1992; Goovaerts, 1997; Remy et al., 2009) is then used to simulate a V_P-log. Using the data-derived linear relations, V_S and ρ are computed from V_P. Detailed parameters of the caprock simulation applied in our case example are given in Table 1.

Parameter	Value(s)
Number of realizations for a specific N/G and NP/N	100
Vertical sampling interval	0.125 m
Caprock thickness	100 m
V_P semivariogram model range	1.92 m
V_P semivariogram model sill	1
V_S regression model intercept	-123.15 m/s
V_S regression model slope	0.49
ρ regression model intercept	1.93 g/cm^3
ρ regression model slope	1.53×10^{-4} g/cm^3 s/m

Table 1: Parameters of pseudo-well generation workflow for the caprock unit derived from data from three wells.

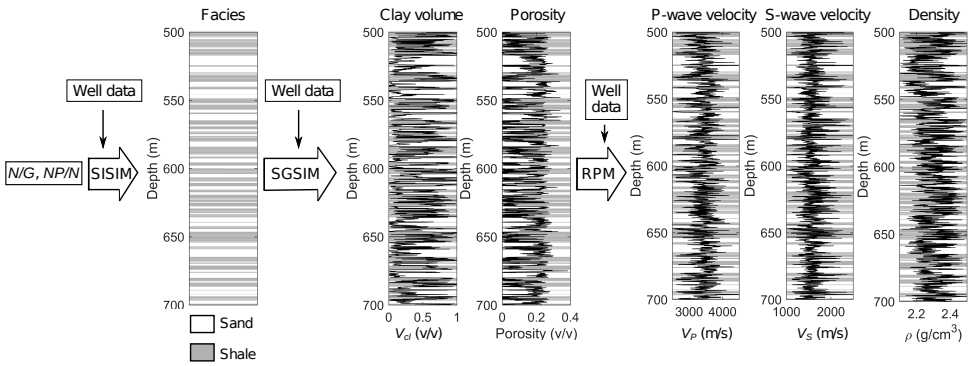

Figure 4: Workflow for the generation of the reservoir interval of pseudo-wells. In this example, the net-to-gross ratio N/G is 0.5, the net-pay-to-net ratio NP/N is 0.2, and the vertical sampling is 0.125 m. Facies models of sand and shale layers are generated by Sequential Indicator Simulation (SISIM). Clay volume and porosity are simulated by Sequential Gaussian Simulation (SGSIM). Finally, elastic properties are computed using a rock-physics model (RPM).

Reservoir

For the simulation of the reservoir interval of the pseudo-wells, we developed a multistage workflow, shown in Figure 4, that takes the statistical information of measured well data into account. The workflow draws on previous work by Takahashi et al. (1999), Das et al. (2019), and Allo et al. (2021). The detailed parameters of the simulation in our case example based on three wells are given in Table 2.

In the first step, equiprobable binary facies models are generated. Each facies model represents a sequence of sand and shale layers with variable individual layer thicknesses. The simulation is performed by a geostatistical Sequential Indicator Simulation (SISIM; Deutsch and Journel, 1992; Goovaerts, 1997; Remy et al., 2009) using a spherical semivariogram model fitted to experimental vertical semivariograms from well data. The well data have been interpreted by petrophysicists and each sample of the reservoir unit has been classified as either shale or sand. The SISIM algorithm constrains the N/G by marginal probabilities for the occurrence of sand and shale, respectively, and the vertical

Parameter	Value(s)
N/G	0 to 1 in steps of 0.1
NP/N	0 to 1 in steps of 0.1
Number of realizations for a specific N/G and NP/N	100
Vertical sampling interval	0.125 m
Reservoir thickness	200 m
Facies semivariogram model range	3.21 m
Facies semivariogram model sill	0.19
Clay volume semivariogram model range	1.05 m
Clay volume semivariogram model sill	1
Correlation coefficient of clay volume and porosity	-0.61
Cement volume	0.005
Bulk modulus of quartz	36.8 GPa
Shear modulus of quartz	44 GPa
Density of quartz	2.65 g/cm^3
Bulk modulus of clay	12 GPa
Shear modulus of clay	3 GPa
Density of clay	2.35 g/cm^3
Bulk modulus of brine	2.24 GPa
Density of brine	1.00 g/cm^3
Bulk modulus of oil	1.20 GPa
Density of oil	0.76 g/cm^3
Cement cohesion coefficient (Allo, 2019)	1 (0.3 to fit V_S)
Critical porosity	0.39
Coordination number	8

Table 2: Parameters of the pseudo-well generation workflow for the reservoir unit derived from data from three wells.

correlation of the facies by the given semivariogram model.

In the second step, SGSIM is applied to populate the sand and shale layers of a facies model with the petrophysical properties clay volume and porosity. A spherical semivariogram model of clay volume is derived from the well data and constrains the vertical correlation during the simulation. The porosity is simulated from the bivariate Gaussian distribution of the normal score transformed variables (Goovaerts, 1997) to take the negative correlation between porosity and clay volume into account (Doyen, 2007). The SGSIM algorithm reproduces the facies-dependent histograms of clay volume and porosity.

In the third step, a rock-physics model (RPM; Allo, 2019; Allo et al., 2021) is used to compute the elastic properties V_P, V_S, and ρ given the simulated clay volume and porosity values and the pore fluid (in case of a sand layer). The RPM shown in Figure 5 together with the well data is a constant-cement model (Avseth et al., 2000) of 0.05 % quartz cement. The saturated-rock properties are computed by the Gassmann model (Gassmann, 1951).

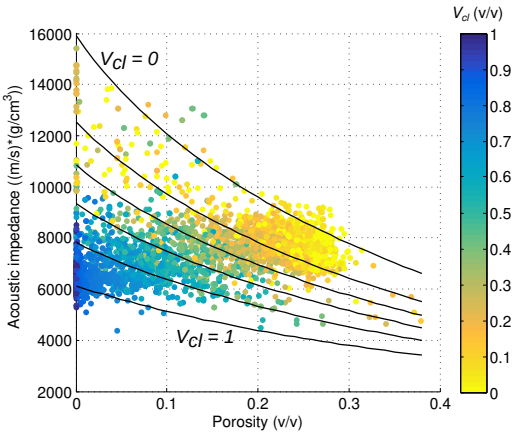

Figure 5: Acoustic impedance vs. porosity crossplot of the reservoir formation data from three wells. The clay volume V_{cl} is represented by color. The fitted constant-cement rock-physics model is shown as black lines.

Seismic forward modeling

The seismic forward modeling engine as part of the Monte Carlo simulation, where many possible realizations are considered, needs to be both accurate for finely layered media and computationally fast. We compare three modeling algorithms with respect to amplitude accuracy and computation time: primaries-only convolutional modeling (CM), the plane-wave reflectivity method (PRM), and the spherical-wave reflectivity method (SRM).

CM (Russell, 1988) uses angle-dependent reflectivity series $r(t, \theta)$ of primary reflections from the Zoeppritz equations or their approximations that are convolved with a wavelet $f(t)$ to produce angle gathers

$$S(t, \theta) = f(t) * r(t, \theta) \ . \tag{1}$$

This method is widely used and extremely efficient but neglects multiple reflections, mode conversions, and transmission loss.

The PRM computes the full-wavefield response of an elastic layered medium to harmonic plane waves using an iterative computation scheme (Kennett, 1974; 2009). The resulting complex reflectivity $r(\omega, p)$ is given in the frequency-slowness domain, where ω denotes radial frequency and p is the horizontal slowness or ray parameter. The corresponding response $S(\tau, p)$ of a seismic signal $f(\omega)$ in τ-p domain with intercept time τ can be obtained by convolution and inverse temporal Fourier transform

$$S(\tau, p) = \frac{1}{2\pi} \int_{-\infty}^{\infty} f(\omega) r(\omega, p) e^{i\omega\tau} d\omega \ . \tag{2}$$

Oliveira et al. (2018) proposed a procedure to transform synthetic τ-p seismograms to angle gathers. First, a τ-p normal-moveout correction is applied (van der Baan, 2004). Then, the horizontal slowness $p = \frac{\sin\theta}{V_P(\tau)}$ is mapped to the incidence angle θ using a smoothed velocity model $V_P(\tau)$ in time. The result is a synthetic plane-wave angle gather $S(\tau, \theta)$. In contrast to CM, internal multiples, mode conversions, and transmission

loss are included. The method gained therefore attraction for the application in AVO inversion in recent years (Liu et al., 2016; Yang and Lu, 2020; Chen et al., 2020).

To compute spherical-wave synthetics using the SRM, a weighted sum of plane-wave contributions needs to be computed (Fuchs and Müller, 1971; Aki and Richards, 2002). The scalar potential $\Phi_r(x,t)$ of the spherical-wave reflection response from a layered medium observed at the surface $z = 0$ and at a source-receiver offset x is (Fuchs and Müller, 1971)

$$\Phi_r(x,t) = \frac{1}{2\pi}\int_{-\infty}^{\infty} e^{i\omega t} F(\omega) \int_0^{\infty} \frac{\omega p}{i q_1} J_0(\omega p x) r(\omega, p)\, dp\, d\omega \;, \tag{3}$$

where $q_1 = \sqrt{V_{P,1}^{-2} - p^2}$ is the vertical slowness in the uppermost layer with P-wave velocity $V_{P,1}$, J_0 is the Bessel function of the first kind and order zero, and $F(\omega)$ denotes the Fourier transform of the source excitation function $F(t)$. The slowness integral has an oscillatory integrand, which makes a dense sampling in slowness domain necessary to avoid spatial aliasing (Sen, 2021). This requirement increases the computational effort of computing $r(\omega, p)$ compared to the PRM. The generation of angle gathers from offset-time seismograms can be done by applying a migration algorithm (Hanitzsch et al., 1994) followed by an offset-angle mapping, which requires ray tracing. As an alternative to migration, normal moveout, and geometrical spreading correction can be applied. These additional steps to produce angle gathers from synthetic shot gathers from the SRM increase the computational cost further.

The generated pseudo-wells are in log scale and have a vertical sampling interval Δz of 0.125 m. This corresponds to a ratio of wavelength to vertical sampling interval of $\frac{\lambda}{\Delta z} = 693$ with the wavelength λ computed at the average shale velocity of 2600 m/s and a dominant wavelet frequency of 30 Hz. To reduce the computation time of seismic forward modeling, the models are upscaled (resampled) to a vertical sampling interval of 4 m, corresponding to $\frac{\lambda}{\Delta z} \approx 22$. The upscaling is performed by an aliasing-protected low-pass wavenumber filtering of the inverse P-wave modulus $c_{33}^{-1} = \rho^{-1} V_P^{-2}$, the inverse shear modulus $c_{44}^{-1} = \rho^{-1} V_S^{-2}$ and the density ρ (Tschache et al., 2022). The upscaling procedure preserves the low wavenumbers of the model properties up to the cut-off (Nyquist) wavenumber at $\frac{1}{2\Delta z}$ and removes the higher wavenumbers, which are irrelevant for a wave propagating with a wavelength of $\lambda \approx 84$ m.

Figure 6a shows the upscaled acoustic-impedance model (red) compared to the log-scale model (blue) of an example pseudo-well. The SRM (Figure 6b), PRM (Figure 6c), and CM (Figure 6d) synthetic angle gathers of the upscaled model generated using a 30 Hz Ricker wavelet are displayed. The computation times on a regular business laptop are given for orientation at the bottom of Figure 6. All three synthetic angle gathers are visually similar. The peak amplitudes at the top reservoir reflection at a 500 m depth were picked and the resulting amplitude variation with angle (AVA) is displayed in Figure 7. For comparison, the AVA of the SRM synthetics produced for the originally sampled model at log scale is shown by a dashed line. The AVA of the SRM and the PRM are generally in good agreement, while the AVA of the CM synthetics deviates considerably at large incidence angles. This is probably caused by offset-dependent tuning effects, which are not correctly simulated by the simplistic primaries-only CM approach. The PRM synthetics are equivalent to spherical-wave seismograms in the pre-critical angle range provided that the wave propagation distance is sufficiently long (Ursenbach et al., 2007). Because the velocity contrasts of the upscaled pseudo-wells are moderate, it can be guaranteed that critical angles are not reached in the angle range

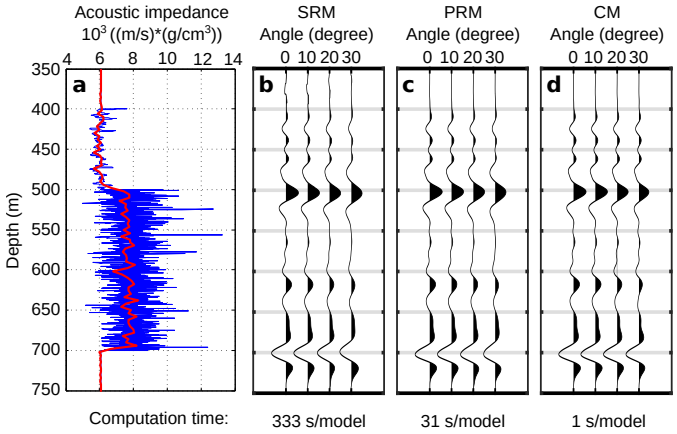

Figure 6: a: Acoustic impedance model in original sampling (blue) and upscaled version (red), b-d: corresponding synthetic seismic angle gathers from the spherical-wave reflectivity method (SRM), the plane-wave reflectivity method (PRM) and convolutional modeling (CM), respectively. A comparison of computation time is given at the bottom.

of 0° to 30°. The PRM requires a considerably shorter computation time than the SRM (see Figure 6, bottom) while providing sufficient amplitude accuracy and is therefore the preferred modeling method for this study.

AVO attribute extraction

The angle-dependent amplitudes $R(\theta)$ at the reservoir top are picked on the peak amplitude in a window 500 ± 10 m. A linear curve is fitted by the least-squares method to obtain the AVO intercept $R(0)$ and gradient G from Shuey's two-term approximation (Shuey, 1985)

$$R(\theta) = R(0) + G\sin^2\theta. \tag{4}$$

Bayesian inversion

The goal of solving the inverse problem is the estimation of reservoir properties $\mathbf{m}$ from geophysical data $\mathbf{d}$. In this study, the reservoir properties of interest are N/G and NP/N and the geophysical data are AVO attributes intercept $R(0)$ and gradient G. Because of the variable scale of heterogeneity of turbidite reservoir models, the relationship between reservoir properties and AVO attributes is non-unique (Takahashi, 2000). To honor this non-uniqueness, we can express the inverse problem as a conditional probability distribution $p(\mathbf{m} \mid \mathbf{d})$. According to Bayes' theorem, the posterior probability distribution can be estimated by

$$p(\mathbf{m} \mid \mathbf{d}) = \frac{p(\mathbf{d} \mid \mathbf{m})\, p(\mathbf{m})}{p(\mathbf{d})} = \text{const.} \cdot p(\mathbf{d} \mid \mathbf{m})\, p(\mathbf{m}), \tag{5}$$

where the likelihood function $p(\mathbf{d} \mid \mathbf{m})$ is the conditional probability distribution of AVO attributes conditioned on the reservoir properties N/G and NP/N, $p(\mathbf{m})$ is the prior

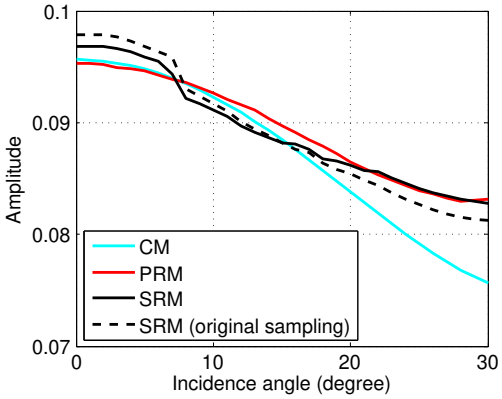

Figure 7: Amplitude variation with incidence angle of the top reservoir reflection measured on different synthetic seismic angle gathers.

probability of the reservoir properties independent of seismic AVO observations, and $p(\mathbf{d})$ is a normalizing constant.

By considering many equiprobable reservoir models $\mathbf{n}$ of a fixed set of N/G and NP/N, we can estimate the conditional probability density function (Takahashi, 2000)

$$p(\mathbf{d} \mid \mathbf{m}) = \int p(\mathbf{d} \mid \mathbf{n}, \mathbf{m})\, p(\mathbf{n} \mid \mathbf{m})\, d\mathbf{n}. \tag{6}$$

This is realized by simulating equiprobable pseudo-wells and applying seismic forward modeling to obtain AVO attributes as discussed in the previous subsections.

Using the described Monte Carlo approach of pseudo-well generation, seismic forward modeling, and AVO attribute extraction of many pseudo-well realizations, the two-dimensional model space of N/G and NP/N is explored systematically on a regular grid. Both N/G and NP/N range from 0 to 1. The grid spacing is chosen to be 0.1 for both parameters because the computational effort of the Monte Carlo simulation is heavy. At each model-space grid point $m_{i,j}$, 100 pseudo-wells are generated.

Results

Likelihood function

The seismic modeling as part of the Monte Carlo simulation was run for two different wavelets, a Ricker wavelet of 30 Hz peak frequency and a tapered Ormsby wavelet with corner frequencies 6 Hz, 10 Hz, 80 Hz, and 90 Hz, which are both shown in Figure 8. In this way, the impact of the wavelet's shape and bandwidth on the resulting probability density functions (PDFs) can be analyzed.

Bivariate normal distributions were fitted to the 100 data points to estimate the likelihood $p(R(0), G \mid m_{i,j})$ at each grid location $m_{i,j}$ in the model space. Figure 9 shows the mean, variance, and covariance values of the resulting PDFs in the model space for the two different wavelets. The AVO intercept is mainly sensitive to the fluid content. It is largest when there is brine ($NP/N = 0$) and smallest when there is a thin

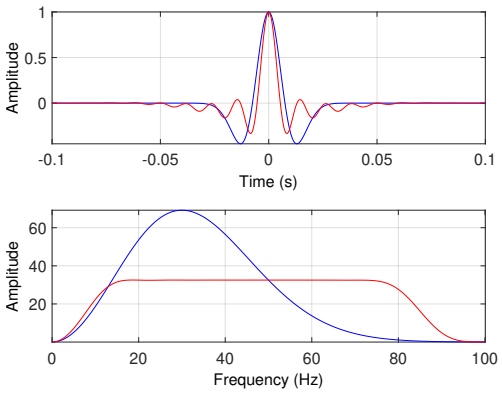

Figure 8: Ricker (blue) and tapered Ormsby (red) wavelet (top) and their corresponding frequency spectra (bottom).

oil interval ($NP/N = 0.1$). As expected, the fluid effect on $R(0)$ is stronger as N/G increases and vanishes if N/G is low. The AVO gradient shows a correlation with N/G: a decreasing N/G makes the gradient more negative. There is also sensitivity for varying NP/N when NP/N is low. The gradient sensitivity for low NP/N is mainly driven by the interference with the OWC reflection response. If NP/N is larger than 0.4, the OWC response is too far away from the top reservoir reflection to interfere with it. We can conclude from this observation that the sensitivity interval of the two wavelets reaches a maximum depth of 80 m measured from the reservoir top.

The different interference pattern of the two wavelets explains the difference in the mean gradient displays. For the Ricker wavelet, there is a gradient depression at $NP/N = 0.2$, which is found at $NP/N = 0.1$ for the Ormsby wavelet. The variances are significantly higher for the Ormsby wavelet than for the Ricker wavelet, probably caused by the longer coda of the Ormsby wavelet. This indicates that the broadband Ormsby wavelet is less suitable for an inversion of AVO attributes, which are measured at the reservoir top, for N/G and NP/N.

Prior probability

The estimation of realistic prior probabilities is often challenged by sparse a priori information. We gathered data of N/G and NP/N from six wells of the study area, which is not enough to estimate a probability distribution. Therefore, we built a simple prior model shown in Figure 10 that integrates the observations without making too strict assumptions on the probability distribution. For N/G, an equal prior probability is assumed in the range of 0.3 to 0.9 and a lower prior probability at the limits. The prior probability of NP/N is equal for the range of 0 to 0.4 and decreases by a Gaussian taper towards a low prior probability for $NP/N = 1$, which represents a completely oil-saturated reservoir unit of 200 m.

Brunstad et al. (2013) investigated the N/G of several formations of the Rogaland group. For the reservoir formation of concern, they estimated a general N/G of about 0.65, which is in good agreement with the observed range of N/G at the well locations shown in Figure 10.

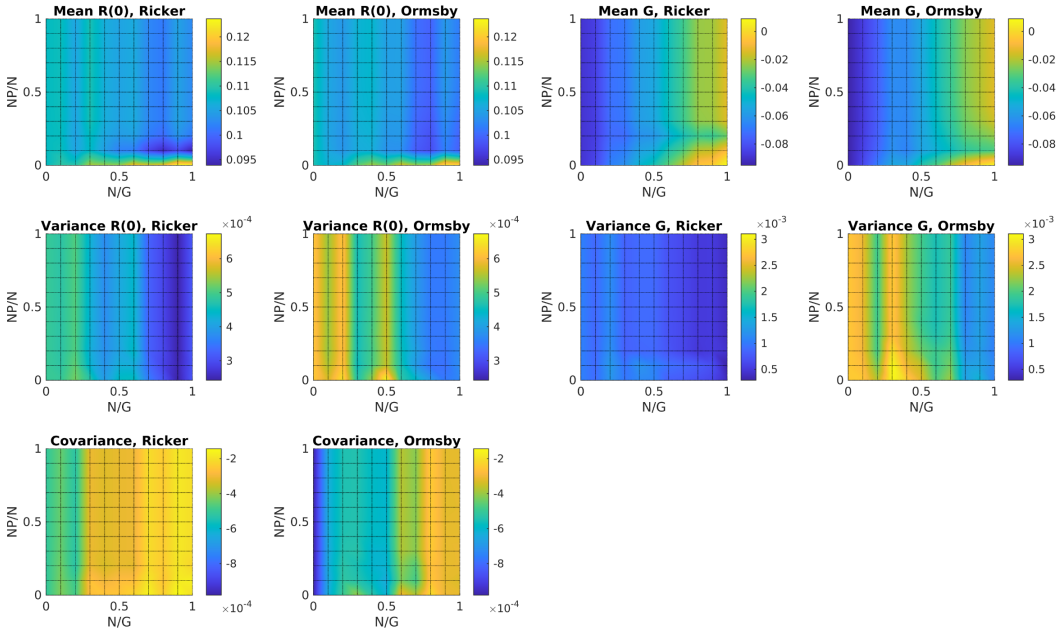

Figure 9: Mean, variance, and covariance of intercept $R(0)$ and gradient G resulting from Monte Carlo simulation using a Ricker and Ormsby wavelet displayed on a grid of varying net-to-gross ratio N/G and net-pay-to-net ratio NP/N. Interpolation between grid points was done for display purposes.

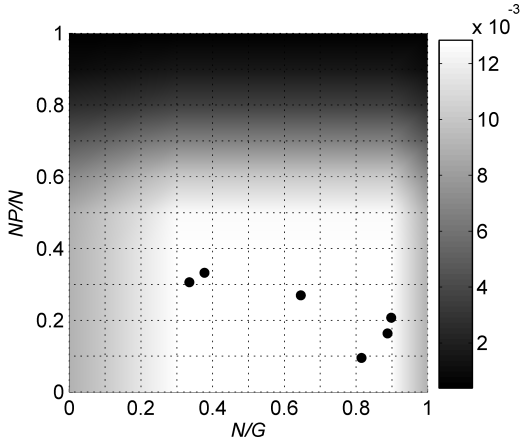

Figure 10: Prior probability of N/G and NP/N with a priori information from six wells shown by black markers.

Posterior probability

Using Bayes' theorem and linear interpolation, the posterior probabilities can be computed for a given data point $(R(0), G)$. This has been done on a regular grid of $R(0)$ and G covering the central zone of observed AVO attributes resulting from the Monte Carlo simulation. In Figure 11, the posterior probabilities are displayed in the form of contour lines of highest posterior density (HPD) regions. These HPD contours can be easily interpreted. The probability that N/G and NP/N are inside the 90 % HPD contour is 90 %. Additionally, the locations of maximum a posteriori probability (MAP) are displayed.

Figure 11 visualizes how well the reservoir properties N/G and NP/N are constrained at different locations in the AVO crossplot. At $R(0) = 0.14, G = 0.02$, for example, a fully brine-saturated high-N/G reservoir condition is predicted with confidence. For other values, such as $R(0) = 0.10, G = -0.04$, the HPD regions are large indicating that N/G and NP/N are not well constrained by the AVO attributes. The posterior probabilities nicely reflect the already mentioned correlation between gradient and N/G and the weak dependence of N/G on the intercept.

Application to pseudo-wells

To check the consistency of the inversion, we applied it to 1000 test pseudo-wells with reservoir properties N/G and NP/N that were drawn from the prior probability distribution shown in Figure 10. The test pseudo-wells were generated using the same workflow as discussed in the Methods section, followed by the generation of synthetic seismic angle gathers by the PRM, amplitude picking, and estimation of AVO intercept and gradient.

Figure 12a shows the AVO attributes of all test pseudo-wells in an AVO crossplot. We demonstrate the reliability of the inversion at one example location in the AVO crossplot at $R(0) = 0.1$ and $G = -0.04$. For this specific pair of AVO attributes, the posterior probability density was computed by the inversion and is shown as 90 % and 50 % HPD region contours in Figure 12b. The test pseudo-wells that are closest to the target point in the AVO crossplot were selected and are shown by red markers in Figure 12a. Assuming that we can apply the target posterior to those selected test pseudo-wells that have a very similar AVO to the target, we plot their true N/G and NP/N values in the target HPD region display (Figure 12b). We see that 16 out of 18 (89 %) selected test pseudo-wells are located inside the 90 % HPD region and 8 (44 %) are located inside the 50 % HPD region. Given the relatively small number of selected test pseudo-wells, these scores match well with the expectation. Figure 12b also demonstrates the non-uniqueness of the estimation of reservoir properties from AVO attributes when using a very smooth and almost uniform prior model. A wide range of reservoir properties can lead to the same observed AVO at the reservoir top.

From all 1000 test pseudo-wells with known N/G and NP/N, we counted how many are in the respective HPD regions between 10 % and 90 %. The observed scores shown in Figure 13 are close to the expectation. Slightly higher scores could be a consequence of the linear interpolation that was applied to compute the HPD regions.

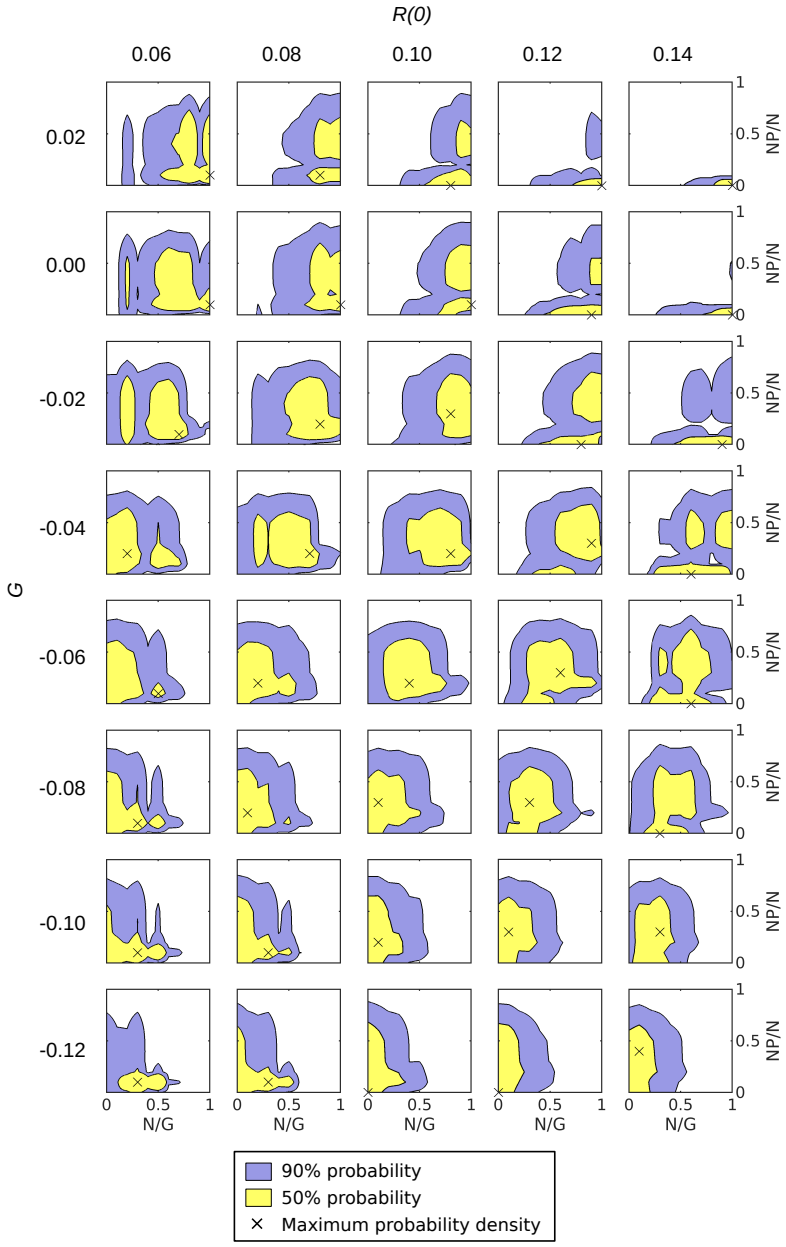

Figure 11: Highest posterior density regions of 90 % (outer contour, purple region) and 50 % (inner contour, yellow region) probability of N/G and NP/N estimated on a grid of varying $R(0)$ and G. Crosses show the locations of the maximum a posteriori probability.

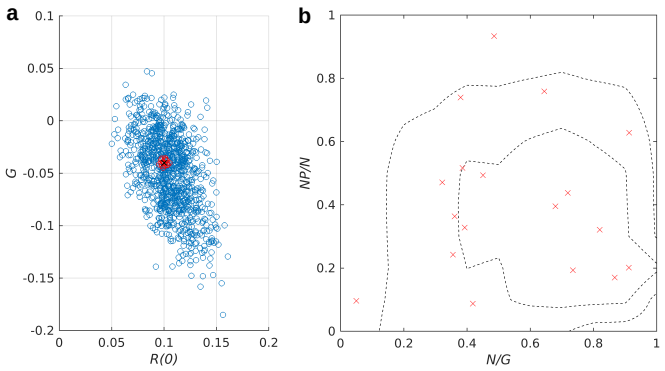

Figure 12: a: AVO crossplot of all 1000 test pseudo-wells (blue markers) with the target AVO marked by a black cross and the selection of neighboring test pseudo-wells marked in red. b: Contours of the 90 % (outer) and 50 % (inner) highest posterior density regions for the target AVO with the true reservoir properties of the selected neighbor test pseudo-wells shown by red crosses.

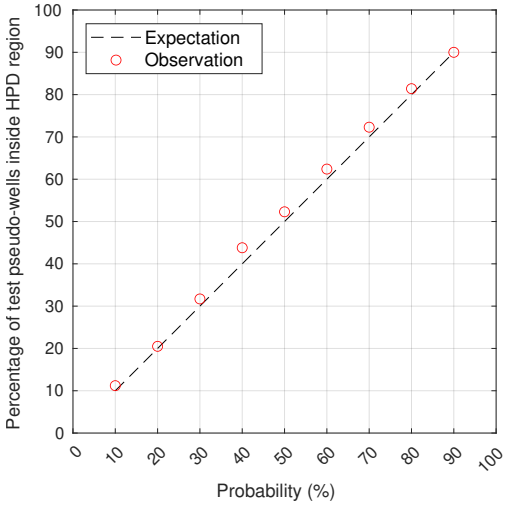

Figure 13: Percentage of test pseudo-wells with N/G and NP/N inside the respective highest posterior density (HPD) regions of a given probability compared to the expectation.

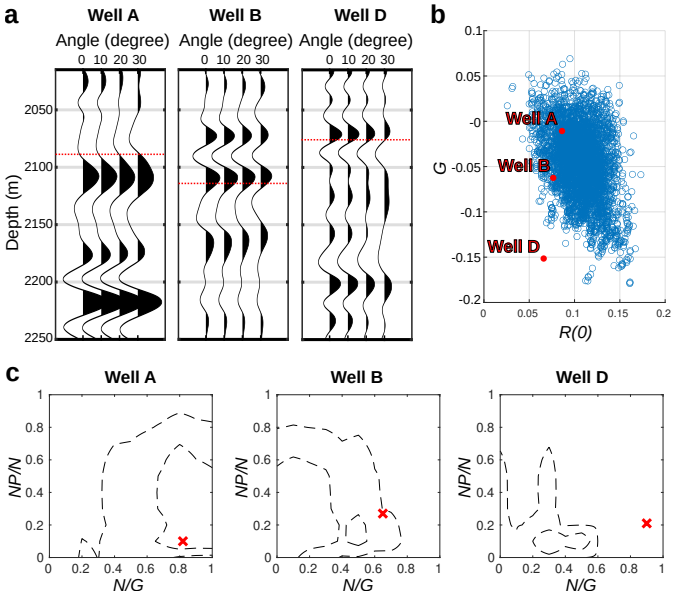

Figure 14: a: Synthetic seismic angle gathers of three wells computed by the PRM. The top of the reservoir interpreted from the well data is indicated by dotted red lines. b: Measured seismic AVO of the three wells (red markers) plotted on top of the AVO of all pseudo-wells (blue markers) c: Inversion results for the three wells showing the contours (dashed lines) of the 90 % (outer) and 50 % (inner) HPD regions and the actual N/G and NP/N by red crosses.

Application to synthetic seismic data from well logs

The inversion was applied to the AVO data from synthetic seismic angle gathers computed by the PRM using the well-log data from three wells (A, B, D). Well A does not have shear-wave logs and V_S was estimated using the RPM. Figure 14a shows the angle gathers in depth with the top of the reservoir interpreted from well data marked. The peak amplitudes closest to the reservoir top were picked, and $R(0)$ and G were estimated. The AVO crossplot shown in Figure 14b reveals that the AVO of wells A and B is inside the distribution of AVO estimated from pseudo-wells, while the AVO observed at well D is outside. Consequently, the inversion result for well D is unreliable (Figure 14c right). As can be seen on the angle gather from well D, the top reservoir reflection is masked by a thin, hard layer that produces a typical dipole (peak-trough) seismic reflection response. The inversion results at wells A and B shown in Figure 14c (left and center) match well with the actual reservoir properties at these well locations. In case of well A, the true N/G and NP/N point is inside the 50 % HPD region. For well B, the true N/G and NP/N location is outside the 50 % HPD region but inside the 90 % HPD region.

Application to field data

The inversion was finally applied to field seismic AVO data from the Jotun Field, a North Sea oil field in Paleocene sandstones of turbidite deposits (Bergslien, 2002). In

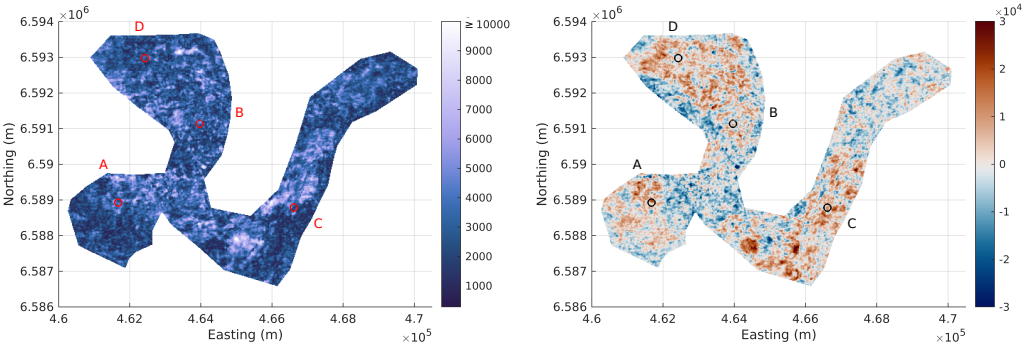

Figure 15: Maps of the AVO intercept (left) and gradient (right) of the top reservoir reflection response. The locations of four wells A-D are indicated.

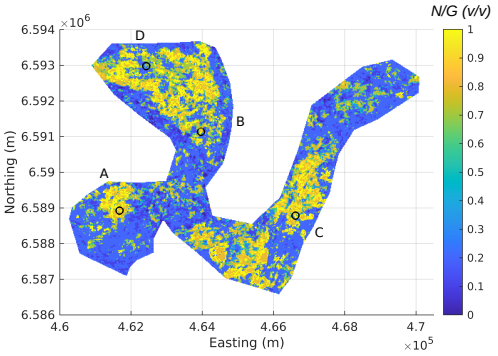

Figure 16: Map of the net-to-gross ratio N/G where the posterior probability is highest.

the study area, the transition from the caprock shale (Sele and Lista Formations) to the reservoir sand (Heimdal Formation) is seismically characterized by a hard event (increase in acoustic impedance resulting in a positive peak) and a class I AVO signature. The reservoir top has been interpreted following the peak amplitude on a near (0° to 15°) and far (24° to 39°) sub-stack. However, the interpretation was challenging, and its confidence decreases away from well control. Figure 15 shows the resulting AVO attribute maps of intercept and gradient at the reservoir top, generated using windowed root-mean-squared amplitudes around Top Heimdal from near and far sub-stacks.

New synthetic angle gathers of the pseudo-wells were generated to encompass the angle range 0° to 39° and to use an extracted wavelet from the seismic data. The observed seismic AVO intercept and gradient values were calibrated using synthetic seismic AVO data at the three wells A, B, and D (Figure 15). In a second calibration step, the gradient was scaled to match the variance of the pseudo-well gradients. The inversion was applied to the calibrated seismic AVO data. At every location on the map, the inversion result is a bivariate PDF of N/G and NP/N. The maps in Figures 16 and 17 show the MAP solution.

Figure 18 shows an uncertainty estimate, which is the proportional area of the 90 % HPD region in the N/G-NP/N space. An estimate of net pay was generated by com-

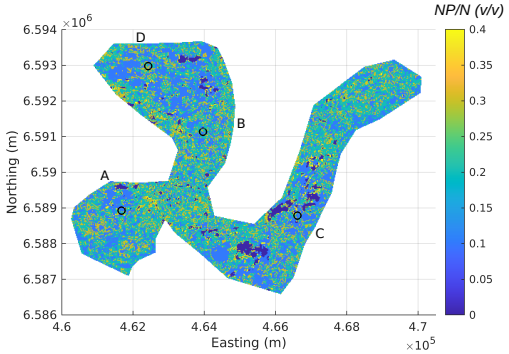

Figure 17: Map of the net-pay-to-net ratio NP/N where the posterior probability is highest.

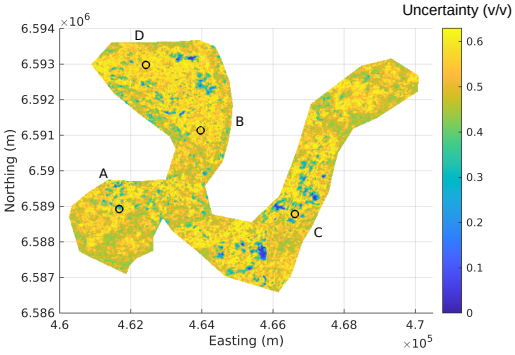

Figure 18: Map of the uncertainty of N/G and NP/N.

puting the product of the MAP N/G, the MAP NP/N, and a constant gross thickness of 200 m. The resulting net-pay map is shown in Figure 19.

The MAP N/G (Figure 16) shows a correlation with the AVO gradient. Patches of high N/G are predicted where the gradient is positive and largest. There are coherent clusters of high MAP N/G that can be interpreted, for example around well A.

The MAP NP/N (Figure 17) varies only between 0 and 0.4 because there is no sensitivity of the AVO attributes for higher NP/N. A MAP $NP/N = 0$ indicates the absence of hydrocarbon and these zones correspond to a large AVO intercept. The presence of hydrocarbon has a dimming effect on the amplitude in this hard sand reservoir. For most parts of the map, a NP/N between 0.1 and 0.3 is predicted as the most likely value, which means that the presence of oil is more likely in these places than the presence of brine.

The uncertainty estimate of the inversion (Figure 18) is high (≥ 0.5) throughout vast parts of the map. Low uncertainty values correlate with high AVO intercept, where the absence of hydrocarbon ($NP/N = 0$) is predicted. The high level of uncertainty should always be kept in mind when interpreting the MAP N/G and MAP NP/N maps.

The map of net pay (Figure 19) is a scaled product of the MAP N/G and MAP NP/N maps and indicates the expected net pay in meters. If a gross thickness map is

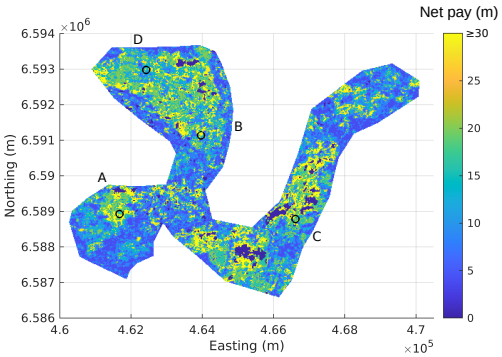

Figure 19: Map of the net-pay thickness in meters estimated from the MAP N/G and the MAP NP/N. The color scale was capped at 30 m.

available, it should be used in the calculation of net pay rather than assuming a constant gross thickness.

Figure 20 shows the bivariate PDFs resulting from the inversion as filled contours of the 50 % and 90 % HPD regions and the MAP solution for wells A-D together with the true values of N/G and NP/N. At well A, the MAP prediction almost coincides with the actual values of N/G and NP/N. This is also the location of the highest confidence of the input AVO maps. For two wells (A and B), the true values are located inside the 50 % HPD regions and in all four cases they are located inside the 90 % probability contours. A huge deviation of the MAP solution at well C from the true values can be explained by a gas cap that was drilled there. The presence of gas (as opposed to oil or brine) was neglected by the simplified assumptions of the modeling. All inversion results in the gas cap of the Tau structure (Bergslien, 2002) should therefore be disregarded.

Suggestions for further study

The net-to-gross ratio is a scale-dependent parameter (Avseth et al., 2009) and is also dependent on the definition of net intervals. In this study, we refer to N/G interpreted at log scale with measurement intervals of 0.125 to 0.15 m. The facies, rock physical, and elastic properties of pseudo-wells are simulated consistently in log scale. N/G varies vertically and laterally in turbidite reservoirs. Typical turbidite sequences, such as Bouma (Bouma, 1962) or Lowe (Lowe, 1982) sequences, have not been considered in this study and could be accounted for in future work.

The generated pseudo-wells rely on several simplifying assumptions. One basic assumption is that the reservoir can be described by a sequence of sand and shale layers. Additional facies, such as shaly sand, could be added if deemed necessary. Despite only two facies being used, the variability of rock physical and elastic properties observed from well logs have been incorporated. We further assume that the reservoir thickness is above the tuning thickness (Widess, 1973) and that the top and base reflections are completely separated. We also simplified the fluid saturation scenarios for practical purposes. The presence of gas and a variable saturation of mixed fluids could be considered in future work. The effect of the caprock has been ignored in many earlier studies (Takahashi et al., 1999; Stovas et al., 2006; Pradhan and Mukerji, 2020). We realized that caprock

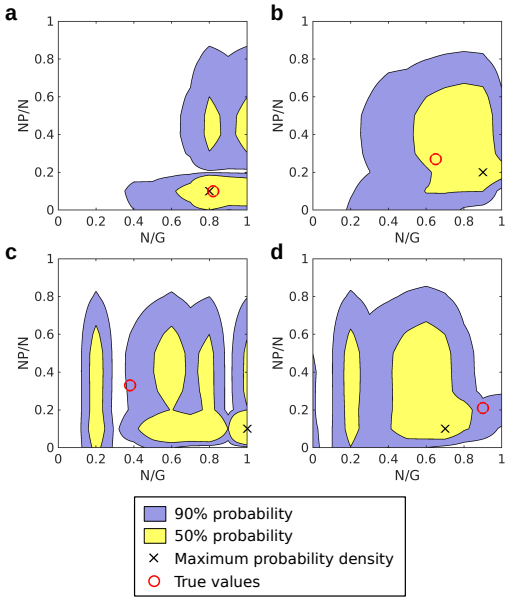

Figure 20: Inversion results at wells A-D (a-d) displayed by the highest posterior density regions of 90 % and 50 % probability and the maximum a posteriori solution compared to the true N/G and NP/N values.

heterogeneity affects the measured AVO at the reservoir top through interference and have included this effect in the presented workflow for the generation of pseudo-wells.

The usage of AVO attributes measured at the top of the reservoir sets a limitation on the presented method. The reflection response at the reservoir top is most sensitive to the uppermost part of the reservoir and it is assumed that the predicted N/G there is representative of the whole reservoir unit. The sensitivity limit for the wavelets included in this study is located at 80 m depth below the reservoir top. Nevertheless, we show that useful information on reservoir properties can be derived. The AVO attributes at the reservoir top are influenced by the type of pore fluid and by the OWC when it is within the sensitivity interval of the wavelet. The presented inversion can be applied to AVO attribute maps that are often already available or that can be easily produced from sub-stacks. An interesting present and future research direction is the usage of complete seismic traces and the application of machine learning methods as proposed by Pradhan and Mukerji (2020).

Local geological features such as facies that are considerably softer or harder than shale or sand can perturb the seismic reflection response at the top of the reservoir as has been observed in well D. The presented inversion is not adapted to such irregularities. If there are indications for thin, hard layers intercalated in the reservoir or caprock, such as calcite-cemented sand layers, these should be included in the pseudo-wells (Tschache et al., 2023).

The estimated uncertainty values represent only the geological uncertainty originating from the non-unique relationship between AVO measured at the reservoir top and the reservoir properties of interest. Additional uncertainty associated with the measurement

error of seismic amplitudes and AVO is not included, such as noise in the seismic data, amplitude distortions from processing, or errors related to the interpretation of the top reservoir reflection, the calibration of the seismic amplitudes, and the estimation of the AVO attributes. The signal-to-noise ratio of the AVO intercept is higher than that of the AVO gradient (Chopra and Castagna, 2014). Especially the prediction of N/G will suffer from low-quality gradient input data. The incorporation of the measurement uncertainty of the AVO attributes should be addressed in future work.

Possible ways to reduce the uncertainty of the predictions would be a more constraining prior model or the incorporation of more input variables. As discussed, the usage of complete seismic traces is also promising (Kjønsberg et al., 2010; Pradhan and Mukerji, 2020).

The presented inversion contains several improvements compared to previous work by Takahashi et al. (1999) and Stovas et al. (2006). The correlation between the reservoir properties and the AVO attributes is investigated which helps to understand the inversion results. The prior model can be easily replaced to include additional data. The pseudo-wells are constructed based on the observed regional characteristics of sand and shale layers. The usage of an adequate seismic forward modeling method allows us to include all scattering effects instead of regarding the reservoir as an effective medium. Combining the pseudo-wells and the seismic forward modeling, the geological uncertainty of the estimation of reservoir properties based on AVO is estimated, which is important to consider in quantitative seismic interpretation.

Conclusion

We present a 1D Bayesian inversion that estimates the probability density function of the local reservoir properties net-to-gross ratio N/G and net-pay-to-net ratio NP/N given the AVO attributes intercept $R(0)$ and gradient G at the reservoir top as input data. From the estimated probability density functions, regions of highest posterior density can be computed, or the maximum a posteriori solution together with uncertainty measures can be derived.

A reflectivity method producing plane-wave synthetics was used for seismic forward modeling because it yields better amplitude accuracy than primaries-only convolutional modeling for an acceptable computational cost. We found a broadband wavelet to be less suitable for the presented workflow than a Ricker wavelet because observed variances of AVO attributes are significantly larger when using a broadband wavelet with a long coda. In the study area, the AVO intercept is mainly sensitive to the pore fluid, while the AVO gradient shows a correlation with N/G and sensitivity for low NP/N.

The consistency of the method was proven on a test dataset of pseudo-wells. The inversion was further tested on synthetic seismic AVO at well locations, where it gave reasonable results when the observed AVO was in the range of AVO of the training dataset. We applied the inversion to AVO attribute maps of the reservoir top of the Jotun Field, where maps of the most likely N/G, NP/N, net pay, and of the uncertainty were produced. Despite the high uncertainty in predicting definite values of reservoir properties, spatial trends could be identified. Such maps can, combined with other information, support the screening for areas of high reservoir quality.

Acknowledgments

We would like to thank Liv Inger Trøan for the preparation of the well data and Rosario Negusse for loading the seismic data. For geostatistical simulation, we used the open-source Stanford Geostatistical Modeling Software (SGeMS) and the Matlab toolbox mGstat, which was written by Thomas Mejer Hansen. The Matlab package SeisLab written by Eike Rietsch was used for the display of seismic angle gathers. We express our gratitude to the Research Council of Norway, the University of Bergen, and CGG for funding this work through an industrial Ph.D. grant, project no. 310441.

References

Aki, K., and P. G. Richards, 2002, Quantitative seismology, 2nd ed.: University Science Books.

Allo, F., 2019, Consolidating rock-physics classics: A practical take on granular effective medium models: The Leading Edge, **38**, 334–340.

Allo, F., J.-P. Coulon, J.-L. Formento, R. Reboul, L. Capar, M. Darnet, B. Issautier, S. Marc, and A. Stopin, 2021, Characterization of a carbonate geothermal reservoir using rock-physics-guided deep neural networks: The Leading Edge, **40**, 751–758.

Avseth, P. A., 2000, Combining rock physics and sedimentology for seismic reservoir characterization of North Sea turbidite systems: Ph.d. thesis, Stanford University.

Avseth, P., J. Dvorkin, G. Mavko, and J. Rykkje, 2000, Rock physics diagnostic of North Sea sands: Link between microstructure and seismic properties: Geophysical Research Letters, **27**, 2761–2764.

Avseth, P., A. Jørstad, A.-J. van Wijngaarden, and G. Mavko, 2009, Rock physics estimation of cement volume, sorting, and net-to-gross in North Sea sandstones: The Leading Edge, **28**, 98–108.

van der Baan, M., 2004, Processing of anisotropic data in the τ-p domain; I, Geometric spreading and moveout corrections: GEOPHYSICS, **69**, 719–730.

Bergslien, D., 2002, Balder and Jotun; two sides of the same coin? A comparison of two Tertiary oil fields in the Norwegian North Sea: Petroleum Geoscience, **8**, 349–363.

Bouma, A. H., 1962, Sedimentology of Some Flysch Deposits: A Graphic Approach to Facies Interpretation: Elsevier Publishing Company.

Brunstad, H., F. Gradstein, J. E. Lie, Ø. Hammer, D. Munsterman, G. Ogg, and M. Hollerbach, 2013, Stratigraphic Guide to the Rogaland Group, Norwegian North Sea: Newsletters on Stratigraphy, **46**, 137–286.

Chen, L., J. Li, X. Chen, H. Liu, and L. Zhou, 2020, Prestack AVO inversion based on the vectorised reflectivity method with blockiness constraint: Exploration Geophysics, **51**, 535–548.

Chopra, S., and J. P. Castagna, 2014, AVO: Society of Exploration Geophysicists.

Connolly, P., 2007, A simple, robust algorithm for seismic net pay estimation: The Leading Edge, **26**, 1278–1282.

Connolly, P. A., and M. J. Hughes, 2016, Stochastic inversion by matching to large numbers of pseudo-wells: GEOPHYSICS, **81**, no. 2, M7–M22.

Das, V., A. Pollack, U. Wollner, and T. Mukerji, 2019, Convolutional neural network for seismic impedance inversion: GEOPHYSICS, **84**, no. 6, R869–R880.

Deutsch, C. V., and A. G. Journel, 1992, GSLIB: Geostatistical Software Library and User's Guide: Oxford University Press.

Doyen, P., 2007, Seismic Reservoir Characterization: European Association of Geoscientists & Engineers.

Fuchs, K., and G. Müller, 1971, Computation of Synthetic Seismograms with the Reflectivity Method and Comparison with Observations: Geophysical Journal International, **23**, 417–433.

Gancarski, S., J. P. Valois, and C. Palus, 1994, The pseudo-well technique – A Tool for statistical calibration of seismic data in a field with limited well control: 56th EAEG Meeting and Technical Exhibition, Extended Abstracts, P055.

Gassmann, F., 1951, Über die Elastizität poröser Medien: Vierteljahrsschrift der Naturforschenden Gesellschaft in Zürich, **96**, 1–23.

Goovaerts, P., 1997, Geostatistics for natural resources evaluation: Oxford University Press.

Grana, D., L. Azevedo, L. de Figueiredo, P. Connolly, and T. Mukerji, 2022, Probabilistic inversion of seismic data for reservoir petrophysical characterization: Review and examples: GEOPHYSICS, **87**, no. 5, M199–M216.

Hanitzsch, C., J. Schleicher, and P. Hubral, 1994, True-amplitude migration of 2D synthetic data: Geophysical Prospecting, **42**, 445–462.

Joseph, C., F. Fournier, and S. Vernassa, 1999, Pseudo-well methodology: A guiding tool for lithoseismic interpretation: Annual Meeting 1999, SEG, Expanded Abstracts, 938–941.

Kennett, B. L. N., 1974, Reflections, rays, and reverberations: Bulletin of the Seismological Society of America, **64**, 1685–1696.

Kennett, B. L. N., 2009, Seismic wave propagation in stratified media, new edition: ANU E Press.

Kjønsberg, H., R. Hauge, O. Kolbjørnsen, and A. Buland, 2010, Bayesian Monte Carlo method for seismic predrill prospect assessment: GEOPHYSICS, **75**, no. 2, O9–O19.

Lai, H., and R. L. Gibson Jr., 2005, Stochastic models of turbidite reservoirs for seismic simulations: Annual Meeting 2005, SEG, Expanded Abstracts, 1453–1456.

Liu, H., J. Li, X. Chen, B. Hou, and L. Chen, 2016, Amplitude variation with offset inversion using the reflectivity method: GEOPHYSICS, **81**, no. 4, R185–R195.

Lowe, D. R., 1982, Sediment gravity flows; II, Depositional models with special reference to the deposits of high-density turbidity currents: Journal of Sedimentary Research, **52**, 279–297.

Marion, D., T. Mukerji, and G. Mavko, 1994, Scale effects on velocity dispersion: From

ray to effective medium theories in stratified media: GEOPHYSICS, **59**, 1613–1619.

Oliveira, S. A. M., I. L. S. Braga, M. B. Lacerda, G. F. Ouverney, and A. W. P. de Franco, 2018, Extending the useful angle range for elastic inversion through the amplitude-versus-angle full-waveform inversion method: GEOPHYSICS, **83**, no. 3, R213–R226.

Pradhan, A., and T. Mukerji, 2020, Seismic Bayesian evidential learning: estimation and uncertainty quantification of sub-resolution reservoir properties: Computational Geosciences, **24**, 1121–1140.

Remy, N., A. Boucher, and J. Wu, 2009, Applied geostatistics with SGeMS: a user's guide: Cambridge University Press.

Rietsch, E., 2008, A designer attribute for net-sand thickness estimation: The Leading Edge, **27**, 386–393.

Russell, B. H., 1988, 2. Part 2 - The Convolutional Model, *in* S. N. Domenico, ed., Introduction to seismic inversion methods, Society of Exploration Geophysicists, 2-1–2-19.

Sen, M. K., 2021, Seismic, Reflectivity Method, *in* H. K. Gupta, ed., Encyclopedia of Solid Earth Geophysics, 2nd edition, Springer International Publishing, 1592–1602.

Shuey, R. T., 1985, A simplification of the Zoeppritz equations: GEOPHYSICS, **50**, 609–614.

Sinvhal, A., and K. Khattri, 1983, Application of seismic reflection data to discriminate subsurface lithostratigraphy: GEOPHYSICS, **48**, 1498–1513.

Spikes, K. T., 2009, Statistical classification of seismic amplitude for saturation and net-to-gross estimates: The Leading Edge, **28**, 1436–1443.

Stovas, A., and M. Landrø, 2006, Uncertainty in discrimination between net-to-gross and water saturation for fine-layered reservoirs: Annual Meeting 2006, SEG, Expanded Abstracts, 1698–1702.

Stovas, A., M. Landrø, and P. Avseth, 2006, AVO attribute inversion for finely layered reservoirs: GEOPHYSICS, **71**, no. 3, C25–C36.

Takahashi, I., 2000, Quantifying information and uncertainty of rock property estimation from seismic data: Ph.d. thesis, Stanford University.

Takahashi, I., T. Mukerji, and G. Mavko, 1999, Effect of thin-layering on seismic reflectivity: Estimation of sand/shale ratio using stochastic simulation and Bayes' inversion: Annual Meeting 1999, SEG, Expanded Abstracts, 1787–1790.

Tschache, S., V. Vinje, and E. Iversen, 2022, On the accuracy and spatial sampling of finite-difference modelling in discontinuous models: Journal of Applied Geophysics, **206**, 104789.

Tschache, S., V. Vinje, J. E. Lie, and E. Iversen, 2023, Quantifying amplitude-variation-with-offset uncertainties related to calcite-cemented beds using a Monte Carlo simulation: Interpretation, **11**, no. 2, T279 - T293.

Ursenbach, C. P., A. B. Haase, and J. E. Downton, 2007, Efficient spherical-wave AVO modeling: The Leading Edge, **26**, 1584–1589.

Vernik, L., 2016, Seismic petrophysics in quantitative interpretation: Society of Exploration Geophysicists.

Vernik, L., D. Fisher, and S. Bahret, 2002, Estimation of net-to-gross from P and S impedance in deepwater turbidites: The Leading Edge, **21**, 380–387.

Weimer, P., and M. H. Link, 1991, Global Petroleum Occurrences in Submarine Fans and Turbidite Systems, *in* P. Weimer and M. H. Link, eds., Seismic Facies and Sedimentary Processes of Submarine Fans and Turbidite Systems. Frontiers in Sedimentary Geology, Springer, 9–67.

Widess, M. B., 1973, How thin is a thin bed? GEOPHYSICS, **38**, 1176–1180.

Yang, Z., and J. Lu, 2020, Thin interbed AVA inversion based on a fast algorithm for reflectivity: Acta Geophysica, **68**, 1007–1020.

Graphic design: Communication Division, UiB / Print: Skipnes Kommunikasjon AS

uib.no

ISBN: 9788230847893 (print)
9788230864463 (PDF)